

GAS-SURFACE INTERACTION, RADIATIVE HEAT TRANSFER
AND THERMOCHEMISTRY MODELING IN THE SIMULATION OF
PARAFFIN-BASED HYBRID ROCKET ENGINES

GIUSEPPE LECCESE



Advisor: Prof. F. Nasuti

Sapienza University

DIMA – Mechanical and Aerospace Engineering Department
Ph.D. Course in Aeronautics and Space Engineering – XXX Cycle
Rome, IT

October 2017

Giuseppe Leccese : *Gas–Surface Interaction, Radiative Heat Transfer and Thermochemistry Modeling in the Simulation of Paraffin–Based Hybrid Rocket Engines*, © October 2017

To my family

e volta nostra poppa nel mattino,
de' remi facemmo ali al folle volo

Dante Alighieri, *Divina Commedia – Inferno – Canto XXVI*

ABSTRACT

The present thesis is focused on the computational fluid dynamics modeling of paraffin-based hybrid rocket engines. For the purpose, a comprehensive theoretical and numerical model with predictive capabilities of the motor internal ballistics is proposed. The main idea behind the model is to take advantage of typical supercritical pressure conditions of melted paraffin-wax, when injected into the port of hybrid rocket thrust chambers, to maintain a single-phase approach.

Before being implemented into an in-house Reynolds-averaged Navier-Stokes solver for compressible, turbulent, multicomponent and reacting flows, suitable physical sub-models are developed. First of all, a gas-surface interaction boundary condition, based on interface mass and energy balances, is specialized to the case of liquefying fuels, such as paraffin-waxes. After that, by using the discrete transfer method, a radiative heat transfer model is developed to allow the inclusion of the radiative contribution to the wall heat flux into the interface energy balance. A dedicated chemical global mechanism is finally introduced to evaluate finite-rate combustion between gaseous-oxygen and thermal cracking products of melted paraffin-wax.

Sufficiently accurate pressure, temperature and species concentration fields, as required by the thermal radiation computation, are ensured by including dissociations within the set of chemical reactions. The importance of coupling the radiative heat transfer model with such kind of chemistry description is highlighted in preliminary results, obtained by rebuilding a test campaign performed on a lab-scale motor using the gaseous-oxygen/hydroxyl-terminated poly-butadiene propellant combination.

Simulations with the fully coupled model for paraffin-based fuels are finally carried out by rebuilding selected firing tests of a medium-scale gaseous-oxygen/paraffin-wax hybrid rocket engine. The capabilities of the model to describe the main features of the flow field, as well as diffusion flame characteristics and melted paraffin-wax concentration, are highlighted. The relative magnitude of different

contributions to the total wall heat flux is also investigated. After the ability of the combustion and mixing model to predict the motor characteristic velocity is proved, a direct comparison of numerical results against experimental data is carried out for different mass flux and chamber pressure conditions.

Promising results are found, encouraging further developments to pave the way for improving the technology readiness of paraffin-based hybrid rocket engines by deeper numerical investigations of relevant physical phenomena and coupling.

ACKNOWLEDGMENTS

I would like to express all my gratitude to Prof. Francesco Nasuti for his very enriching guidance and teachings since the time I was a student in his courses. It has been a honor to work together along these years and to have him as advisor for this stimulating research work.

A very special and warm thank goes to Dr. Daniele Bianchi, his willingness to donate his experience and support really made possible this research work. I owe to him too my scientific growth along these three years.

A sincere thank is also for Prof. Diego Lentini who was instrumental to kick-off this work by introducing me to the discrete transfer method for radiative heat transfer calculations.

I would like to conclude expressing my gratitude to Prof. Brian Cantwell and his research group for hosting me during the visiting period at Stanford University. I have great memories of that period as a unique scientific opportunity and a wonderful life experience.

CONTENTS

Introduction	4
1 STATE OF THE ART	5
1.1 Brief overview of hybrid rocket historical background	5
1.2 Fundamental analyses of hybrid rocket regression rate	7
1.3 CFD modeling of hybrid rocket flow fields	8
1.4 Research activities on paraffin-based hybrid rocket engines	12
1.5 CFD activities on paraffin-based hybrid rocket engines	16
2 THEORETICAL AND NUMERICAL FLUID DYNAMICS MODEL	19
2.1 Conservation principles	19
2.2 Equation of state	20
2.3 Thermophysical properties	21
2.4 Chemical source terms	22
2.5 Turbulence closure equation	23
2.6 Numerical method	25
3 GAS-SURFACE INTERACTION MODEL	27
3.1 Entrainment phenomena	27
3.2 Gas-surface interaction boundary conditions	28
3.3 Surface mass and energy balances	29
3.4 Formulation for hybrid rocket fuel grains	32
3.4.1 Non-liquefying fuels	33
3.4.2 Liquefying fuels	33
4 RADIATIVE HEAT TRANSFER MODEL	37
4.1 Fundamentals of thermal radiation	37
4.2 Radiative properties of molecular gases	46
4.3 Radiative transfer in participating media	48
4.4 Discrete transfer method	51
4.5 Developed radiative code	53
4.6 Code testing and convergence analysis	54

4.6.1	Infinitely long square cavity	55
4.6.2	Sub-scale liquid rocket engine	58
5	THERMOCHEMISTRY MODEL	63
5.1	Basics of supercritical fluids behavior	63
5.2	Paraffin-wax thermophysical properties	65
5.3	Paraffin-wax thermal cracking	67
5.4	Global reaction mechanism without dissociations	69
5.5	Global reaction mechanisms including dissociations	71
5.5.1	HTPB fuel	71
5.5.2	Paraffin-wax fuel	72
6	VALIDATION: HTPB CASE STUDY	77
6.1	Overview	77
6.2	Experimental test cases	77
6.3	CFD grid and boundary conditions	79
6.4	Role of operating conditions on thermal radiation	81
6.5	Effects of radiation and dissociation on the flow field	84
6.6	Rebuilding results and comparison with test data	87
7	RESULTS: PARAFFIN-WAX CASE STUDY	93
7.1	Overview	93
7.2	Comparison between HTPB and paraffin-wax models	93
7.3	Experimental test cases	95
7.4	CFD grid and boundary conditions	97
7.5	General results for the reference test case	99
7.6	Radial profiles of temperature and species concentration	103
7.7	Wall heat flux contributions and regression rate evolution	105
7.8	Combustion and mixing modeling evaluation	107
7.9	Rebuilding results and comparison with test data	109
	Conclusions	117

LIST OF FIGURES

Figure 1	HRE combustion schematic.	1
Figure 2	Fuel droplet entrainment in a paraffin-based HRE (Credits Stanford).	3
Figure 3	Amroc HRE firing test at NASA Stennis Space Center in 1994 (Credits NASA).	7
Figure 4	Droplet entrainment in hydrocarbons (Credits Stanford). . .	13
Figure 5	Contributions to the surface mass balance.	30
Figure 6	Contributions to the surface energy balance.	30
Figure 7	Entrainment process schematic.	35
Figure 8	Supercritical entrainment model schematic.	35
Figure 9	Irradiation contributions through a layer, from [1].	40
Figure 10	Black body spectral emissive power [$W/m^2\mu m$] at different temperatures [K], from [1].	43
Figure 11	Planck-mean absorption coefficients for water vapor, carbon dioxide and carbon monoxide, after [2].	49
Figure 12	Infinitely long square cavity under consideration.	55
Figure 13	Comparison between exact and present DTM solution for $\tau = 1$	56
Figure 14	Comparison between exact and present DTM solution for $\tau = 0.1$	56
Figure 15	Comparison between exact and present DTM solution for $\tau = 10$	57
Figure 16	Convergence analysis of present DTM solutions in the case of $\tau = 1$	57
Figure 17	Convergence analysis of present DTM solutions in the case of $\tau = 0.1$	58
Figure 18	Convergence analysis of present DTM solutions in the case of $\tau = 10$	58

Figure 19	Sub-scale liquid rocket engine under consideration, from [3].	59
Figure 20	Comparison along different segments of integral wall heat flux measurements and computed convective and radiative contributions.	61
Figure 21	Convergence analysis of present DTM radiative wall heat flux predictions.	62
Figure 22	Methane density behavior, from [4].	64
Figure 23	Methane constant pressure specific heat behavior, from [4]. .	64
Figure 24	Normal-alkanes critical properties as a function of carbon number.	65
Figure 25	Liquid-like paraffin-wax constant pressure specific heat behavior with temperature.	68
Figure 26	Liquid-like paraffin-wax transport properties behavior with temperature.	68
Figure 27	Supercritical paraffin-wax thermal cracking rate constant. .	70
Figure 28	Gaseous-oxygen/HTPB lab-scale HRE schematic, from [5].	79
Figure 29	Adopted grid and boundary conditions, HTPB case study. .	81
Figure 30	Role of pressure and diameter on the medium global emissivity.	82
Figure 31	Ratio of radiative wall heat fluxes obtained with gray and black wall treatment.	84
Figure 32	Effects of radiation and dissociation on the computed temperature field.	85
Figure 33	Radiative wall heat flux profiles with and without considering dissociation.	86
Figure 34	Contributions to the wall heat flux, HTPB case study. . . .	87
Figure 35	Regression rate evolution with iterations, HTPB case study.	88
Figure 36	Port diameter effect on the flow field.	89
Figure 37	Port diameter effect on the radiative wall heat flux magnitude and profile.	90
Figure 38	Comparison between computed and measured regression rates, HTPB case study.	90

Figure 39	Comparison between computed and measured chamber pressures, HTPB case study.	91
Figure 40	Comparison of temperature fields with streamlines for paraffin-wax and HTPB.	94
Figure 41	Comparison of regression rate profiles for paraffin-wax and HTPB.	95
Figure 42	Gaseous-oxygen/paraffin-wax medium-scale HRE schematic (Credits Stanford).	98
Figure 43	Adopted grid and boundary conditions, paraffin-wax case study.	99
Figure 44	Temperature field with streamlines.	100
Figure 45	Comparison of radial profiles at the end of the grain length obtained with two different grid levels.	101
Figure 46	Mass fraction field of melted paraffin-wax.	102
Figure 47	Molar fraction fields of radiative species.	102
Figure 48	Mass fraction fields of radical species.	103
Figure 49	Radial profiles of temperature and species concentration at mid-grain location.	104
Figure 50	Radial profiles evolution along the grain length.	105
Figure 51	Contributions to the wall heat flux, paraffin-wax case study.	106
Figure 52	Regression rate evolution with iterations, paraffin-wax case study.	108
Figure 53	Evaluation of the combustion and mixing model.	109
Figure 54	Comparison of regression rate profiles between different test conditions.	111
Figure 55	Comparison between computed and measured regression rates, paraffin-wax case study.	112
Figure 56	Comparison between computed and measured chamber pressures, paraffin-wax case study.	113

Figure 57	Comparison between computed and measured regression rates including error bars and power fitting laws as a function of the oxidizer mass flux.	113
-----------	--	-----

LIST OF TABLES

Table 1	Liquid-like paraffin-wax thermodynamic properties coefficients [6, 7, 8].	66
Table 2	Liquid-like paraffin-wax transport properties coefficients [6, 7, 8].	67
Table 3	Supercritical paraffin-wax parameters for thermal cracking rate constant [9].	69
Table 4	Parameters of reaction rate constants for HTPB combustion without dissociations.	71
Table 5	Parameters of reaction rate constants for HTPB combustion including dissociations.	73
Table 6	Parameters of reaction rate constants for paraffin-wax combustion including dissociations.	75
Table 7	ORPHEE test campaign average data [10].	78
Table 8	HTPB chemical kinetics [11].	80
Table 9	HTPB grain properties [12, 13].	80
Table 10	Selected test case average data [14].	96
Table 11	Paraffin-wax grain properties [15, 16].	98
Table 12	Computed wall heat flux contributions.	110
Table 13	Computed chamber pressure, regression rate and mixture ratio.	110
Table 14	Errors between computed and measured regression rates and chamber pressures.	114

ACRONYMS

ABC	Asymptotic Behavior Correlations
AHRES	Advanced Hybrid Rocket Engine Simulation
CEA	Chemical Equilibrium with Applications
CFD	Computational Fluid Dynamics
CSM	Computational Solid Mechanics
GSI	Gas–Surface Interaction
HCF	Hybrid Combustion Facility
HDPE	High–Density Poly–Ethylene
HPDP	Hybrid Propulsion Demonstration Program
HRE	Hybrid Rocket Engine
HTPB	Hydroxyl–Terminated Poly–Butadiene
HYTOP	HYbrid Technology Option Project
MAV	Mars Ascent Vehicle
MON	Mixed Oxides of Nitrogen
MSR	Mars Sample Return
NASA	National Aeronautics and Space Administration
ODE	Ordinary Differential Equation
ORPHEE	Operational Research Project on Hybrid Rocket Engine in Europe
PDE	Partial Differential Equation
RANS	Reynold–Averaged Navier–Stokes

SBR	Styrene–Butadiene Rubber
SCVF	Stanford Combustion Visualization Facility
SEB	Surface Energy Balance
SMB	Surface Mass Balance
US	United States
VLES	Very Large Eddy Simulation

INTRODUCTION

In hybrid rocket engines (HREs) one of the propellants is stored at solid state and is physically separated from the other. Common HREs, in particular, rely on a solid fuel and a liquid or gaseous oxidizer. The latter propellant, injected into the grain port, reacts with the pyrolysis gas produced at the fuel grain surface. As a consequence, a diffusion flame, which in turn provides the convective and radiative heat flux needed to sustain the fuel pyrolysis process, is formed within the turbulent boundary layer [17]. A schematic of HRE combustion is shown in Figure 1.

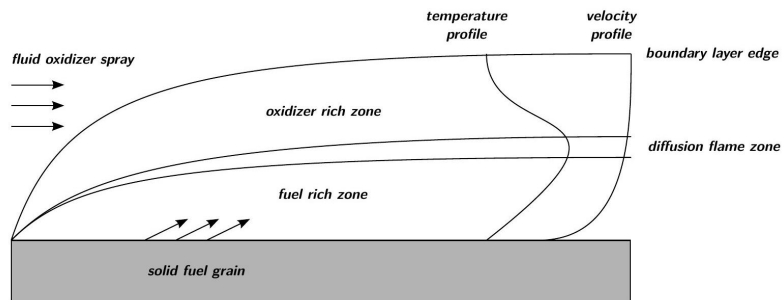


Figure 1: HRE combustion schematic.

Hybrid rocket engines present several advantages against solid rocket motors and liquid rocket engines. With respect to solid rocket motors, HREs are characterized by safety during fabrication, storage and operations, by throttling, shutdown and restart capabilities, a lower sensitivity to ambient temperature and a higher specific impulse. Compared to liquid rocket engines, on the other hand, they exhibit a greater simplicity and reliability, lower costs and higher propellant densities. Besides the mentioned advantages, HREs can have environmentally clean exhausts, without ecologically damaging compounds, and can allow the introduction of various additives, for both performance and density enhancement. In addition, the large range of performance achievable by HREs, together with throttling capabilities, makes them suitable for a wide range of applications, from launcher stages to in-space propulsion. There has been renewed interest in HREs in the last two

decades for such reasons, making this class of rocket engines considered as one of the envisaged options for future generation propulsion systems [18].

Despite the advantages of HREs, together with the experience gained during several decades, this class of rocket engines has almost never been developed for launcher or space vehicles. This essentially occurred because of a poor understanding of physical/chemical phenomena inside the motor, together with some intrinsic drawbacks of HRE operations, such as the shift in mixture ratio, the low combustion efficiency and the low regression rate. Especially the latter, significantly limited the possibility to attain high thrust levels in a easy and effective manner and, accordingly, the technology readiness level of HREs [18].

As mentioned, among the different shortcomings of conventional HREs, the low regression rate is one of the most significant. In fact, because of the diffusive nature of the flame, the regression rate of HRE solid fuels appears at least an order of magnitude lower than in solid rocket motors. So far, many techniques have been tried to improve the regression rate. Multi-port grains with a large wetted surface have been often employed to increase the fuel mass flow rate, but this led to several issues related to poor volumetric loadings and undesired fuel slivers [17]. An increase in regression rate up to seven times has been achieved by using swirl injection to create a coaxial counter-flowing vortex able to enhance both grain regression and heat transfer toward the surface [19]. To maintain a high level of swirl over the full length of the port and to scale this approach to larger motors has been found very challenging. Sometimes an oxidizing agent like ammonium perchlorate has been added to the fuel grain to make the regression rate also sensitive to chamber pressure, like in solid rocket motors. However, this approach removes the main safety advantage of the hybrid configuration [20]. Any technique aimed at enhancing the regression rate by increasing the heat transfer toward the fuel grain was also found ineffective because of the blocking effect. In fact, although increasing the heat transfer to the fuel grain enhances the rate of pyrolysis, the increased mass flux from the surface tends to reduce the temperature gradient at wall, thus limiting the heat transfer. All the attempts made to increase the regression rate without compromising the simplicity and safety of HREs have been largely unsuccessful until recently. The use of paraffin-based fuels appears nowadays as a very promising technique to solve the low regression rate problem [20].

It has been demonstrated that for paraffin-based fuels a liquid layer is formed on the grain surface. The hydrodynamic instability of the liquid layer, driven by the oxidizer gas flow in the port, can lead to the entrainment of fuel droplets into the gas stream, as illustrated in Figure 2. This additional mass transfer mechanism acts like a continuous spray distributed along the port, with most of the fuel vaporization occurring around droplets between the melt layer and the flame front. Because droplet entrainment is not limited by heat transfer to the fuel from the flame zone, the mechanism is not limited by the blocking effect and leads to much higher regression rates than conventional polymeric fuels [20]. Regression rates up to three to four times higher than the conventional values have been first observed in lab-scale motors and then confirmed in scale-up tests with different oxidizers. Paraffin-based fuels also provide theoretical specific impulses slightly higher than those of kerosene-fueled liquid rocket engines, together with an increase in propellant density. High regression rates allow to design high volumetric loading single-port combustion chambers, avoiding complex multi-port grains. In addition, paraffin-based fuels are non-hazardous, non-toxic, easy to handle and environmentally friendly [20].

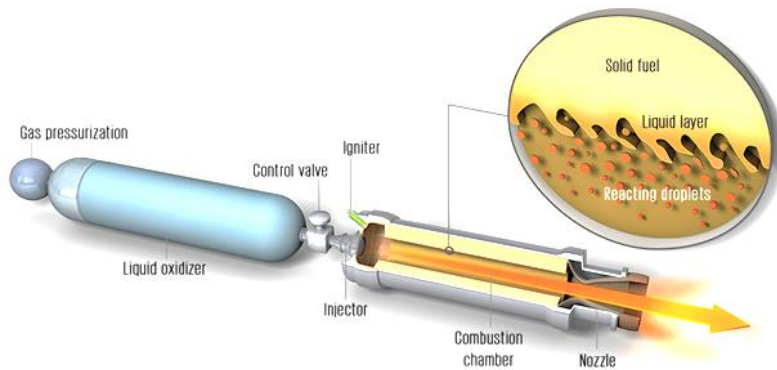


Figure 2: Fuel droplet entrainment in a paraffin-based HRE (Credits Stanford).

The present work is focused on the computational fluid dynamics (CFD) modeling of paraffin-based HREs aiming at developing predictive capabilities of the motor internal ballistics. In particular, the thesis is organized into two parts, after a state of the art survey is reported in Chapter 1. The first part, including Chapters 2–5, is devoted to present the proposed modeling approach for internal ballistics predictions of paraffin-based HREs. The second part, constituted by Chapters 6

and 7, is, on the other hand, aimed at showing the main results achieved by employing the aforementioned model, together with relevant comparisons against experimental data.

Chapter 2 describes the model employed as baseline for the present CFD simulations. The conservation principle in the form of the Navier–Stokes equations are recalled, together with some details about the modeling approach used for both combustion and turbulence. Next chapters give a panorama of the different modules developed to make the CFD solver able to deal with the physical/chemical phenomena of paraffin–based thrust chambers. In Chapter 3, a gas–surface interaction boundary condition, able to solve regression rate and mixture composition at wall in the case of liquefying fuels, is presented with the relevant surface mass and energy balances. In Chapter 4, focus is given to the model developed for radiative heat flux estimations, to be included into the surface energy balance. According to the model, the radiative transfer equation is integrated by discrete transfer method, dealing with inhomogeneous media within axisymmetric geometries. Finally, Chapter 5 shows the thermochemistry model implemented to describe paraffin–wax thermophysical properties, as well as paraffin–wax thermal cracking and successive combustion with gaseous–oxygen, including dissociations.

Chapter 6 shows results obtained by considering conventional pyrolyzing fuels, with the objective to analyze the coupling of the different physical sub–models, by leaving out the additional assumptions made specifically for the case of paraffin–wax. Particular attention is given to the role played by thermal radiation and dissociation reactions, as well as their mutual coupling, before presenting comparison against experimental data with a validation purpose. Chapter 7 is finally focused on the results obtained with the full model for paraffin–wax regression and combustion. The ability of the solver to capture the temperature and composition fields, as well as the different wall heat flux contributions, is highlighted. Selected firing tests from experimental campaigns are also numerically rebuilt to show up the model capabilities to predict the motor internal ballistics under different mass flux and chamber pressure conditions.

STATE OF THE ART

1.1 BRIEF OVERVIEW OF HYBRID ROCKET HISTORICAL BACKGROUND

The development of HREs started in the 1930s, when also solid and liquid rockets were at their initial development phase. The first work with HREs was carried out in Russia in 1933 when a 500 N rocket burning liquid–oxygen with gelled–gasoline reached 1.5 km altitude [21]. In the late–1940s the Pacific Rocket Society flew another HRE, burning liquid–oxygen with a rubber–based fuel, reaching an altitude of 10 km. Few years later, in the early–1950s, the General Electric Company made analytical and experimental investigations burning hydrogen–peroxide and poly–ethylene, for performance augmentation purposes. In the 1960s an era of fundamentals studies started with an increased interest in research on hybrid propulsion by United States (US) military forces and private companies. Extensive motor testing activities were carried out and several theoretical results were obtained. One of the greatest accomplishments of that period was the development of fundamental regression rate models. Some large size HREs were also designed and tested in the US and Europe, achieving thrust levels of 20 kN and specific impulses up to 400 s (by using exotic propellant solutions involving fluorine/oxygen mixtures as oxidizer) [21]. Few informations can be found on the activities performed in the 1970s, mainly focused on the design of HRE–powered sounding rockets. Anyway, such studies, together with the experience gained in large size HRE tests, paved the way for the development of important programs on hybrid propulsion across the 1980s and 1990s. In 1981 the Starstrack company was created to develop a 155 kN thrust–class HRE. Using liquid–oxygen and a multi–port grain of poly–butadiene, six full–scale static firings were performed. In 1985 the company was renamed Amroc, and started to design HREs in a range of thrust between 25 kN and 1.1 MN, with the same propellant combination. In the following seven years 124 static firings were made, more than a dozen with a 335 kN thrust

level, the largest HRE ever tested at that time [21]. Both Starstrack and Amroc failed the launch of the HRE-powered sounding rockets they developed. Despite such failures, the idea of launching a 1.1 MN rocket motor, as first or second stage of a launch vehicle continued. During 1993 and 1994, the so-called hybrid technology option project (HYTOP) was joined by other companies and supported by the national aeronautics and space administration (NASA). Different firing tests were carried out (one of them is illustrated in Figure 3), but after a small burning time, the motor suffered from a low frequency combustion instability [21]. A new hybrid propulsion demonstration program (HPDP), was started with Thiokol taking the place of Amroc. A multi-port wagon wheel fuel grain of hydroxyl-terminated poly-butadiene (HTPB) was fired with short burning times in 1999. The engine exhibited large pressure oscillations and unequal burning rates in the various ports. Eventually, stable combustion was achieved, but the problem of low volumetric loading remained [21]. In the meantime, starting from the early 1990s, several US research groups began to investigate cryogenic fuels. During tests with cryogenic hydrocarbons, such as methane and pentane, regression rates up to ten times higher than those of classical polymeric fuels were found [22, 23, 24, 25]. After many series of tests and experimental analyses, researchers from Stanford University developed and extended to non-cryogenic hydrocarbons a mathematical theory showing the entrainment phenomena as responsible of such an apparently strange behavior [26, 27]. In particular, paraffin-waxes were found to be characterized by regression rates from three to four times higher than conventional pyrolyzing fuels. Such findings lead to an increased interest in hybrid rocket research in the following two decades. To date, the most successful flight of a HRE has been achieved in 2004 when the Space Ship One reached an altitude of 100 km by using nitrous-oxide in a four-port HTPB fuel grain. Although this was a major success for HREs, the performance required to the engine was far from that needed to lift-off a payload to orbit [20].



Figure 3: Amroc HRE firing test at NASA Stennis Space Center in 1994 (Credits NASA).

1.2 FUNDAMENTAL ANALYSES OF HYBRID ROCKET REGRESSION RATE

Fundamental analyses of hybrid rocket combustion have relied on boundary-layer assumptions to determine the fuel grain regression rate. Various types of analyses have been developed by identifying different controlling mechanisms, such as heat transfer, mass diffusion, pressure dependence and gas or solid-phase reactions. Probably the most thorough and influential theory of hybrid rocket combustion was developed in the early 1960s by Marxman *et al.* at the United Technology Center in Sunnyvale, California [28, 29]. Such theory proposed an important heat transfer limited regression rate model suggesting that the solid fuel regression rate depends mainly on the heat transfer from the gas phase toward the grain surface. An important implication of the theory developed by Marxman is the weak dependence of the regression rate on the enthalpy difference between the flame and the fuel surface because of the blocking effect, so that many different types of solid fuels exhibit similar regression rates. Another significant implication of the Marxman's theory is that the injected fuel mass flow rate, and hence the

regression rate, are only a function of the mass flux in the port, G , according to the relation:

$$\dot{r} \propto aG^n \quad (1)$$

with a being a constant depending essentially on the propellant combination and the turbulence level and n an exponent with values in between 0.6 and 0.8. Since for a given oxidizer mass flow rate G decreases as the port area increases during the burn the regression rate is expected to decrease with time. At the same time, since G depends, at a certain axial position, on both the oxidizer flowing into the port and the fuel injected upstream of such position, the regression rate is expected to increase with the axial location along the fuel grain. After Marxman's pioneering works, different theories, correlations and numerical procedures have been often proposed to examine the burning behavior of hybrid rockets. Various schools attributed the regression rate limiting mechanism to different controlling parameters, as well as examined deviations from Marxman's law due to thermal radiation or chemical kinetics effects [30]. None of those simplified analyses, however, was able to account for the many complex physical/chemical interactions occurring in hybrid rockets. More comprehensive models based on CFD have been found necessary to analyze and understand parametric trends as well as to provide design and development tools [31].

1.3 CFD MODELING OF HYBRID ROCKET FLOW FIELDS

With regard to the CFD modeling, it is worth to note that in hybrid rocket flow fields, the fluid dynamic and chemical time scales are much smaller than the one governing the fuel regression. For this reason steady-state solutions appear adequate for predicting the regression rate, as well as motor efficiency or scale-up effects. The main interest in simulating hybrid rockets by means of CFD is therefore to obtain steady-state flow fields. This can be accomplished by solving the Reynolds-averaged Navier-Stokes (RANS) equations, with suitable turbulence closure models. Besides the equations of motion and the suitable description of turbulence, several sub-models are required to represent the fuel surface pyrolysis and regression, thermal radiation effects and gas-phase chemistry. The surface

pyrolysis and regression should be evaluated by treating the coupling between the solid and gaseous phase through a suitable boundary condition based on mass and energy balances at the interface. A surface pyrolysis description, which can potentially rely on semi-empirical models, is also needed to close the problem by relating the wall temperature to the injected fuel mass flux. Both theoretical and experimental studies indicate that thermal radiation may be a significant contributor to the energy balance on the fuel surface, with a greater relative importance at low mass fluxes. These observations highlight the need to include a model for radiative heat transfer to accurately predict the fuel regression rate. Gas-phase chemistry should be also included to account for combustion. Since non-equilibrium conditions can be found in the flow field, finite-rate chemistry should be employed for accurate predictions. At the same time, because of the high computing effort associated with detailed chemical kinetics mechanisms, involving several tens of species and hundreds of elementary reaction steps, global combustion models are generally adopted [31].

One of the first attempts to apply a RANS approach was that by Sankaran in Refs. [30, 31], where the slab burner experimental results obtained by Chiaverini *et al.*, and presented in Refs. [32, 33] have been rebuilt. A very simplified model, calibrated on experimental measurements, was adopted for thermal radiation. At the same time, a two steps global reaction mechanism was employed to evaluate combustion between gaseous-oxygen and the main pyrolysis product of HTPB. Results appeared fairly in qualitative agreement with Marxman's boundary layer theory. The regression rate was found to decrease during the burn because of the reduction of the mass flux as the port opens up. Furthermore, the regression rate was confirmed to increase along the fuel grain because of the mass addition effect which results in an increase in the total mass flux as the flow moves downstream into the port. Besides such findings, analyses of scale-up effects showed that the ratio between the flame distance from the fuel surface and the port radius decreases with motor dimension, leading to a reduction of the combustion efficiency for large-scale motors. At the same time, since the absolute flame distance from the fuel surface was found to increase anyway, a reduction of the temperature gradient at wall was observed, as well as a decrease in the convective heat flux. Despite the higher volumetric radiative source associated with larger dimensions was found

to increase thermal radiation effects, the convective flux reduction was found to be strong enough to reduce the total heat flux and, accordingly, the regression rate, in the case of large-size motors [31]. By using a commercial Navier–Stokes solver, CFD–ACE, also Serin and Gogus simulated the gaseous–oxygen/HTPB slab burner developed and tested by Chiaverini *et al.*. In particular, surface pyrolysis capabilities and simplified radiative modeling were included [34]. The Chiaverini *et al.* slab burner has been also recently the subject of study of Gariani *et al.*. In the OpenFOAM framework they used a RANS solver, coupled with a global reaction mechanism including dissociations to compute finite–rate chemistry. The regression rate, in particular, has been computed by iteratively solving the wall energy balance. A suitable pyrolysis model has been used, while thermal radiation has been included according to the lowest order approximation, i.e. P1 approximation, of the spherical harmonic method. The numerical results appeared in good agreement with experimental data [35].

Approaches similar to that of Sankaran, also with multi–phase predictions of liquid–oxygen droplet atomization, but lacking of suitable gas–surface interaction (GSI) modeling, were reported by Cheng *et al.* and Liang *et al.* [36, 37]. A proper GSI model was added to a multi–phase simulation framework by Lin *et al.* [38].

More recently, Bianchi *et al.* analyzed via CFD simulations two entire test campaigns performed by Carmicino and Russo Sorge [39, 40] using a lab–scale gaseous–oxygen/HTPB HRE. An in–house RANS solver with GSI capabilities, finite–rate chemistry with two reaction steps and turbulence closure by means of a Spalart–Allmaras one equation model were adopted. They confirmed the experimental evidence of a regression rate enhancement associated with axial injection, together with the effect of port diameter on such phenomenon [41, 5]. In addition, despite the lack of thermal radiation modeling, they were able to capture the main features of the motor internal ballistics over the whole set of experimental data. Di Martino *et al.* also simulated some test cases performed with the experimental setup of Carmicino and Russo Sorge. In particular, two different motor scales and the gaseous–oxygen/high–density poly–ethylene (HDPE) propellant combination have been investigated. The commercial CFD solver ANSYS–Fluent has been used, while the GSI capabilities have been implemented through user–defined functions. At the same time, an equilibrium with a probability density function approach has

been used for chemistry, while a κ - ω model has been employed to close the set of RANS equations. Also in these cases no radiation modeling has been considered. However, an iterative procedure able to account for grain geometry evolution with time has been introduced. The results showed a fairly good agreement with experimental data. In addition, performances of different injector configurations and nozzle materials have been analyzed [42, 43]. The firing tests performed by Carmicino and Russo Sorge with the gaseous-oxygen/HDPE propellant combination have been simulated with the commercial CFD solver CFX also by Lazzarin *et al.*. A RANS approach with a single reaction step finite-rate chemistry and a κ - ϵ turbulence closure model has been used. Different simplified approaches to model the fuel grain regression rate have been adopted, from that of directly enforcing the experimental value to that of deriving an average value from the computed heat flux, either neglecting or including the radiative contribution. Results showed a limited under-estimation of the characteristic velocity when the experimental regression rate has been enforced. At the same time, a strong underestimation of regression rate, when computed from the heat flux, has been found. To include the contribution of radiative heat transfer appeared crucial to mitigate such errors [44]. With the same numerical setup Faenza *et al.* also simulated the gaseous-oxygen/HTPB propellant combination. In particular, they included *via* user-defined functions an iterative procedure able to calculate the wall temperature and the regression rate from the convective heat flux. A better agreement with experimental data has been found in this case [45].

May and Bozic performed with their in-house code both 2D and 3D RANS reactive simulations of the advanced hybrid rocket engine simulation (AHRES) lab-scale HRE, relying on hydrogen-peroxide into multi-port HTPB grains. They used a very accurate global reaction mechanism involving 12 species and 22 reaction steps. However, the regression rate was directly evaluated from the pyrolysis model by enforcing a uniform temperature at wall and no thermal radiation was modeled, accordingly. May and Bozic showed a local regression rate increase associated with higher velocity in the near-wall regions caused by vortices [46].

Recently, Chen *et al.* carried out preliminary numerical investigations of mixture ratio shift and performance behavior over time of different propellant combinations involving nitrous-oxide and hydrogen-peroxide as oxidizers and HTPB,

HDPE and styrene–butadiene rubber (SBR) as fuels. They used a reactive very large eddy simulation (VLES) approach using global reaction mechanisms with a high number of species and reaction steps. They also considered real fluid thermodynamics, together with non–standard pyrolysis models and gray gas phase radiation to solve the wall energy balance and compute the grain regression rate [47, 48].

It should be noted that radiative heat transfer has been rather rarely considered in the different proposed model of HRE internal ballistics. In addition, very few works have reported informations about the share of the radiative contribution to the total wall heating. Among them, Sankaran [31] predicted a radiative contribution up to 25% for lab–scales and further increases with motor dimensions. Lazzarin *et al.* [44] showed a central role of the radiative wall heat flux in regression rate predictions, with contributions of approximately 50%. Finally, Serin *et al.* [34] highlighted a dominant contribution of the gas phase with respect to that of soot, predicting a 7% contribution due to thermal radiation.

1.4 RESEARCH ACTIVITIES ON PARAFFIN–BASED HYBRID ROCKET ENGINES

The milestone of paraffin–based fuels investigations is the study carried out at Stanford University by Karabeyoglu *et al.* on the combustion of liquefying propellants. First, the formation of a melt layer was found and its linear stability under high shear stresses investigated. As a second step, the melt layer instability was linked to droplet entrainment by using experimental results and semi–empirical correlations from film–cooling literature. Finally, the Marxman’s regression rate theory was extended to the case of liquefying propellants [26, 27]. The entrained mass flow rate, in particular, was found directly proportional to dynamic pressure p and melt layer thickness h and inversely proportional to dynamic viscosity μ and surface tension σ according to the relation:

$$\dot{m}_{ent} \propto \frac{p^\alpha h^\beta}{\mu^\gamma \sigma^\delta} \quad (2)$$

In practice, the primary parameter characterizing the tendency for a fuel to entrain is the viscosity, which varies greatly from one fuel to another. The surface tension, on the other hand, is the less important discriminator since it tends to be relatively constant for a wide range of fuels and is not defined at supercritical pressures,

as may occur in HRE thrust chambers [20]. Looking at Figure 4, paraffin-waxes appear, among normal-alkanes that are solid at room temperature, those to exhibit the highest entrainment and, accordingly, expected to have the highest regression rates. The burning rate of the paraffin-wax fuel formulation as a function of mass flux was in fact found approximately from three to four times higher than the burning rates of HTPB. Experiments conducted with gaseous-oxygen on a lab-scale HRE at Stanford University confirmed the theory predictions [49]. To further demonstrate the feasibility of the proposed approach, a series of scale-up tests with gaseous-oxygen were carried out in the hybrid combustion facility (HCF) at NASA Ames Research Center [50]. Data from these tests were found in agreement with the lab-scale, low pressure and low mass flux laboratory tests performed at Stanford University. Such tests confirmed the high regression rate behavior of paraffin-based fuels at chamber pressures and mass fluxes representative of flight applications [14].

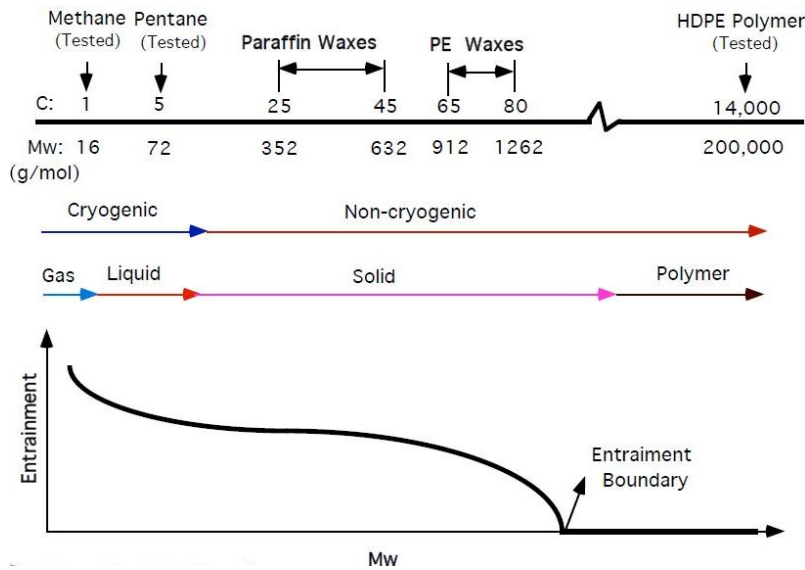


Figure 4: Droplet entrainment in hydrocarbons (Credits Stanford).

The mentioned theoretical and experimental findings on high regression rate liquefying fuels generated a renewed interest in visualization experiments. Nakagawa and Nikone published images of the combustion of paraffin-wax fuel grains with gaseous-oxygen at atmospheric pressure. The images clearly showed droplets lifted off from the fuel surface burning in the oxygen free stream. The low pressures and oxidizer mass fluxes made relatively easy to detect droplets but were

quite far from actual hybrid rocket conditions [51]. Chandler *et al.* designed a test article named Stanford combustion visualization facility (SCVF) with side and top accesses for high speed cameras. Results showing unsteady roll waves and droplet entrainment during the combustion of paraffin-wax with gaseous-oxygen at atmospheric pressure were presented. The experimental campaign proved the presence of the droplet entrainment mechanism at ambient pressure. At the same time, tests with conventional fuels confirmed the presence of a stable melt layer, without any droplet entrainment event, for HDPE, and the absence of both liquid layer and droplet injection in the case of HTPB [52]. A number of modifications were made to the CVF by Jens *et al.* to accommodate Schlieren imaging capability, facilitate repeatable test conditions and make the apparatus able for testing at higher pressures. The first high speed visualizations and Schlieren images of paraffin-wax and gaseous-oxygen combustion at supercritical pressures were obtained. The nature of the combustion was seen to change dramatically with increasing pressure. Entrained filament structures were not the dominant detectable feature, while numerous intense blowing events were observed [53]. Kobald *et al.* presented Schlieren images of the combustion of paraffin-wax and gaseous-oxygen at atmospheric pressure. However, they showed the droplet entrainment to occur only during start-up and shut-down transients [54]. More recently, Petrarolo *et al.* continued such investigation by running firing tests with gaseous-oxygen in a slab burner while using high speed imaging with different decomposition techniques. Both the liquid layer instability process and the formation of wave-like structures have been confirmed. The role played by different viscosities, geometries and mass flow rates has been also identified [55, 56].

Adachi and Shimada came back on the instability analysis of liquid films looking at supercritical conditions, as those actually occurring in HRE operations. Methane fuel was investigated as representative of liquefying propellants and a real fluid behavior was taken into account by using the Van der Waals equation of state. By ignoring both combustion and radiation, the flow field was represented as a Couette flow. The steady state solution was then perturbed and analyzed in the non-linear range. A limit cycle was found for low Reynolds numbers, while the droplet entrainment phenomenon was observed at higher turbulence regimes [57].

From the experimental side, Narsai *et al.* applied an image processing technique to obtain time-varying port area measurements in a lab-scale paraffin-based HRE. The objective of such direct imaging technique was to allow inherently less ambiguous estimations with respect to traditional measurements by avoiding averaging processes. The technique was confirmed to be very effective since the time-varying estimated regression rate parameters matched generally well with published data [58]. In the meantime, Santi *et al.* proved the feasibility of paraffin-based HREs in actual mission scenarios by carrying out long burning firing tests, up to 80 seconds. Besides the combustion stability, the test campaign showed that the heat flux does not penetrate in depth into the fuel grain, since almost ambient temperature conditions was measured by embedded thermocouples. The integrity of paraffin-wax mechanical properties along the whole burn was proved accordingly [59].

Some engineering models have been also recently developed. Funami *et al.* developed a simplified melt layer model with the purpose of integrating it into a proper design tool [60]. Similarly, Lestrade *et al.* developed a one-dimensional code for regression rate and performance predictions of their experimental apparatus [61].

Looking to future technology development plans, Chandler *et al.* are currently working on a Mars ascent vehicle (MAV) relying on a paraffin-based hybrid rocket as the main propulsion system. Their objective, in particular, is to increase the technology readiness level of paraffin-based HREs for in-space and planetary exploration applications by developing a MAV technology demonstrator. The compactness, combined with the relatively high achievable performances, together with restart and low temperature capabilities, in fact, makes the paraffin-based HRE concept an ideal candidate to carry out the return-leg of future Mars sample return (MSR) missions [62]. In this framework, Evans and Karabeyoglu developed and tested a paraffin-based fuel with low temperature capabilities for a MAV application. Several firing tests with either mixed oxides of nitrogen (MON) or nitrous-oxide have been carried out proving ignition, stable combustion and good overall performances. The firing tests also demonstrated the ability of the fuel to meet the propulsion requirements of a potential MSR mission while allowing to identify proper regression rate laws with both the envisaged oxidizers [63].

1.5 CFD ACTIVITIES ON PARAFFIN-BASED HYBRID ROCKET ENGINES

Few works about CFD modeling and simulation of paraffin-based HREs can be found in the open literature. To support experimental activities and understand basic aspects on nitrous-oxide/paraffin-wax HREs, such as vortex or liquid injection, as well as scale-up effects, Bellomo *et al.* performed a series of CFD simulations by using commercial software. Turbulence has been described by means of a κ - ϵ model, while a simple equilibrium chemistry has been employed. The fuel mass flux has been enforced without solving any wall balance. In particular, a gas mixture of ethylene and hydrogen at paraffin-wax boiling temperature has been assumed and injected from the fuel grain. No thermal radiation nor droplet entrainment model has been employed in the computation. In Ref. [64] a role of vortex injection in enhancing mixing, and hence in improving the combustion efficiency, has been detected. In Ref. [65] the importance of a liquid injection model to reproduce experimental results of different motor scales has been highlighted. The nitrous-oxide/paraffin-wax propellant combination has been also investigated by Ranuzzi *et al.* in Ref. [66]. An in-house finite-volume RANS solver for turbulent and reactive gaseous-mixtures has been employed to reproduce an experimental test case. Both κ - ϵ and κ - ω models have been used to evaluate turbulence effects. Finite-rate chemistry with a single step global reaction mechanism has been used for computing combustion. Also in this case the experimental fuel mass flux has been directly enforced as an inflow boundary condition at the fuel grain wall, while radiation and entrainment effects have been neglected. Results in terms of achieved chamber pressure have been found in good agreement with experimental data, with errors ranging between 10% and 18%, depending on the adopted turbulence model. Similar results have been found by simulating the reference test case with a commercial software. Both a cryogenic injection and a turbulence-chemistry interaction model have been also developed and validated against experimental data with the objective to include them into the numerical solver for future computations. A first approach to solve mass and energy balances at wall and compute paraffin-based fuel regression rates has been proposed by Bianchi *et al.* in Ref. [16]. The proper gas-surface interaction model has been implemented

into a finite volume RANS solver for compressible, turbulent, multispecies and reactive flows. A single equation Spalart–Allmaras turbulence closure model has been employed, while a two steps global mechanism has been used to compute finite-rate chemistry. A numerical test case with gaseous–oxygen has been simulated for both HTPB and paraffin–based fuel combinations. In the latter case, the balances have been solved in a parametric way with varying wall temperature because of the lack of available correlations between wall temperature and fuel mass flux. Regression rates from about two to more than four times higher than HTPB have been computed in the case of paraffin–wax depending on the assumed wall temperature, between paraffin–wax melting and boiling points. The role of increased wall temperature has been found to decrease the regression rate because of the reduced convective heat flux toward the wall. However, the radiative heat flux has not been modeled, as well as the droplets entrainment into the gas stream.

2.1 CONSERVATION PRINCIPLES

The fluid dynamics model relies on the turbulent and reactive set of Navier–Stokes equations, expressing mass, momentum and energy conservation within a generic control volume. Chemical reactions are accounted for by using a number of mass conservation equations consistent with the number of species constituting the mixture, as well as by suitably modeling chemical source terms. Turbulence effects are taken into account by using RANS equations, properly closed by an additional equation accounting for turbulent viscosity.

The integral form of the species mass conservation is given by the following scalar equation:

$$\frac{d}{dt} \int_V \rho_i dV + \oint_S \rho_i \mathbf{u} \cdot \mathbf{n} dS = - \oint_S \rho_i v_i dS + \int_V \dot{\omega}_i dV \quad (3)$$

where \mathbf{u} is the mixture velocity, v_i is the i -th species diffusion velocity, ρ_i is the i -th species density and $\dot{\omega}_i$ is the i -th species chemical production/destruction rate. Notice that by summing up all the species continuity equations, the mass conservation for the gas mixture is obtained:

$$\frac{d}{dt} \int_V \rho dV + \oint_S \rho \mathbf{u} \cdot \mathbf{n} dS = 0 \quad (4)$$

because of the mixture density definition:

$$\rho = \sum_{i=1}^N \rho_i \quad (5)$$

as well as the null contributions:

$$\sum_{i=1}^N \dot{\omega}_i = 0 \quad (6)$$

$$\sum_{i=1}^N \rho_i v_i = 0 \quad (7)$$

The integral form of the momentum conservation is given by the following vectorial equation:

$$\frac{d}{dt} \int_V \rho \mathbf{u} dV + \oint_S (\rho \mathbf{u} \cdot \mathbf{n}) \mathbf{u} dS = \int_V \rho \mathbf{f} dV + \oint_S \mathbf{t} dS \quad (8)$$

where ρ is the mixture density and \mathbf{f} and \mathbf{t} are the volume and surface forces, respectively. The surface forces vector, in particular, can be expressed as the scalar product between the stress tensor, decomposed in a spherical and a viscous component, and the normal to the surface:

$$t_l = \sigma_{lm} n_m = (-p \delta_{lm} + \tau_{lm}) n_m \quad (9)$$

while the spherical component is related to the mixture pressure, the viscous component of the stress tensor is, in turn, given by the Newton's law:

$$\tau_{lm} = \mu \left(\frac{\partial u_l}{\partial x_m} + \frac{\partial u_m}{\partial x_l} - \frac{2}{3} \frac{\partial u_n}{\partial x_n} \delta_{lm} \right) \quad (10)$$

with μ being the mixture dynamic viscosity.

The integral form of the energy conservation is given by the following scalar equation:

$$\frac{d}{dt} \int_V \rho e_0 dV + \oint_S (\rho \mathbf{u} \cdot \mathbf{n}) e_0 dS = \int_V \rho \mathbf{f} \cdot \mathbf{u} dV + \oint_S \mathbf{t} \cdot \mathbf{u} dS - \oint_S \mathbf{q} \cdot \mathbf{n} dS \quad (11)$$

where e_0 is the mixture internal energy and \mathbf{q} is the heat flux. The heat flux vector, in particular, can be expressed through a diffusive and a convective contribution given by Fourier's law:

$$q_l = \sum_{i=1}^N \rho_i u_{i,l} h_i - k \frac{\partial T}{\partial x_l} \quad (12)$$

with k being the mixture thermal conductivity.

2.2 EQUATION OF STATE

The mixture is assumed to be composed of thermally perfect gases. According to this assumption, mixture pressure p and temperature T are related with each other by the well known equation of state:

$$p = \rho RT \quad (13)$$

where the mixture gas constant R is given by:

$$R = \frac{\mathcal{R}}{M} = \sum_{i=1}^N Y_i R_i = \mathcal{R} \sum_{i=1}^N \frac{Y_i}{M_i} \quad (14)$$

with \mathcal{R} being the universal gas constant, M the mixture molar mass, R_i the i -th species gas constant, M_i the i -th species molar mass and Y_i the i -th species mass fraction.

2.3 THERMOPHYSICAL PROPERTIES

According to the thermally perfect gas assumption, the single species thermophysical properties are described as a function of temperature only.

Thermodynamics properties of species are described by seventh-order polynomials of temperature using the chemical equilibrium with applications (CEA) database [67] for the relevant coefficients. In particular, constant pressure specific heat $c_{p,i}$, enthalpy h_i and entropy at atmospheric pressure s_i are expressed as polynomials:

$$\frac{c_{p,i}}{R} = \frac{a_1}{T^2} + \frac{a_2}{T} + a_3 + a_4 T + a_5 T^2 + a_6 T^3 + a_7 T^4 \quad (15)$$

$$\frac{h_i}{RT} = -\frac{a_1}{T^2} - \frac{a_2}{T} \ln T + a_3 + a_4 \frac{T}{2} + a_5 \frac{T^2}{3} + a_6 \frac{T^3}{4} + a_7 \frac{T^4}{5} + \frac{b_1}{T} \quad (16)$$

$$\frac{s_i}{R} = -\frac{a_1}{2T^2} - \frac{a_2}{T} + a_3 \ln T + a_4 T + a_5 \frac{T^2}{2} + a_6 \frac{T^3}{3} + a_7 \frac{T^4}{4} + b_2 \quad (17)$$

Mixture thermodynamics properties are then evaluated by:

$$c_p = \sum_{i=1}^N Y_i c_{p,i} \quad (18)$$

$$h = \sum_{i=1}^N Y_i h_i \quad (19)$$

$$s = \sum_{i=1}^N Y_i s_i \quad (20)$$

Transport properties of species are described by fourth-order polynomials of temperature also according to CEA. Molecular viscosity μ_i and thermal conductivity k_i are expressed as:

$$\ln \mu_i = A_\mu \ln T + \frac{B_\mu}{T} + \frac{C_\mu}{T^2} + D_\mu \quad (21)$$

$$\ln k_i = A_k \ln T + \frac{B_k}{T} + \frac{C_k}{T^2} + D_k \quad (22)$$

The diffusion coefficient D_i is considered to be the same for all species through a constant Schmidt number:

$$D_i = D = \frac{\mu}{\rho S_c} \quad (23)$$

Mixture viscosity and thermal conductivity are then derived from Wilke's semi-empirical rule [68]:

$$\mu = \frac{\sum_{i=1}^N X_i \mu_i}{\sum_j X_j \phi_{ij}} \quad (24)$$

$$k = \frac{\sum_{i=1}^N X_i k_i}{\sum_j X_j \phi_{ij}} \quad (25)$$

with the ϕ_{ij} coefficients given by:

$$\phi_{ij} = \frac{1}{\sqrt{8}} \left(1 + \frac{M_i}{M_j}\right)^{-1/2} \left[1 + \sqrt{\frac{\mu_i}{\mu_j}} \left(\frac{M_j}{M_i}\right)^{1/4}\right]^2 \quad (26)$$

2.4 CHEMICAL SOURCE TERMS

Chemical reactions are modeled according to a finite-rate approach, hence by assuming the transformation of reactants into products species to occur through a sequence of chemical non-equilibrium states. The overall reaction process is then computed through its evolution in time, i.e. the series of intermediate reaction steps.

To account for finite-rate chemistry, the chemical source terms $\dot{\omega}_i$ in Eq. (3) are required for each species $i = 1, \dots, N$. Each reaction $j = 1, \dots, M$ that involves the

i -th species, in particular, contributes to the i -th source term through the relevant reaction rate v_j according to the law of mass action:

$$v_j = k_{j_f} \prod_{i=1}^N [\cdot]_i^{v_{ij}^r} - k_{j_b} \prod_{i=1}^N [\cdot]_i^{v_{ij}^p} \quad (27)$$

where $[\cdot]_i$ is the concentration of the i -th species, v_{ij} is the stoichiometric coefficient of the i -th species in the j -th reaction, with superscripts r and p indicating reactants and products, respectively, and k_j is the reaction rate constant relevant to the j -th reaction, with subscripts f and b indicating the forward and backward directions, respectively. Notice that reaction rate constants are expressed with an Arrhenius-type equation:

$$k_j = A_j T^{n_j} \exp\left(-\frac{E_{a_j}}{RT}\right) \quad (28)$$

where A_j is the pre-exponential factor, n_j the temperature exponent and E_{a_j} the activation energy of the j -th reaction. Once the reaction rates are known, the source terms can be easily evaluated according to:

$$\dot{\omega}_i = M_i \sum_{j=1}^M \Delta v_{ij} v_j \quad (29)$$

where Δv_{ij} is the difference of the stoichiometric coefficients in the reaction direction of the i -th species in the j -th reaction.

In the present work, finite-rate chemistry is modeled by global reaction mechanisms. In fact, detailed chemical kinetics mechanisms are both computationally heavy and not strictly needed to achieve an accurate internal ballistics prediction. Global reaction mechanisms, in particular, involve a reduced number of reaction steps with v_{ij} exponents and k_j constants obtained from experimental investigations performed under prescribed operating conditions.

2.5 TURBULENCE CLOSURE EQUATION

Turbulence effects, such as mixing enhancement, are modeled by exploiting the property of a turbulent flow to have clean and steady mean properties despite its chaotic change of velocity, tridimensional and irregular vorticity distribution

and continuous dependence on initial conditions. Each flow variable ϕ is, in fact, decomposed into an average $\bar{\phi}$ and fluctuating component ϕ' , according to:

$$\phi = \bar{\phi} + \phi' = \frac{\overline{\rho\phi}}{\rho} + \phi' \quad (30)$$

and substituted into the conservation principles to obtain RANS equations. For such averaged equations, the Reynolds stress tensor, that represents the dissipation due to field oscillations, appears unclosed. This point is overcome by expressing the Reynolds stress tensor as a function of averaged variables and, in particular, according to the Boussinesque assumption, as a function of the mean velocity gradient, by analogy with viscous stresses. In this way the problem of unclosed equations is transferred to the description of turbulent viscosity by a suitable model.

The one equation turbulence closure model by Spalart and Allmaras is employed in the present work [69]. In this model the Reynolds stress tensor is assumed to be related to the strain rate tensor through the turbulent viscosity μ_T :

$$-\rho\overline{u'_i u'_j} = \mu_T S_{ij} \quad (31)$$

while the turbulence closure equation is written in terms of an auxiliary intermediate variable $\tilde{\nu}$ defined as:

$$\tilde{\nu} = \frac{\mu_T}{\rho f_{v1}} \quad (32)$$

with f_{v1} a damping coefficient. The additional partial differential equation (PDE) for turbulent viscosity computation [69] is given by:

$$\frac{D\tilde{\nu}}{Dt} = b_{prod}(S, \tilde{\nu}) - b_{dest}(\tilde{\nu}, d) + \frac{1}{\sigma} [\nabla \cdot ((\nu + \tilde{\nu})\nabla\tilde{\nu}) + c_{b2}\nabla\tilde{\nu}]^2 \quad (33)$$

where the different terms account for production, destruction and diffusion/convection of $\tilde{\nu}$, respectively. The Spalart–Allmaras turbulence model appears suitable for complex internal, external and boundary layer flows, economical for large meshes, simpler than two equation models with good performances in the case of separation. Once the turbulent viscosity is known, turbulent thermal conductivity k_T and turbulent diffusion D_T are determined from the constant pressure specific heat by assuming constant turbulent Prandtl and Schmidt numbers:

$$k_T = \frac{\rho\nu_T c_p}{Pr_T} \quad (34)$$

$$D_T = \frac{\nu_T}{Sc_T} \quad (35)$$

2.6 NUMERICAL METHOD

The adopted in-house RANS solver is developed to treat three-dimensional, turbulent, compressible, multi-component and reacting flows. The interaction between turbulence and chemical kinetics is computed according to a laminar flame model. The solver adopts a second order accurate in space finite volume Godunov formulation [70]. To allow the second order accuracy in space, a linear cell reconstruction of flow variables is carried out by using the value in the considered cell and those in the contiguous ones. A Roe approximate Riemann solver [71] for multi-block structured meshes is used. This allows to evaluate variables at cell interfaces and associated fluxes to compute the evolution in time. Time integration is based on the Strang operator-splitting technique [72], with convective and diffusive terms integrated by a second-order Runge-Kutta scheme, whereas for the chemical source term a stiff ordinary differential equation (ODE) implicit integrator is used [73]. The solver has been verified against experimental data in very different operating conditions and applications [74, 41, 75, 76].

GAS–SURFACE INTERACTION MODEL

3.1 ENTRAINMENT PHENOMENA

A considerable amount of research has dealt with the basic phenomena that characterize the flow of a gas over a liquid film. For example, pressure drop in annular two–phase flows, interfacial structure and instability, wetting and entrainment phenomena have been studied. The entrainment, in particular, has been identified as a mass transfer mechanism that occurs through a diffuse injection of droplets from a liquid layer into a gas stream flowing over the free surface. The majority of the research activities on entrainment phenomena has been focused on fundamentals investigations. Anyhow, some studies have been also specifically oriented toward rocket applications, such as liquid–film cooling problems. In these cases the results evidenced that the entrainment contribution to the whole mass transfer is typically several times more important than that due to evaporation [77].

Under the shear stresses exerted by the gas stream the liquid layer could develop interfacial instabilities. Such hydrodynamic instabilities are however just a necessary condition for the entrainment to occur. In fact, infinitesimal disturbances must grow to conform into non–harmonic waveform of finite amplitude to ensure that the phenomenon is manifested [15]. One plausible mechanism is the formation of roll–waves, as it has been confirmed through flow visualizations [52]. In particular, sheets and ligands are torn apart from the tips of such non–linear waves, before breaking into droplets as the viscous forces become less important than the shear actions of the local gas flow. At last, the droplets are atomized into smaller and smaller sizes which evaporate and move within the main gaseous stream [78].

The entrainment is obviously of great interest for paraffin–based hybrid rockets, since it has been identified as the driving mechanism for the relevant regression rate increase. In particular, the melt layer formed by liquefying fuels has been found capable to brake into droplet that burn into the gaseous stream, hence in-

creasing the regression rate. Notice that only if droplets are sufficiently atomized they can completely participate to the combustion process before reaching the nozzle exit, thus contributing to increase the engine thrust [78].

The presence of entrainment phenomena makes CFD models already developed for conventional fuels extremely complex to be extended to the case of liquefying fuels. The additional complexity comes out not only from the number of additional physical phenomena but especially from their mutual interactions, which need to account for multiple phases, with multiple relevant space- and time-scales within a single finite-volume framework [78]. In the past, several CFD models accounting for the interaction between high-speed gaseous flows and low-speed liquid droplets have been developed. However, to describe the complete transition from unstable free surfaces to dispersed liquid droplets appears still a challenge, well beyond actual commercial CFD solver capabilities, as well as far from being handled by RANS codes, as those typically used for design purposes. This restriction has substantially contrasted the development of CFD models for liquefying fuels, limiting the description of entrainment phenomena only to analytical or low-order models, able to treat such a transport phenomena in a very simplified manner [78].

In the present work, a GSI approach to treat entrainment phenomena within a RANS framework for hybrid rocket simulations is presented. Advantage is taken by typical supercritical pressure conditions of paraffin-wax when injected into the grain port.

3.2 GAS–SURFACE INTERACTION BOUNDARY CONDITIONS

The numerical study of the flow field in HRE thrust chambers requires the ability to adequately describe the interaction between the hot gas and the solid surface through suitable GSI modeling. This model requires to solve mass and energy balances at the interface between the gas and the solid phases, which, together with gas-phase combustion and surface chemical models, yield a coupled gas-surface solution. The surface mass and energy balances are connected with the CFD solver because of the presence of gradients which involve the knowledge of variables both at interface and inside the flow field. The way these gradients are expressed

is highly dependent on the numerical scheme adopted for the solver, thus, for the regression rate problem, the surface mass and energy balance have to be considered part of the CFD solver boundary conditions [79]. The GSI model provides the regression rate and mixture composition at wall, which are crucial information for HRE performance predictions and design. Entrainment phenomena, however, impose a further effort to suitably compute these quantities. Here, a specific GSI boundary condition for hybrid rocket applications has been developed and included into the previously described RANS solver for the case of liquefying fuel grains. Such boundary condition has been previously validated for ablating surfaces in re-entry flows [80] and solid-rocket nozzles [81], while it has been already extended to hybrid rocket applications for nozzle erosion [82] and pyrolysing fuel grains regression problems [41].

3.3 SURFACE MASS AND ENERGY BALANCES

The surface mass and energy balances, required by the GSI boundary condition to describe the physics of surface phenomena, are defined for a control volume fixed to the gas-surface interface under the assumption that no material is removed in a condensed phase from the interface. The mass balance is given by:

$$\dot{m}_w = (\rho v)_w = \rho_s \dot{r} \quad (36)$$

expressing the mass flux injected from the surface \dot{m}_w either as the product of the surface gas density, ρ , and normal-to-wall component of velocity, v , or as the product of solid material density, ρ_s , and regression rate, \dot{r} .

The mass balance of each species can be in particular expressed as:

$$\rho D_i \frac{\partial Y_i}{\partial \eta} \Big|_w + \dot{\omega}_i = (\rho v)_w Y_i \quad i = 1, \dots, N \quad (37)$$

where D_i is the species to mixture diffusion coefficient, Y_i is the species mass fraction and $\dot{\omega}_i$ is the species rate of production at the surface.

The energy balance can be finally expressed as:

$$k \frac{\partial T}{\partial \eta} \Big|_w + \dot{q}_{w,\text{rad}} + \sum_{i=1}^N h_i \rho D_i \frac{\partial Y_i}{\partial \eta} \Big|_w + \dot{m}_w h_s = (\rho v)_w h_w + \dot{q}_{\text{cond}} \quad (38)$$

where k is the gas thermal conductivity, T is the gas temperature and h_i , h_s and h_w are the i -th species, solid material and wall enthalpies, respectively. The wall enthalpy, in particular, is the enthalpy of the gaseous mixture at the wall, i.e. the weighted sum at the interface of the i -th species enthalpies, with the relevant mass fractions as weights.

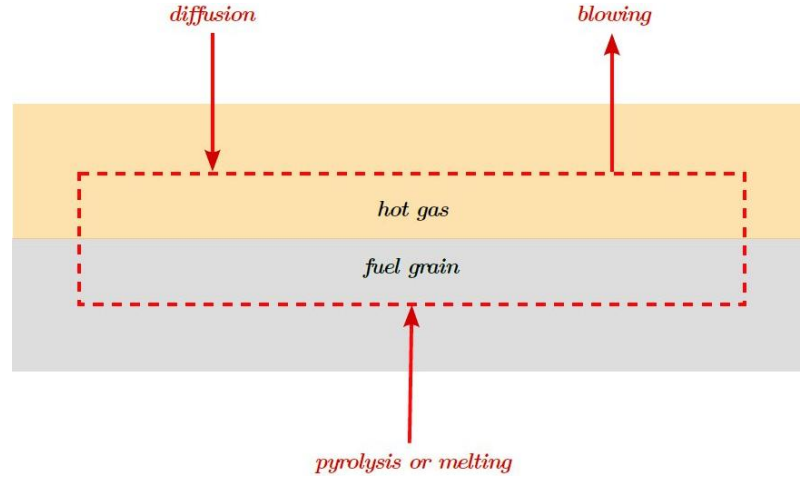


Figure 5: Contributions to the surface mass balance.

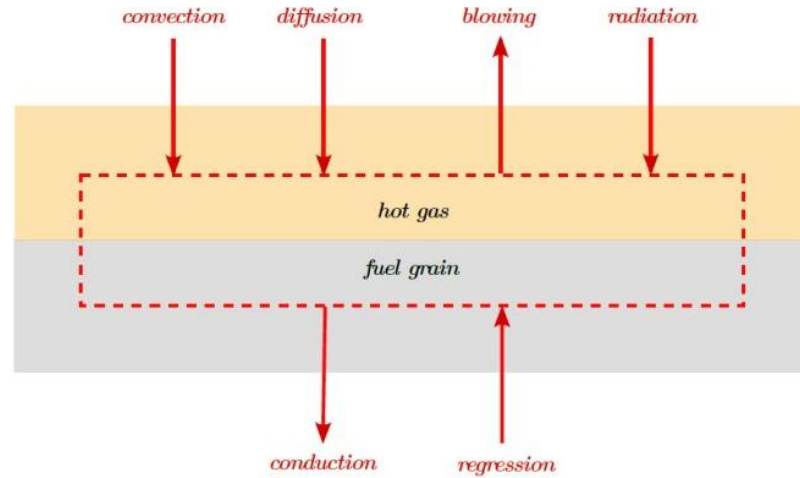


Figure 6: Contributions to the surface energy balance.

By substituting Eq. (36) into Eqs. (37,38) more appealing forms come out.

The surface mass balance (SMB) of species gets the form:

$$\rho D_i \frac{\partial Y_i}{\partial \eta} \Big|_w + \dot{\omega}_i = \dot{m}_w Y_i \quad i = 1, \dots, N \quad (39)$$

which, as shown in Fig. 5, expresses, for each species $i = 1, \dots, N$, the balance between the mass entering the control volume due to diffusion and surface chemical process and the mass leaving the volume by blowing.

The surface energy balance (SEB) gets the form:

$$k \frac{\partial T}{\partial \eta} \Big|_w + \dot{q}_{w,\text{rad}} + \sum_{i=1}^N h_i \rho D_i \frac{\partial Y_i}{\partial \eta} \Big|_w + \dot{m}_w h_s = \dot{m}_w h_w + \dot{q}_{\text{cond}} \quad (40)$$

which, as shown in Figure 6, expresses the balance between the energy entering the control volume because of convection, radiation, diffusion and grain regression and the energy leaving the volume because of blowing and conduction into the solid material.

By substituting Eq. (37) into Eq. (38), the SEB can be re-casted as:

$$k \frac{\partial T}{\partial \eta} \Big|_w + \dot{q}_{w,\text{rad}} = \dot{m}_w \left(\sum_{i=1}^N \frac{\dot{\omega}_i}{\dot{m}_w} h_i - h_s \right) + \dot{q}_{\text{cond}} \quad (41)$$

in order to emphasize that the balance is established between the heat transferred to the grain via convection and radiation and the heat absorbed because of chemical reactions at the surface and thermal conduction into the solid material. The first term at the right hand side, in fact, represents a heat associated to the surface chemical process:

$$\dot{q}_{\text{chem}} = \dot{m}_w \left(\sum_{i=1}^N \frac{\dot{\omega}_i}{\dot{m}_w} h_i - h_s \right) = \dot{m}_w \Delta h_{\text{chem}} \quad (42)$$

which, in turn, is expressed by the product between the injected mass flux and the enthalpy change relevant to the process under examination, responsible of the fuel grain phase change.

The conductive heat flux in the SEB is an input for the CFD simulation, which has to be provided by a coupled numerical computational solid mechanics (CSM) solution. However, when a coupling with a material response code is not available, further hypotheses have to be made in order to compute the conduction contribution. Firstly, it is assumed that heat conduction is dominant in the direction normal to the grain surface. Although axial temperature gradients exist along the grain wall, they are generally small if compared with the normal heat conduction and represent a second-order effect. As a consequence, in a moving local coordi-

nate system tied to the receding surface, the general one–dimensional in–depth energy balance gets the form:

$$\frac{\partial T_s}{\partial t} = \alpha_s \frac{\partial^2 T_s}{\partial \eta^2} - \dot{r} \frac{\partial T_s}{\partial \eta} \quad (43)$$

where the different terms represent the temporal variation of the grain sensible energy, the net conduction inside the material and the convected energy due to the coordinate motion. In particular, α_s and T_s are the grain thermal diffusivity and local temperature, respectively. Secondly, a steady–state regression process is assumed. This appears as a good approximation when the thermal lag in the solid material is sufficiently small, as actually occurs for hybrid rocket conditions, because of the moderately high regression rate and the low thermal conductivity of the fuel grain. By integrating the stationary form of Eq. (43) between the gas–surface interface and a point sufficiently far from the wall, so that an adiabatic condition can be assumed for the in–depth fuel, the conduction term can be expressed by the following closed form [83]:

$$\dot{q}_{\text{cond}} = \dot{q}_{\text{cond}}^{\text{ss}} = \dot{m}_w c_s (T_w - T_{s,d}) \quad (44)$$

where the superscript *ss* indicates a steady–state value according to the introduced approximation. In particular, c_s and $T_{s,d}$ are the specific heat and the in–depth temperature of the solid material, respectively.

The radiative heat flux in the SEB is also considered as an input for the CFD simulation, which has to be provided by a coupled numerical radiative solution. Closed form solutions are not available except for very simplified conditions, leading to very uncertain results. A suitable code for detailed radiative heat transfer predictions, described in detail in Chapter 4, has been developed to overcome this point.

3.4 FORMULATION FOR HYBRID ROCKET FUEL GRAINS

In order to determine both regression rate and mixture composition at wall, a model able to relate wall temperature and injected fuel mass flux is needed to solve the system of PDEs constituted by the SMB and SEB. The formulation is separately presented for non–liquefying and liquefying fuel grains, because they

are characterized by different surface chemical processes, pyrolysis and melting, respectively. The non-liquefying case is considered only for preliminary results, with a validation purpose. The liquefying case, on the other hand, is actually used in the numerical setup built up through the present work.

3.4.1 Non-liquefying fuels

Pyrolysis models to solve the GSI balance equations for non-liquefying fuels often rely on semi-empirical relations [31]. In such models the rate of pyrolysis, i.e. the unknown injected fuel mass flux, is typically expressed as a function of the unknown wall temperature through a single Arrhenius-type equation:

$$\dot{m}_w = A \exp\left(-\frac{E_a}{RT_w}\right) \quad (45)$$

with pre-exponential factor and activation energy available from literature.

Substituting Eqs. (44,45) into Eq. (41) the SEB gets the form:

$$k \frac{\partial T}{\partial \eta} \Big|_w + \dot{q}_{w,\text{rad}} - A \exp\left(-\frac{E_a}{RT_w}\right) [\Delta h_{\text{pyr}} + c_s(T_w - T_{s,d})] = 0 \quad (46)$$

Equation (46) allows to iteratively calculate the wall temperature via Newton-Raphson method. Then, once the wall temperature is known, Eq. (45) allows to evaluate the injected fuel mass flux. Also regression rate and mixture composition at wall are therefore determined by using Eq. (36) and (39), respectively. In particular, if a single pyrolysis product is considered, hence only one species is injected from the interface, in Eq. (39) the chemical source term $\dot{\omega}_i$ is equal to the injected fuel mass flux for the pyrolysis product and equal to zero for all other species. It is worth to note that, even if only one species is injected from the interface, the gas mixture at the pyrolysing wall is not entirely composed by that species, as the others, both oxidizer and combustion products, can reach the surface due to diffusion.

3.4.2 Liquefying fuels

In the case of liquefying fuels the model is further complicated by the entrainment. Such a mechanism, in fact, imposes that the dynamics of the liquid phase enter-

ing the computational domain in the form of droplets is in principle appropriately modeled. As previously observed, such a demanding task has probably discouraged the development of GSI boundary conditions for liquefying fuels and, in turn, that of predictive CFD models for the internal ballistics of paraffin-based hybrid rocket engines. If one notes that for typical hybrid rocket conditions the paraffin-wax is in the supercritical pressure regime, however, different possible modeling solutions arise.

At supercritical pressures no surface tension can be defined and no boundary for droplets exists [84, 85]. In such conditions it is reasonable to assume that the turbulent diffusion and convection of the supercritical species occurs similarly to that of the other species constituting the mixture and, as a consequence, that the entrainment is part of the turbulent mixing process. A classical single-phase RANS approach can therefore be applied, while standard surface mass and energy balance equations, for the GSI boundary condition, still appear to be valid. The only difference to be accounted for is that the wall mass flux is injected through a melting, instead of a pyrolysis process. Accordingly, two additional modeling tasks should be addressed. First, how to model the melted fuel injected from the wall interface, that is a supercritical fluid. Second, how to take into account the way the melted supercritical fuel is transformed into simpler gaseous species actually acting as fuel in the combustion process. In the present work, a simplified dense fluid approach and a thermal cracking process are used for the purpose. Both aspects are presented in details in Chapter 5 together with a basic introduction to supercritical fluids. Here, in Fig. 7, the entrainment process schematic for both subcritical and supercritical pressure conditions is presented. In particular, diffusion, convection, and cracking processes of the supercritical fluid layer are compared to those of liquid droplet formation, diffusion, convection, evaporation and cracking, as it occurs in the subcritical pressure regime. In Fig. 8 an entrainment model schematic for supercritical pressure conditions is also presented by showing the basic physical processes.

The melting model to be introduced appears quite simple since for liquefying fuels the wall temperature is known *a priori* to be equal to the melting value:

$$T_w = T_{\text{melt}} \quad (47)$$

Substituting Eqs. (44,47) into Eq. (41) the SEB gets the form:

$$k \frac{\partial T}{\partial \eta} \Big|_w + \dot{q}_{w,rad} - \dot{m}_w [\Delta h_{melt} + c_s(T_{melt} - T_{s,d})] = 0 \tag{48}$$

Equation (48) allows to directly evaluate the injected fuel mass flux, so that regression rate and mixture composition at wall are determined by using Eq. (36) and (39), respectively. Similarly to the non-liquefying case, in Eq. (39) the chemical source term $\dot{\omega}_i$ is equal to the injected fuel mass flux for the melted fuel and equal to zero for all other species. Also in this case, it is important to note that the gas mixture at the melting wall is not entirely composed of the melted fuel as the other gaseous species, both oxidizer, thermal cracking and combustion products, can reach the surface due to diffusion. Finally, notice that the heat required to melt a unit mass of a liquefying fuel is significantly lower than that required to pyrolyze a unit mass of a conventional grain by roughly an order of magnitude.

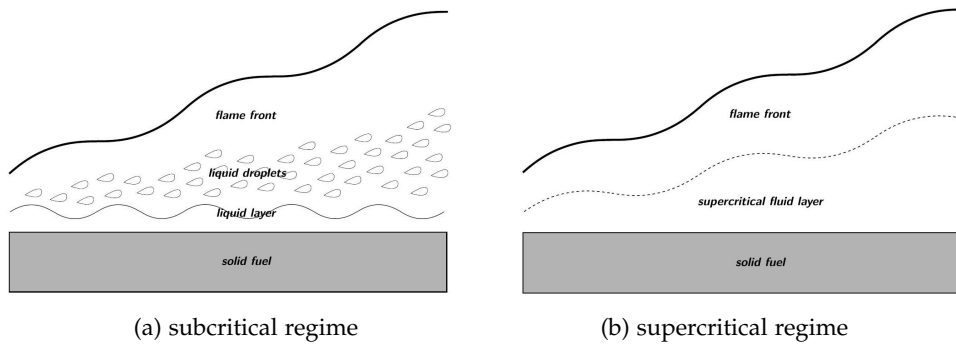


Figure 7: Entrainment process schematic.

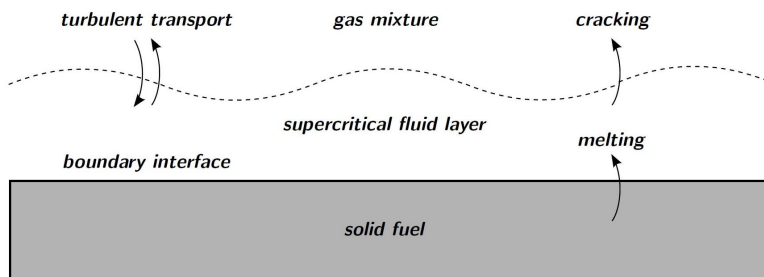


Figure 8: Supercritical entrainment model schematic.

RADIATIVE HEAT TRANSFER MODEL

4.1 FUNDAMENTALS OF THERMAL RADIATION

Radiative energy consists of energy that matter emits or absorbs by lowering or rising molecules energy levels. It can be described by both electromagnetic theory, as consisting of electromagnetic waves, and quantum mechanics, as consisting of massless particles called photons. Neither point of view is able to describe all radiative phenomena that have been observed. It is therefore customary to use both concepts interchangeably. Electromagnetic waves or photons propagate through media at the speed of light c , which can be described either as the ratio between the speed of light in vacuum c_0 and the refractive index of the crossed medium n , or as the product between the wavelength λ and the frequency ν of the wave under consideration:

$$c = \frac{c_0}{n} = \lambda\nu \quad , \quad c_0 = 2.998 \times 10^8 \text{ m/s} \quad (49)$$

In addition, each electromagnetic wave or photon carries an amount of energy ϵ proportional to the frequency ν through the Planck's constant h :

$$\epsilon = h\nu \quad , \quad h = 6.626 \times 10^{-34} \text{ J} \cdot \text{s} \quad (50)$$

Since electromagnetic waves of vastly different frequencies carry vastly different amounts of energy, their behavior is often quite different. Depending on such behavior, electromagnetic waves have been grouped into a number of different categories in the whole electromagnetic spectrum. Among them, thermal radiation may be defined to be constituted by those electromagnetic waves which are emitted by matter due solely by its temperature [86]. The thermal radiation band is conventionally defined as a relatively small fraction of the complete electromagnetic spectrum, positioned between $0.1 \mu\text{m}$ and $1000 \mu\text{m}$, which includes part of the ultraviolet and all of the visible and infrared bands. In particular, when a body

is at ambient temperature most of the energy is radiated in the infrared band. This band is generally subdivided into four smaller bands which are the near infrared (0.1–3 μm), the middle infrared (3–6 μm), the far infrared (6–15 μm) and the extreme infrared (15–1000 μm). However, it should be noted that not only the boundaries but also the involved semantics might change according to the particular context [86, 1].

The exchange of thermal radiation represents a mode of heat transfer as well as conduction and convection. Radiative heat transfer, however, shows significant differences with respect to such other modes, characterized by the need of a medium to propagate, the linear proportionality to temperature differences and the short-range behavior. Since radiative heat is transferred by electromagnetic waves it may propagate in vacuum and travel long distances without interacting with any medium. Radiative heat transfer also generally exhibits a direct proportionality to differences in temperature to the fourth power. As a consequence, the heat exchange by thermal radiation appears to be crucial in vacuum and more and more important, until becoming dominant, with rising temperature levels. Thermal radiation is generally a long-range phenomenon since a photon mean free path, defined as the average distance a photon travels before interacting with a molecule, may be as short as 10^{-10} m, as in the case of absorption in a metal, but also as long as 10^{10} m, as in the case of Sun rays hitting the Earth, or more. For such a reason in presence of thermal radiation the conservation of energy can not be applied on an infinitesimal volume but must be written in an integral form over the entire volume under consideration. Thermal radiation also includes aspects related to direction and spectral dependences. The analysis is therefore further complicated by the presence of three additional independent variables, with respect to the ones needed to describe space and time, which are essentially two angular coordinates for directivity, and wavelength to account for spectral dependence. In addition, radiative properties of different media are usually difficult to be measured and often display an erratic behavior [86].

Thermal radiation interacts with matter. In fact, as shown in Figure 9, the thermal radiation impinging on a layer of finite thickness s can be in part reflected away and in part can penetrate into the layer. In particular, a fraction of the penetrated thermal radiation can be absorbed inside the layer, while the rest can be

transmitted through it. Based on this observation the impinging thermal radiation, often called irradiation, can be expressed as a summation of the reflected, absorbed and transmitted contributions as follows:

$$P_i = P_\rho + P_\alpha + P_\tau \quad (51)$$

and, by dividing both members by the impinging thermal radiation, a useful normalized expression can be obtained:

$$\rho + \alpha + \tau = 1 \quad (52)$$

Here ρ , α and τ are respectively called reflectance, absorptance and transmittance, each assuming values between 0 and 1. When $\rho = 0$ there is no reflected part of thermal radiation, so the medium is called *non-reflective*. Similarly, if $\alpha = 0$ the medium gets the name of *transparent*, because no radiation is absorbed, while if $\tau = 0$ it gets the name of *opaque*, since no radiation is transmitted. All the introduced coefficients, which obviously depend by the temperature and the nature of the medium under consideration, are generally also functions of direction and wavelength. When referred to a specific direction, the coefficients will get the subscript \hat{s} and the appellation of *directional*, in contrast with that of *hemispherical*, for the relevant integral quantities over the solid angle. When referred to a specific wavelength, on the other hand, they will get the subscript λ and the appellation of *spectral*, in contrast with that of *total*, for the relevant integral quantities over the spectrum [1]. Unless specifically expressed, the hemispherical and total appellation will be omitted.

Generally, as thermal radiation penetrates through a layer, it gradually becomes attenuated by absorption, undergoing an exponential decay. According to this behavior, once defined the absorption coefficient of the medium under examination κ , the transmitted radiation can be expressed as a function of the irradiation and the layer thickness as follows:

$$P_\tau = P_i \exp(-\kappa s) \quad (53)$$

while a useful expression for the transmittance can be again obtained by normalizing both members with respect to the impinging thermal radiation:

$$\tau = \exp(-\kappa s) \quad (54)$$

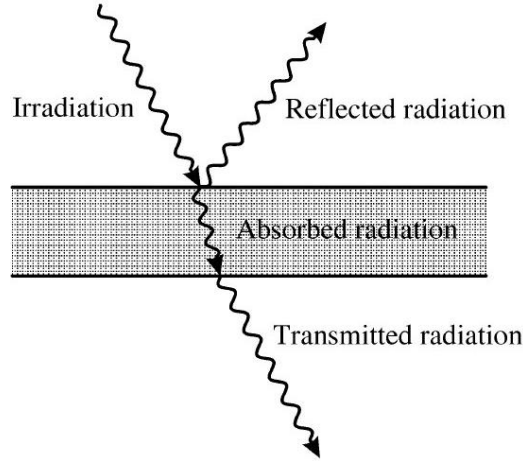


Figure 9: Irradiation contributions through a layer, from [1].

It is worth to note that among the introduced quantities the spectral absorptance $\alpha_\lambda(T, \lambda)$ assumes a particular meaning, since it represents the distribution of the absorbed radiative contents over wavelengths, the so called absorption spectrum. Obviously, the absorption spectrum depends, besides temperature and wavelength, also by the nature of the matter under consideration. For example, in the case of condensed matter the absorption spectrum appears almost continuous, while for gaseous matter it shows a very discontinuous behavior.

Matter continuously emits thermal radiation of different wavelengths, in all directions at a rate depending on the local temperature. The amount of thermal radiative energy emitted per unit time per unit surface area is called total emissive power E , while the emissive power per unit wavelength defines the spectral emissive power E_λ . The total and spectral values of emissive power are related by:

$$E(T) = \int_0^\infty E_\lambda(T, \lambda) d\lambda \quad (55)$$

While emissive power seems to be the natural choice to describe the radiative heat flux leaving a surface, it appears inadequate to describe the directional dependence of the radiative field. This is particularly true inside media, where photons may not have been originated from a surface. Therefore, the total radiative intensity I , defined as the thermal radiative energy emitted per unit solid angle per unit time per unit area normal to the ray under scrutiny, is usually introduced. Similarly to

emissive power, a spectral value of radiative intensity I_λ is defined, and related to the relevant total quantity by:

$$I(T, \hat{\mathbf{s}}) = \int_0^\infty I_\lambda(T, \lambda, \hat{\mathbf{s}}) d\lambda \quad (56)$$

Notice that subscript $\hat{\mathbf{s}}$ is omitted for the radiative intensity because it is always intrinsically referred to a specific direction under scrutiny. The radiative intensity can be also put in connection with the emissive power at a surface by integrating over the hemispherical solid angle:

$$E(T) = \int_{2\pi} I(T, \hat{\mathbf{s}}) \hat{\mathbf{n}} \cdot \hat{\mathbf{s}} d\Omega \quad (57)$$

with $\hat{\mathbf{n}}$ the unit vector normal to the surface, $\hat{\mathbf{s}}$ the unit vector which identifies the generic direction of a ray and Ω the solid angle. If one expresses each line-of-sight $\hat{\mathbf{s}}$ that can be spread out within Ω through an azimuth ψ and an elevation angle θ , by making explicit the scalar product and the definition of solid angle, the relationship between emissive power and radiative intensity can be written as follows:

$$E(T) = \int_0^{2\pi} \int_0^{\frac{\pi}{2}} I(T, \hat{\mathbf{s}}) \sin \theta \cos \theta d\theta d\psi \quad (58)$$

Equations (57,58) are, of course, also valid on spectral basis [86].

The spectral emissive power $E_\lambda(T, \lambda)$, assumes the meaning of emission spectrum. As the absorption counterpart, it also depends by the nature of the matter under examination, exhibiting a continuous or discontinuous behavior for condensed or gaseous media, respectively.

In order to formulate simple general laws for thermal radiation it is useful to introduce the concept of *black body*, an ideal body which is a perfect absorber and emitter of thermal radiation. A black body is thus able to absorb all the received irradiation, regardless of its wavelength and direction, and to emit the maximum possible amount of radiation, for a fixed temperature and wavelength. Even though that of black body is a purely ideal concept, it can be fairly well approximated by a lampblack isothermal cavity with a very small aperture. In such a system, the thermal radiation entering the cavity from the aperture undergoes several reflections before leaving the cavity once again through the aperture. Upon each reflection, significant part of the incident radiation is absorbed by the surface and, therefore,

the radiation eventually leaving the cavity through the aperture is degraded to an extremely small value. Also the radiation emitted by the interior surface of the cavity is maximized to ensure the thermal equilibrium condition at steady-state. The spectral emissive power of a black body is a known quantity through the Planck's law of radiation:

$$E_{b\lambda}(T, \lambda) = \frac{C_1}{\lambda^5 (e^{\frac{C_2}{\lambda T}} - 1)} \quad (59)$$

where $C_1 = 3.742 \times 10^{-6} \text{ W/m}^2$ and $C_2 = 1.439 \times 10^{-2} \text{ K}\cdot\text{m}$ are the first and second radiation constant, respectively. As described in Figure 10, the black body emissive power at a given temperature is a continuous function of wavelength, approaching zero for both very small and very large values, and reaching a maximum at some intermediate wavelength. In addition, the black body emissive power increases significantly with temperature, while shifting the maximum towards smaller wavelengths. The wavelength of maximum emission can be found by differentiating Eq. (59) with respect to wavelength. In this way the Wien's displacement law is obtained:

$$\lambda_{\max} = \frac{A}{T} \quad (60)$$

with the constant $A = 2898 \text{ }\mu\text{m}$. Also the black body total emissive power can be derived from Eq. (59), by integrating over wavelengths. In this way the Stefan-Boltzmann law is found:

$$E_b(T) = \sigma T^4 \quad (61)$$

where $\sigma = 5.670 \times 10^{-8} \text{ W}/(\text{m}^2\cdot\text{K})$ is the so called Stefan-Boltzmann constant [1].

Once defined the laws of a black body, the emission of any real body, which obviously emits only a fraction of the black body counterpart at the same temperature, can be expressed by introducing the concept of emissivity, on both spectral and total bases. The spectral emissivity is defined as:

$$\epsilon_\lambda(T, \lambda) = \frac{E_\lambda(T, \lambda)}{E_{b\lambda}(T, \lambda)} \quad (62)$$

And, similarly, the total emissivity:

$$\epsilon(T) = \frac{E(T)}{E_b(T)} \quad (63)$$

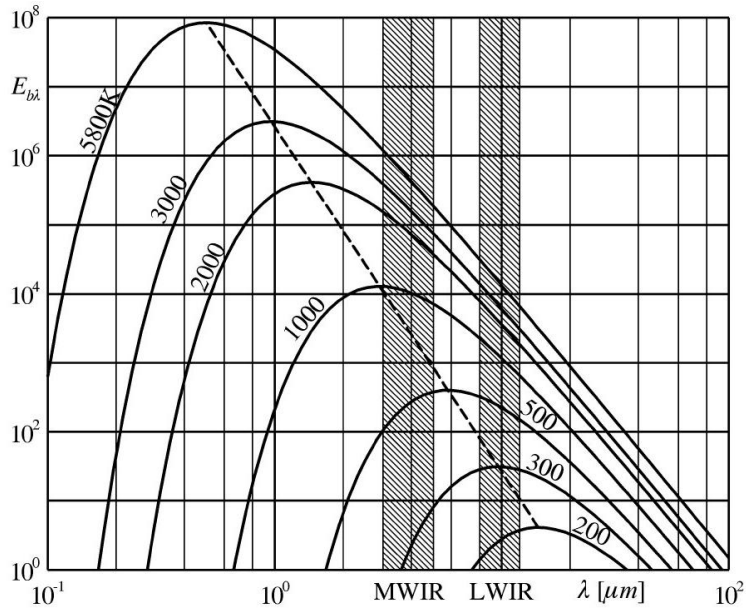


Figure 10: Black body spectral emissive power $[W/m^2\mu m]$ at different temperatures $[K]$, from [1].

Notice that also the emissivity coefficients can be in principle a function of the direction. When the directional dependency does not occur, bodies are called *diffuse* [1].

As previously observed, both the spectral values of emissive power and absorptance are functions of temperature and wavelength, but depend also from the nature of the matter under examination. In spite of this, the ratio between spectral emissive power and spectral absorptance appears independent from the intrinsic features of the body under scrutiny, representing an universal function of only temperature and wavelength. As a consequence, for a given temperature and wavelength, the more a body absorbs the more it will emit and *vice versa*. Such behavior is summarized by the Kirchoff's principle in the following expression:

$$\frac{E_\lambda}{\alpha_\lambda} = \psi(T, \lambda) \quad (64)$$

In particular, by recalling the fact that for a black body the spectral absorptance is equal to unity, it follows that the mentioned universal function equals the black body spectral emissive power:

$$\frac{E_\lambda}{\alpha_\lambda} = E_{b\lambda}(T, \lambda) \quad (65)$$

By recasting Eq. (65), an alternative expression for the spectral absorptance follows:

$$\frac{E_\lambda}{E_{b\lambda}} = \alpha_\lambda \quad (66)$$

So, remembering Eq. (62), it follows that, as a consequence of the Kirchhoff's principle, the spectral emissivity equals the spectral absorptance of a given body:

$$\epsilon_\lambda = \alpha_\lambda \quad (67)$$

Bodies having their absorptance and emissivity independent of wavelength are called *gray*. Accordingly, for diffuse gray bodies Eq. (67), assumes a more general form:

$$\epsilon = \alpha \quad (68)$$

Remembering Eq. (52), in the case of opaque diffuse gray bodies follows that:

$$\epsilon = \alpha = 1 - \rho \quad (69)$$

Such expression appears useful to approximate the behavior of real surfaces, even if no real surface is truly gray over the whole electromagnetic spectrum, since often they have an almost constant spectral emissivity in the infrared band so that the gray hypothesis can be assumed to be satisfied. Obviously, also the hypotheses of opaque and diffuse behavior must be reasonably approximated, as it happens for sufficiently thick and rough surfaces.

For real surfaces is also very useful to apply the electromagnetic theory to find out the directional emissivity as a function of the direction, represented for simplicity only by the elevation angle θ , and the refractive index which is a commonly known parameter. Clearly, the theory is developed with some limiting assumptions so that the emissivity may differ from what is predicted, and it is normally advisable to measure it with *ad hoc* tests. Nevertheless, the theory provides important information on the functional dependence of the directional emissivity on the mentioned parameters. For example, in the case of dielectric real surfaces, according to the theory, the directional emissivity can be calculated by using the relationship:

$$\epsilon_\theta = \frac{2 \sin \theta \sqrt{n^2 - \cos^2 \theta}}{(\sin \theta + \sqrt{n^2 - \cos^2 \theta})^2} \left(1 + \frac{n^2}{(\sin \theta \sqrt{n^2 - \cos^2 \theta} + \cos^2 \theta)^2} \right) \quad (70)$$

For common values of n of dielectric materials, typically smaller than three, the directional emissivity is almost constant for relatively high values of θ but decreases rapidly when the emitted radiation tends towards to being parallel to the surface. With increasing n , the maximum value of the directional emissivity decreases, its drop being more abrupt and, consequently, confined to a smaller range of low values of θ . The hemispherical emissivity can be found by integrating over all directions and the result is particularly interesting. In fact, the hemispherical and normal spectral emissivities are not much different from each other for most practical values of n , within less than 10%. In particular, for the same values of n , normal emissivities higher than 0.75 are expected for dielectric materials [1].

Again from Eq. (52), in the case of non-reflecting diffuse gray bodies it follows that:

$$\epsilon = \alpha = 1 - \tau \quad (71)$$

Such expression appears useful to describe the behavior of the gray approximation of gaseous media. For such media Eq. (54) can be more specifically written explicating pressure in the absorption coefficient, $\kappa = \kappa_p p$ and by identifying the layer thickness with a system characteristic dimension, $s = D$. By using such formula into Eq. (71), the emissivity of gray gaseous media can be described as:

$$\epsilon = \alpha = 1 - \exp(-\kappa_p p D) \quad (72)$$

The pD product, appears to play a crucial role in the absorbing/emitting behavior of the gaseous system. For sufficiently low pD products the absorptance and the emissivity of the medium tend to zero, the gaseous system does not participate to radiative heat exchange, and therefore it gets the name of *non-participating medium*. On the contrary, for sufficiently high pD products, the absorptance and the emissivity of the medium tend to unity, so the gaseous system behaves exactly like a black body. This is the limit case of those in which the product pD assumes finite values, the gaseous system participates to radiative heat exchange, and it is commonly identified as a *participating medium*.

4.2 RADIATIVE PROPERTIES OF MOLECULAR GASES

All gas atoms or molecules carry a certain amount of energy, in the form of molecular kinetic and internal energy. The internal energy consists of several contributions due to translational, rotational, vibrational and electronic states. Thus, a photon passing through a gaseous medium may be absorbed by a molecule raising the level of one of the internal energy states, while, on the other hand, a molecule may spontaneously emit a photon in order to lower one of its internal energy states. Quantum mechanics postulates that the energy levels for atomic or molecular electron orbitals, as well as the energy levels for molecular vibration and rotation, are quantized. Accordingly, since the energy contained in a photon is directly proportional to the frequency, changing the internal energy of a molecular gas can only destroy or generate photons with distinct energy levels and, consequently, only at distinct frequencies. To change the electronic energy level takes a relatively large amount of energy, resulting in absorption–emission lines at short wavelengths, typically in between the ultraviolet and the near infrared. Changing the vibrational energy level of a molecule, requires an intermediate amount of energy, resulting in spectral lines in the near to middle infrared. Finally, rotational energy changes require an even smaller amount of energy, so that rotational lines are found in the middle to far infrared. Usually, vibrational energy changes are accompanied by simultaneous changes in rotational energy levels, so that many rotational lines are clustered around an individual vibrational line. These changes in vibrational energy, accompanied by rotational transitions, lead to closely spaced groups of spectral lines that may partly overlap and lead to the so called vibration–rotation bands [86]. The mentioned energy state changes are known as bound–bound transitions, since they take place between non dissociated atomic or molecular states. Besides such kind of energy state changes other two categories may be defined. In fact, when the transition occurs between a non dissociated and a dissociated state or between two dissociated states, the changes in the energy level, which respectively get the name of bound–free and free–free transitions, exhibit a quite different behavior. Suppose the energy imparted to an atom is in excess of that required for ionization, the liberated electron will carry the excess energy in form of kinetic en-

ergy. As the free electron can absorb any arbitrarily amount of energy, the energy states of the atom above its ionization level are therefore continuous as opposed to the quantized states of the stable atom. An ionized atom will therefore display a continuum within a characteristic spectral band. The energy required for atoms or molecules of gases to be ionized are fairly high and this process is unlikely to be of any importance in rockets utilizing the chemical energy of propellants. For such kind of applications, as well as other systems involving combustion, bound-bound transitions, predominantly due to changes of vibrational-rotational levels, are considered to be of greatest importance [87].

As just described, gaseous media show rather strong variations in their absorption and emission spectra, which appear constituted by a very high number of bands. Moreover, the position of such bands exhibits significant fluctuations depending on the local thermodynamic state. In addition, although quantum mechanics postulates that a molecular gas can only absorb or emit electromagnetic waves of a given frequency, no spectral line can be truly monochromatic. In fact, the shift in phase associated with natural decay, collisions and Doppler effect, leads to band broadening phenomena, and, even though the spectral lines reach their maxima at frequencies predicted by quantum mechanics, the relevant absorption and emission occurs over tiny but finite ranges. Obviously, another element of complexity arises, since also the magnitude of the band broadening strictly depends on local values of temperature and pressure.

In order to solve the problem of the radiative transfer according to a spectral description, the spectrum of the absorption coefficient, as well as all the relevant dependences and broadening phenomena, must be determined. Several approaches can be employed to the purpose, depending on the desired level of accuracy and available computing effort. With decreasing level of complexity, such approaches can be classified into line-by-line, narrow or wide-band calculations. In practice, the very high complexity of line-by-line calculations makes them suitable only as benchmarks for approximate spectral models. On the other hand, wide band calculations can be typically employed adding only small errors to the corresponding computations using a narrow band description.

In radiative heat transfer computations, the interest is usually focused on the determination of total quantities, as for example the radiative wall heat flux. For

such a reason it has often been tried to carry out computations directly involving radiative properties integrated over the whole spectrum, according to a gray gas assumption, instead of considering the described spectral models. Such global model has been the most used in systems involving combustion, where the temperatures involved appear sufficiently limited to allow conditions of vibrational equilibrium. According to the global model approach, the local absorption coefficient of a gas mixture is independent of wavelengths and can be derived according to the expression:

$$\kappa = p \sum_{i=1}^{N_{\text{rad}}} X_i \kappa_{p,i}(T) \quad (73)$$

indicating that the absorption and emission of radiative energy is proportional to the pressure p , i.e. the number of molecules per unit volume, and to the absorption coefficients $\kappa_{p,i}$, weighted with concentrations in terms of molar fraction X_i , of the N_{rad} participating species. In particular, water vapor, carbon dioxide and carbon monoxide are among the combustion products most significant in the process of thermal radiation exchange. Non-negligible contributions, however, can arise also from the presence in the gaseous mixture of nitrous-oxide, ammonia, sulfur-dioxide, methane or nitric-oxide [86, 88]. The absorption coefficients of the participating species, known as Planck-mean absorption coefficients, are averaged over the whole spectrum, hence they depend only on temperature. The temperature dependence of Planck-mean absorption coefficients of water vapor, carbon dioxide and carbon monoxide is given up to 2500 K in Ref. [89] and up to 2800 K in Ref. [90], by fitting the curves reported in Refs. [86, 88]. In Ref. [2] a new updated model for the Planck-mean absorption coefficients of the mentioned species up to 5000 K is presented, see Fig. 11. The averaging process has been carried out over the infrared domain from statistical narrow band data, in turn generated from line-by-line calculations.

4.3 RADIATIVE TRANSFER IN PARTICIPATING MEDIA

Thermal radiation calculations are always performed by making an energy balance within an enclosure bounded by opaque walls. If the enclosure is filled with a non-participating medium we speak of surface radiation transport. On the contrary, if

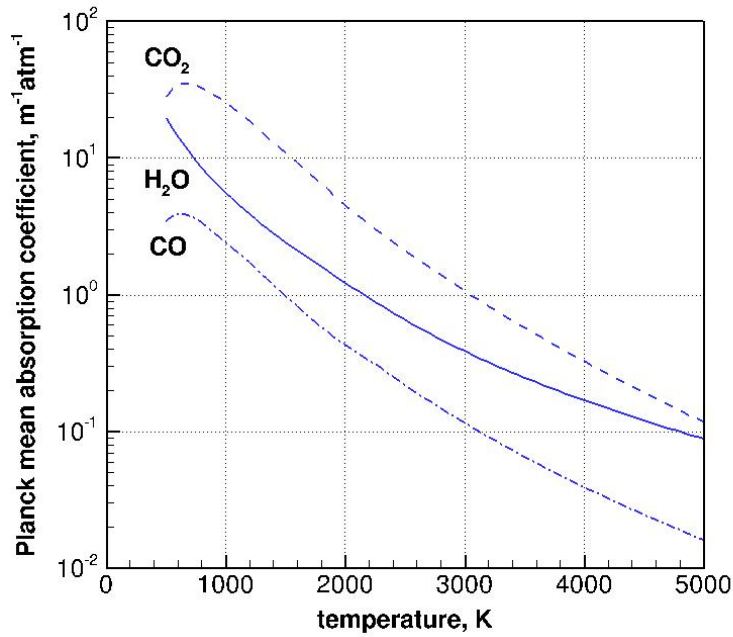


Figure 11: Planck–mean absorption coefficients for water vapor, carbon dioxide and carbon monoxide, after [2].

the enclosure is filled with a participating medium, we refer to radiative transfer in participating media. Of course, radiation in a participating medium is always accompanied by surface radiation transport. The radiative transfer in participating media must be accounted for in many aerospace engineering applications including rocket propulsion, hypersonic shock layers and ablation systems on reentry vehicles [86].

The equation governing the transport of radiative energy in participating media is presented here. Some basic hypotheses are however made to simplify the description. Both the medium and the wall are assumed to behave like gray bodies, so that any equation can be written in terms of total, instead of spectral quantities. In any case, the equations relevant to a spectral model can be easily obtained from those presented here by considering spectral values and integrating over wavelengths in the whole spectrum. Additional hypotheses are those for the medium to be non–scattering and for the wall to be diffuse. Extensions to account for scattering effects or reflections in a non–diffuse manner can be found in Ref. [86].

The objective of thermal radiation analyses is the evaluation of the radiative heat flux at physical boundaries. In particular, the so called radiative wall heat flux can be evaluated as follows by applying the definition of emissive power in Eqs. (57,58) to a point laying on the wall boundary:

$$\dot{q}_{w,\text{rad}} = \int_{2\pi} I_w \hat{\mathbf{n}} \cdot \hat{\mathbf{s}} d\Omega = \int_0^{2\pi} \int_0^{\frac{\pi}{2}} I_w \sin \theta \cos \theta d\theta d\psi \quad (74)$$

Obviously to calculate the radiative wall heat flux, the radiative intensity at wall coming from any generic line-of-sight that can be traced out from the wall point under scrutiny must be determined. This can be done in principle by integrating an energy balance of thermal radiation along the path length relevant to each line-of-sight. The energy balance can be conveniently written in terms of radiative intensity and it has obviously to account for both absorption and emission contributions from the medium. The attenuation of radiative intensity due to absorption is directly proportional to the distance traveled by the radiation as well as to the incident radiative intensity:

$$dI_{\text{ab}} = -\kappa I ds \quad (75)$$

Similarly, the augmentation due to emission is directly proportional to the distance traveled by the radiation and to the local energy content in the medium, which under thermodynamic equilibrium conditions, is represented by the black body radiative intensity:

$$dI_{\text{em}} = \kappa I_b ds = j^e ds \quad (76)$$

In both cases the proportionality coefficient is given by the absorption coefficient κ , while a new quantity $j^e = \kappa I_b$, called emission coefficient, has been defined to briefly describe the emission contribution. Summing up contributions in Eqs. (75,76), and properly recasting, the balance of radiative intensity along a generic line-of-sight, the so called radiative transfer equation (RTE), is obtained:

$$\frac{dI}{ds} = j^e - \kappa I \quad (77)$$

In particular, its formal solution is given by:

$$I_w = I_0 \exp\left(-\int_{s_0}^{s_w} \kappa ds\right) + \int_{s_0}^{s_w} j^e \exp\left(-\int_s^{s_w} \kappa ds'\right) ds \quad (78)$$

where it is assumed that the coordinate along the line-of-sight s originates from a wall point s_0 , representing the origin, and ends up on another wall point s_w , representing the calculation location. The radiative intensity I_w reaching the calculation location from a given line-of-sight is therefore due to the contributions I_0 from the origin of the line-of-sight, and j^e from each point in the medium along the line-of-sight. The exponential terms account for radiation absorption by the medium from the origin, in the first term, and through the medium itself, in the second term.

The RTE is an ODE in terms of radiative intensity. Accordingly, its resolution requires the specification of a boundary condition at a certain location. Generally, it is convenient, as evident from the RTE formal solution, to set the value at the origin of the line-of-sight. In particular, the following expression can be used [91]:

$$\mathcal{I}_0 = \frac{\epsilon_0 \sigma T_0^4 + \rho_0 \dot{q}_{0,\text{rad}}}{\pi} \quad (79)$$

to account for both the radiative intensity emitted and reflected by the wall of emissivity ϵ_0 and reflectance ρ_0 .

4.4 DISCRETE TRANSFER METHOD

Exact analytical solutions for the RTE are usually particularly difficult to obtain, and explicit solutions are generally impossible to express for all situations except the simplest cases. Therefore, research on radiative heat transfer in participating media has generally proceeded to find either analytical solutions of highly idealized configurations or approximate solution methods for more complex realistic scenarios. The majority of exact solutions have been limited to gray isothermal media in one-dimensional mainly plane-parallel geometries, appearing of limited usefulness in heat transfer applications. For what concern approximate solution methods, a survey of the literature over the last years indicated that only a few have found frequent usage, while others have been no longer employed on a regular basis despite their promise. Apparently, some methods seem to be more readily adapted to more difficult situations than other ones [86]. It must be remembered that thermal radiation modeling shows many complex aspects that should be suit-

ably treated including directivity, interactions with complex geometries, spectral dependence, inhomogeneous conditions, coupling to the gas flow, sooting, possibly scattering or non-equilibrium. The most important methods used today in radiative heat transfer analyses include zone method [92, 93], flux method [94, 95], discrete ordinate method [96, 97], spherical harmonic method [98, 99, 100], Monte Carlo method [101] and discrete transfer method (DTM) [102]. With increasing computing power, the first four converge to the solution of the method, i.e. vitiated by the introduced assumptions, whereas the last two converge to the actual solution of the problem. Moreover, the zone method appears uneconomic, particularly because for complex geometries the exchange factors are not available and must be worked out in advance, while the flux method, which is able to offer a very high computational economy, entails a degree of mathematical complexity which inevitably obscures the physics and disenchant the engineering user [102]. Although for sufficiently high discretization the Monte Carlo method yields to the exact solution, it seeks for the solution by injecting packets of photons into the flow field and tracking their path under some stochastic assumptions, which makes the computing slow, the accuracy limited by the inherent imperfections of computer random number generation routines and the coupling to a CFD solver very difficult. The DTM, which combines features and advantages of the zone, flux and Monte Carlo methods, while avoiding their shortcomings, it is accordingly adopted in the present work. It is exact, applicable to complex geometries, fast and it highlights the physics of the problem by avoiding complex mathematics [102].

The DTM foresees the evaluation of the radiative heat flux at a selected calculation point on the wall by solving the RTE along representatively directed beams of radiation emanated from the calculation point under scrutiny within the envisaged enclosure. The equations of the problem are written in finite form by discretizing the domain and hence substituting the integration operation with relevant summations. The hemispherical solid angle seen by the generic calculation point is discretized into different sectors by discretizing the elevation and azimuth angles with which it is represented. In particular, the range of the elevation angle θ_{ij} between 0 and $\pi/2$ is subdivided into I intervals while that of the azimuth angle ψ_{ij} between 0 and 2π into J intervals. In such a way a finite number $I \times J$ of rays ij , each representing a sector of the hemispherical solid angle, is extracted from the

calculation point. The path length of each ray defined along the abscissa s_{ij} is in turn discretized into a number of L_{ij} intervals in order to perform a finite integration of the RTE and hence evaluate the radiative wall heat flux in the location of interest. In particular, the integration over the path length along each ray allows to evaluate the relevant radiative intensity at wall $I_{w,ij}$:

$$I_{w,ij} = I_{0,ij} \exp\left(-\sum_{l=1}^{L_{ij}} \kappa_l \Delta s_l\right) + \sum_{l=1}^{L_{ij}} j_l^e \exp\left(-\sum_{m=l}^{L_{ij}} \kappa_m \Delta s_m\right) \Delta s_l \quad (80)$$

while the integration over the solid angle at each calculation point allows to evaluate the associated radiative wall heat flux $\dot{q}_{w,rad}$:

$$\dot{q}_{w,rad} = \sum_{i=1}^I \sum_{j=1}^J I_{w,ij} \sin \theta_{ij} \cos \theta_{ij} \Delta \theta_{ij} \Delta \psi_{ij} \quad (81)$$

where Eqs. (80,81), are the discretized form of Eqs. (78,74), respectively.

The field and wall local conditions needed by the method can be recovered from the CFD simulation, with which the DTM computation is coupled. In particular, the pressure, temperature and composition fields are required to evaluate the absorption coefficient $\kappa_{l,m}$ of the gaseous mixture at each space step along each line-of-sight according to Eq. (73). At the same time, the wall temperature is required to evaluate the radiative intensity at the origin of the line-of-sight $I_{0,ij}$ by applying the boundary condition in Eq. (79). Since such boundary condition depends on the radiative heat flux reflected by the wall, then on the incoming radiative intensity, an iterative computational procedure is required by the method.

The most complex part of the method, as it implies adopting another grid in addition to the one used to discretize the equations of motion, is tracing the rays and determining their intersection with the geometry at hand. A dedicated algorithm must be therefore developed to this end.

4.5 DEVELOPED RADIATIVE CODE

In the present work, a radiative heat transfer code for axisymmetric gray/diffuse boundaries and inhomogeneous gray/non-scattering media, has been developed, based on the DTM.

The gray assumption is quite accurate for the wall, because of its continuous behavior over the spectrum, while it allows to significantly reduce the computational

time, by means of a global treatment of spectral features, when introduced for the medium. The constraint on computer time almost invariably restricts the choice to gray gas approaches, which assume that the optical properties of the medium are independent of radiation frequency, thereby enabling to describe the phenomenon in terms of a single radiative intensity, rather than a huge number of spectral intensities. The high roughness level expected for the wall surface, is well in agreement with the diffuse wall hypothesis, since reflection from rough surfaces approximates the diffuse reflection regime [103]. The non-scattering nature of soot [86] and the absence of other solid particles suspended in the gas phase, finally, agrees with a non-scattering behavior of the medium. Notice that the effect of soot radiation is not yet accounted for in the present study, but models to consider this contribution are under development [104]. It is also assumed that radiation does not affect the flow field significantly [105], because of the relative small weight of the wall heat transfer, and in particular of the radiative contribution, as compared to the whole thermal power generated within the thrust chamber. This reasonably allows to avoid the calculation of the radiative heat flux at each cell center in the flow field and to neglect its contribution into the energy conservation equation. The radiative heat flux is therefore only evaluated at selected nodes on the wall boundary, and hence a radiative wall heat flux profile is determined.

Looking at the specific application to CFD simulations with GSI capabilities of HRE flow fields, a coupling between DTM and CFD solutions is needed in order to take into account the effect that the radiative wall heat flux has on the fuel regression rate, and in turn the effects that the modified flow field has on the radiative heat transfer toward the grain wall. Such kind of a coupling is realized by implementing an iterative procedure between DTM and CFD solutions until a sufficiently accurate degree of convergence is attained.

4.6 CODE TESTING AND CONVERGENCE ANALYSIS

The previously described radiative heat transfer code has been verified against exact solutions and validated against experimental data. Convergence analyses

with different levels of discretization have been also performed in both cases. A summary of the results obtained are presented in the following.

4.6.1 *Infinitely long square cavity*

The verification test is performed against the exact solution in Ref. [102]. Such solution is given in terms of radiative wall heat flux, made dimensionless with the black body emissive power, as a function of the normalized distance along the edge L of an infinitely long square cavity, constituted of black cold walls, containing a medium of constant absorption coefficient κ . The solution is made available for three different levels of the medium optical thickness $\tau = \kappa L$. The geometry at hand is represented in Fig. 12, where the red segment highlights the generic edge along which the solution is evaluated.

For each of the 21 calculation point used for the verification, a number of rays equal to 1024, traced out by defining 16 and 64 intervals in elevation and azimuth, respectively, together with a spatial integration step of $10^{-4}L$, are adopted.

Figure 13 shows a good agreement between the exact and the present DTM solution for $\tau = 1$, being the error between the average value of the two solutions equal to 0.36%. As shown in Figs. 14,15, a similar result is obtained for $\tau = 0.1$ and $\tau = 10$, with errors of 0.73% and 0.07%, respectively.



Figure 12: Infinitely long square cavity under consideration.

A convergence analysis on the DTM solution, obtained for each envisaged level of the optical thickness, has been performed by considering both a coarser and a finer discretization with respect to the adopted one. In particular, the coarser discretization (256 rays and $2 \times 10^{-4}L$ step) has been realized by halving the number of angular intervals, for both elevation and azimuth, and of the spatial integration step along each ray, while the finer discretization (4096 rays and $0.5 \times 10^{-4}L$ step) has been obtained in the opposite way.

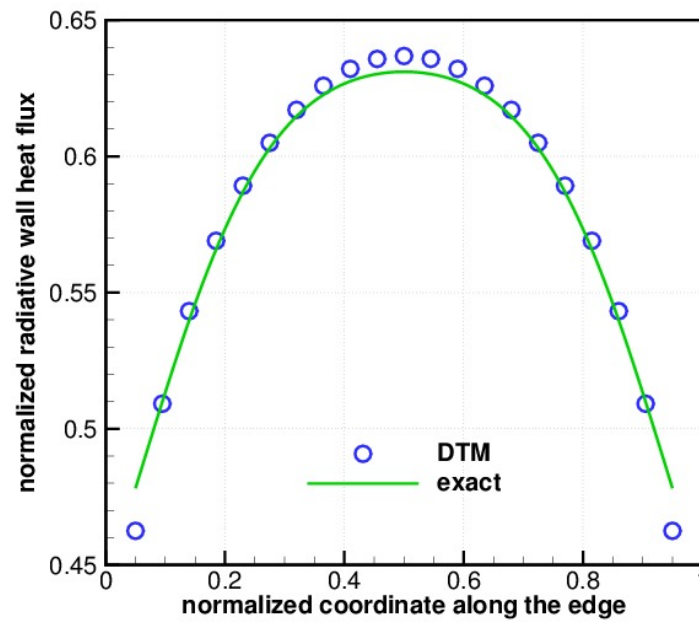


Figure 13: Comparison between exact and present DTM solution for $\tau = 1$.

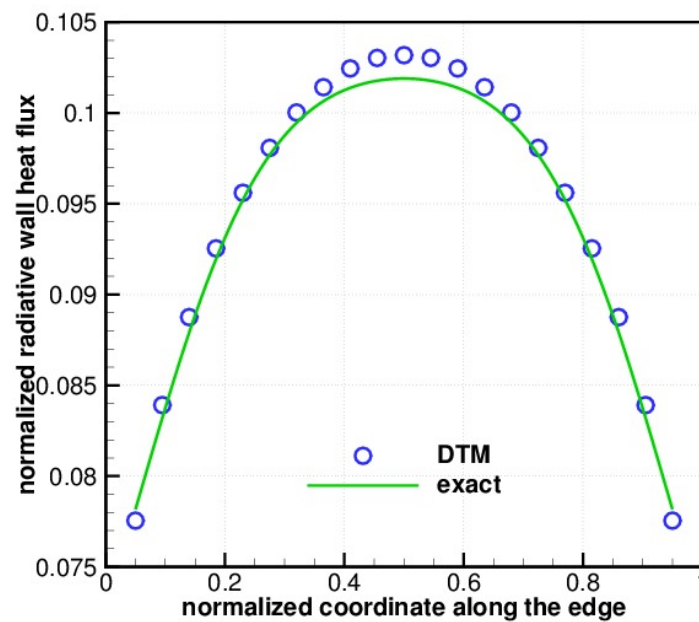


Figure 14: Comparison between exact and present DTM solution for $\tau = 0.1$.

Figure 16, in the case of $\tau = 1$, shows a monotonically converging trend from the coarse to the fine discretization, with the medium one ensuring an error lower than 1%. As reported in Figs. 17,18, the same result is found for $\tau = 0.1$ and $\tau = 10$.

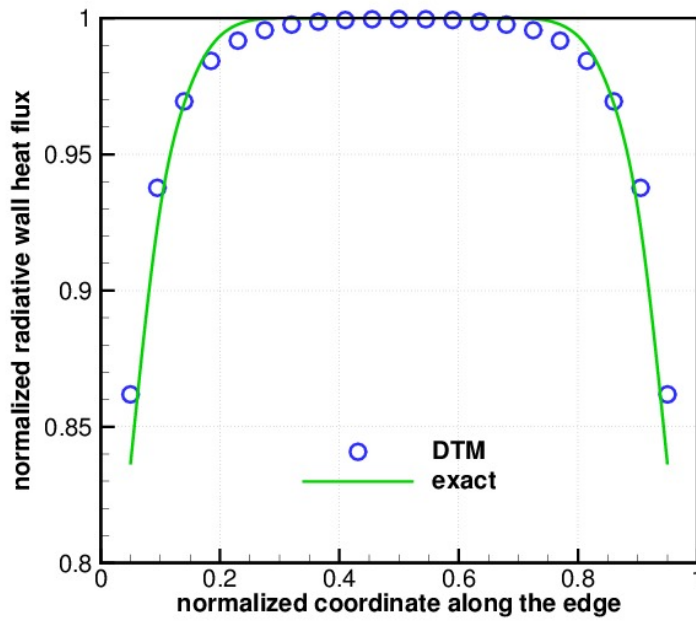


Figure 15: Comparison between exact and present DTM solution for $\tau = 10$.

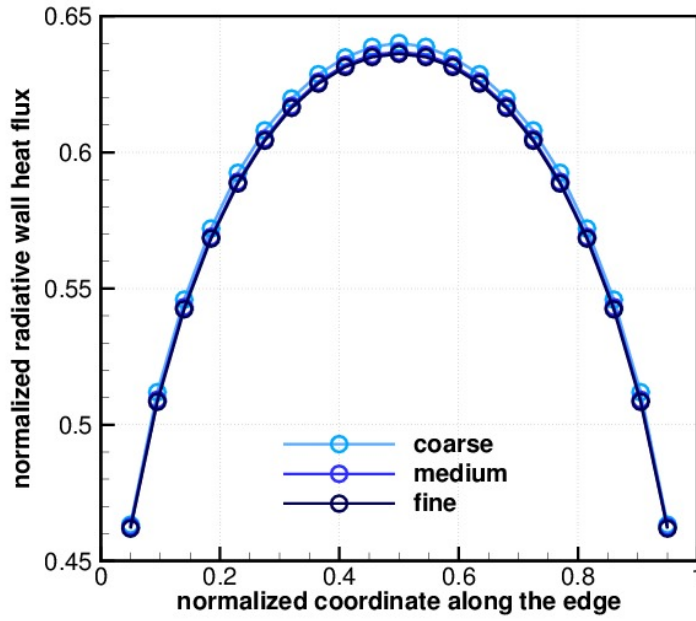


Figure 16: Convergence analysis of present DTM solutions in the case of $\tau = 1$.

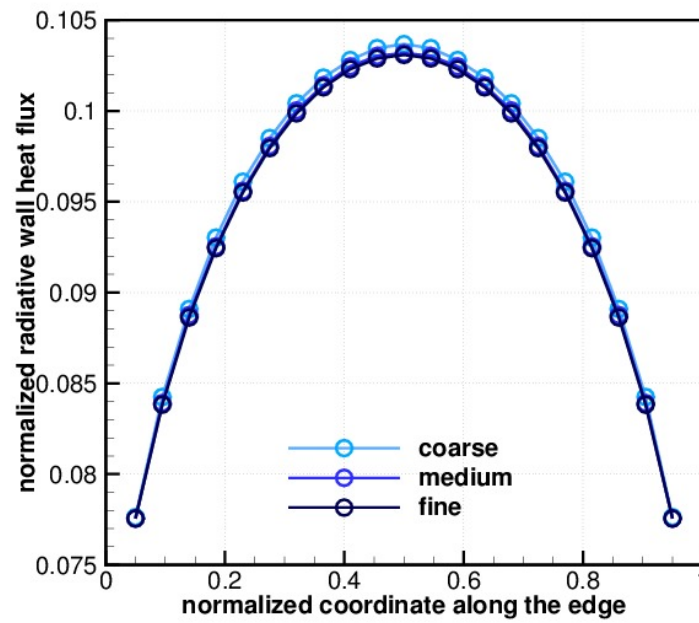


Figure 17: Convergence analysis of present DTM solutions in the case of $\tau = 0.1$.

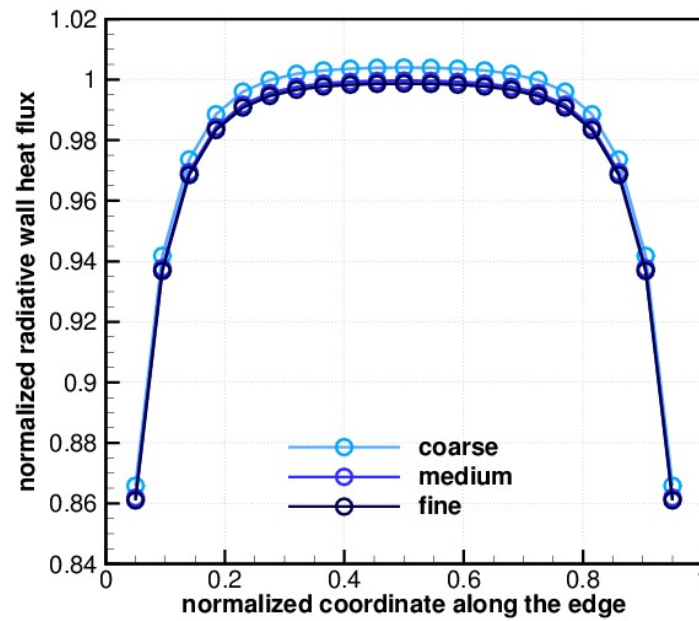


Figure 18: Convergence analysis of present DTM solutions in the case of $\tau = 10$.

4.6.2 Sub-scale liquid rocket engine

The validation test is performed against experimental data on the wall heat flux obtained in a sub-scale liquid rocket thrust chamber working with oxygen/methane

propellants [106, 3]. The experimental data on the wall heat flux, given with an uncertainty of 5%, are obtained by a calorimetric method, based on the coolant temperature increase in each cooling segment [3]. Notice that the mentioned wall heat flux measurements are integral values associated to each segment. In particular, instrumented segments are located in the cylindrical region of the chamber, whereas no measurement is taken in the nozzle region. Test cases in Refs. [106, 3] have been designed to investigate film cooling efficiency. However, attention is focused on a test case performed without film injection, and reported as reference, to emphasize the role of radiative heat flux. The liquid rocket engine under scrutiny is represented in Fig. 19, together with labels of its main components.

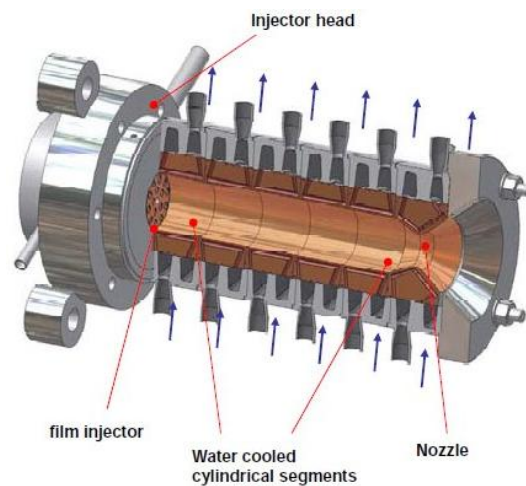


Figure 19: Sub-scale liquid rocket engine under consideration, from [3].

The experimental data are rebuilt by performing CFD and associated DTM simulations of the engine. The convective wall heat flux is evaluated from the CFD solution, while the radiative one is calculated via DTM. Values of temperature, pressure and composition, required to evaluate radiative properties inside the domain, are recovered from the CFD solution. Notice that no iteration between the CFD and DTM solutions is needed in this case because of the enforced isothermal wall boundary condition. The computed total wall heat flux, obtained by summing up the computed convective and radiative contributions, is compared to the wall heat flux measurement already described.

Details of the CFD simulation, here omitted, can be found in Ref. [107].

For what concern the DTM simulation, the selected domain includes the cylindrical chamber and the convergent conical section of the nozzle. Indeed, the throat and the nozzle divergent give a small contribution because of the reduced local temperature and pressure, and shadowing effects, so they are not included. All the boundary surfaces are treated as black walls in order to avoid iteration. At the injection plate and the end section of the conical convergent, a uniform temperature is assigned as the spatial average of computed temperatures over the relevant cross section. At the lateral chamber walls, on the other hand, the wall temperature inferred from the experiments is enforced. Errors deriving from such simplified boundary conditions are proved to be negligible, since walls only give a marginal contribution.

The wall boundary is discretized by means of 50 calculation points, located at the center cell abscissas of the corresponding CFD grid, in the portion of the domain considered for the radiative heat transfer analysis. For each calculation point, 256 rays, obtained by defining 8 and 32 intervals in elevation and azimuth respectively, are drawn, while a spatial integration step of 10^{-3} m is adopted along the rays.

Measured and computed wall heat fluxes are shown in Fig. 20. The estimated experimental error bar and the split between computed convective and radiative heat fluxes are also reported. The experimental wall heat flux increases downstream of the injection plate, attains a peak and then decreases somewhat. The computed wall heat flux decreases along the chamber due to boundary layer thickening, which hinders the convective contribution, while the radiative one is almost constant along the chamber. Notice that, in order to allow a meaningful comparison, computed heat fluxes are averaged over the length of each of the segments over which measurements are taken. A mismatch is observed in the initial part of the chamber, to be ascribed to the simplified inlet boundary condition adopted for the CFD simulation, which disregards the injection geometry details. Nevertheless, in downstream segments, where injection effects have subsided, numerical results can meaningfully be compared to experimental values. This is especially true for segments located 150 mm or more downstream of the injector plate, where the wall heat flux reaches a maximum, including segments S4 and S5. A comparison of the averaged heat flux values, focused on meaningful segments, shows that the radiative contribution to the total heat flux is 13.4% in segment S4 and 13.3% in

segment S5. When adding the radiative contribution to the convective heat flux, this results in slightly overestimating experimental data, 0.4% in segment S4 and 1.6% in segment S5, though still within the presumed error range.

Also in this case a convergence analysis on the DTM solution is performed by using a coarser (64 rays and 2×10^{-3} m step) and a finer (1024 rays and 0.5×10^{-3} m step) discretization. Figure 21 shows again a monotonically converging trend from the coarse to the fine discretization, and errors lower than 1% ensured by the medium discretization.

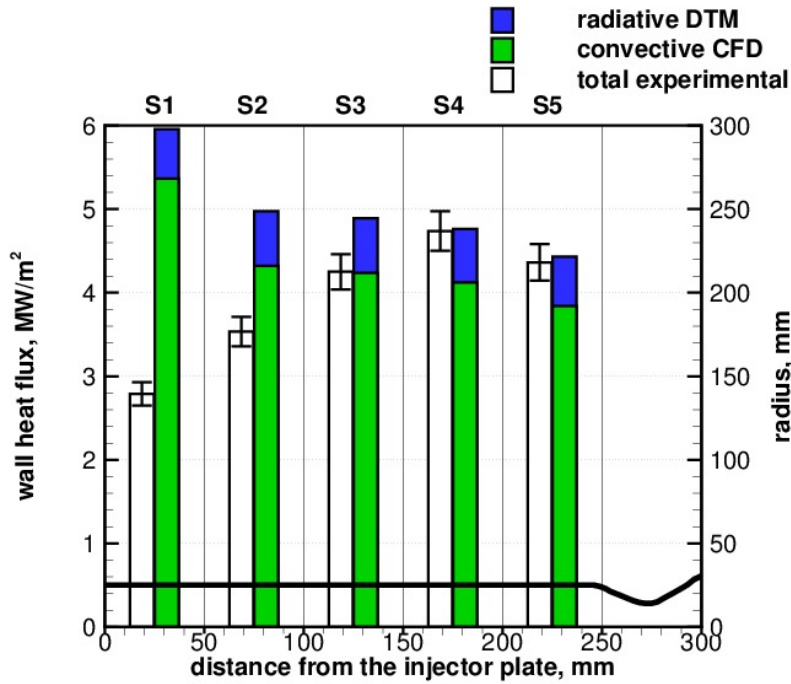


Figure 20: Comparison along different segments of integral wall heat flux measurements and computed convective and radiative contributions.

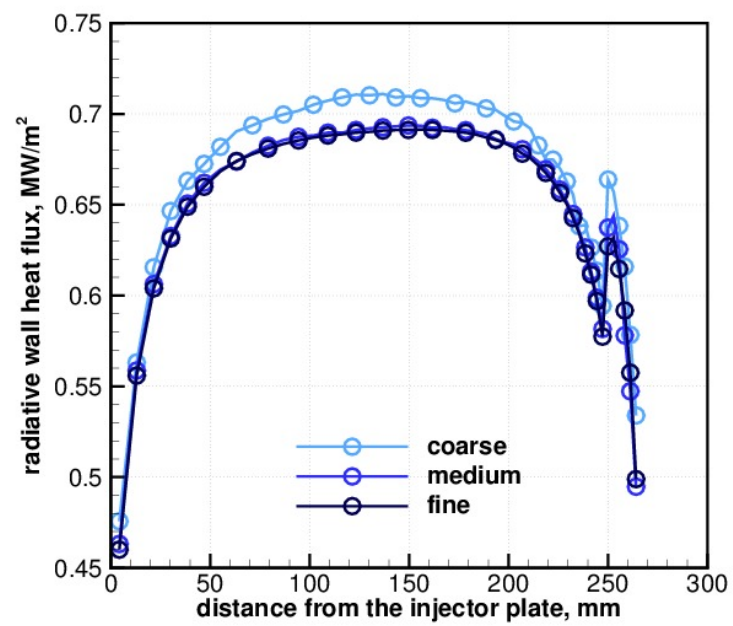


Figure 21: Convergence analysis of present DTM radiative wall heat flux predictions.

THERMOCHEMISTRY MODEL

5.1 BASICS OF SUPERCRITICAL FLUIDS BEHAVIOR

It is well known that when a fluid exceeds the boiling temperature at subcritical pressures it undergoes a phase change from liquid to gas with an associated discontinuous variation of its thermophysical properties. With the pressure approaching the critical value, in particular, the transition becomes dramatic, with the specific heat reaching a maximum which tends to infinity and the dynamic viscosity and thermal conductivity undergoing a significant drop within a very narrow temperature range. In the supercritical pressure regime the fluid exhibits a rather different behavior. It shows a continuous variation of the properties and the phase change does no longer occur, at least in the way it has been previously defined. In these conditions it is common practice to say that the fluid undergoes a pseudo-phase change by crossing the pseudo-critical temperature, the temperature where, for a given pressure, the maximum specific heat is attained [108]. When a supercritical fluid crosses the local pseudo-critical temperature it shows a peak of the constant pressure specific heat, while properties such as viscosity and thermal conductivity decrease [4]. These variations are more gradual than for a subcritical fluid, though they become larger as the pressure gets closer to the critical value [108]. In particular, by exceeding the local pseudo-critical temperature a supercritical fluid moves from a liquid-like to a gas-like state. The liquid-like state is characterized by high density, high viscosity and low thermal compressibility. The gas-like state, on the contrary, exhibits low density, low viscosity and high thermal compressibility. The latter represents the attitude of a fluid to increase its density by an isothermal compression [109]. For example, let us consider methane, whose critical point is defined at about 46 bar and 191 K. The change from a discontinuous to a continuous transition, moving from a subcritical to a supercritical pressure regime, respectively, can be well understood looking at methane density behavior with in-

creasing temperature in Fig. 22. Still considering methane as a representative fluid, the effect of subcritical or supercritical pressures on the constant pressure specific heat behavior with temperature can be observed in Fig. 23. In particular, notice that the thermophysical properties at supercritical pressure well approximate the liquid or gas properties if one consider temperatures sufficiently below or above the local pseudo-critical temperature, respectively. From such peculiar behavior arise the liquid- or gas-like definitions previously introduced.

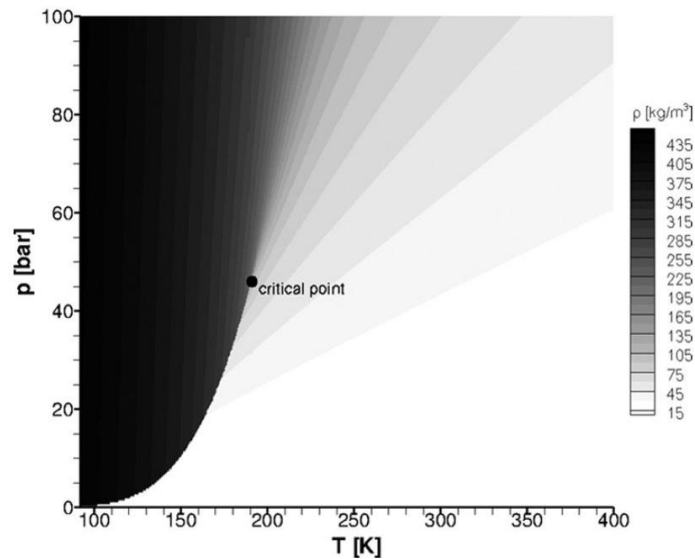


Figure 22: Methane density behavior, from [4].

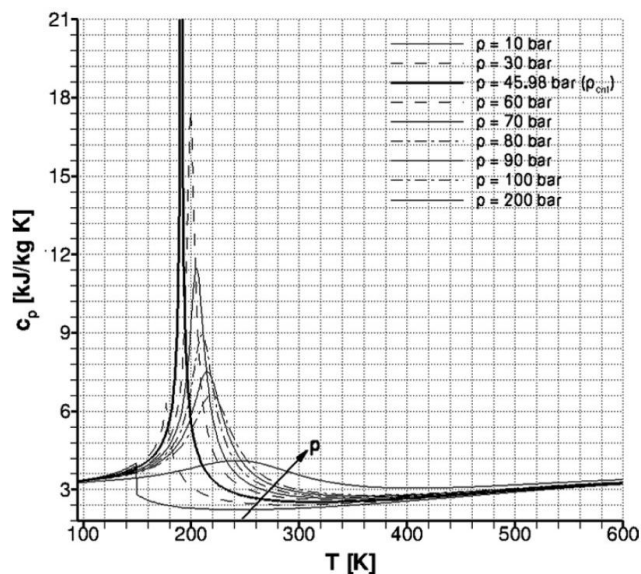


Figure 23: Methane constant pressure specific heat behavior, from [4].

5.2 PARAFFIN-WAX THERMOPHYSICAL PROPERTIES

The melted paraffin-wax injected from the gas-surface interface appears to be in the supercritical pressure regime [57]. In fact, chamber pressures achieved in hybrid rocket conditions are typically far above paraffin-wax critical pressure (see Fig. 24 for carbon numbers in between 25 and 45).

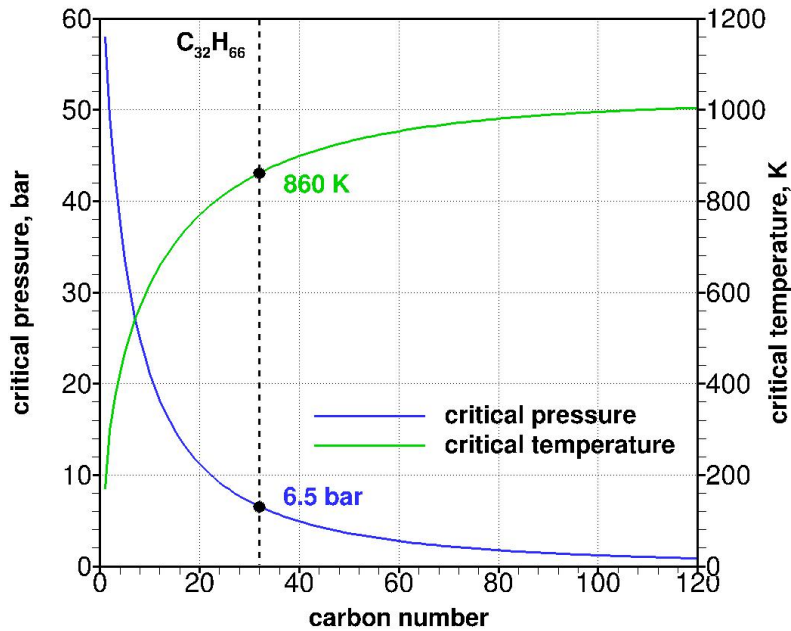


Figure 24: Normal-alkanes critical properties as a function of carbon number.

Modeling the melted paraffin-wax injected into the port can be strongly simplified thanks to supercritical pressure conditions. In fact, no multi-phase modeling is required if no surface tension exists for paraffin-wax droplets. In this context, a single-phase RANS approach with suitable GSI interaction modeling appears viable as described in Chapter 3. At least in principle, a suitable equation of state accounting for real gas properties, like those by Van der Waals, Peng-Robinson or Benedict-Webb-Rubin, should be introduced to treat the supercritical paraffin-wax. However, a simplified model relying on the liquid-like behavior of paraffin-wax below the critical temperature (see again Fig. 24 for carbon numbers from 25 to 45) is used. In such a model paraffin-wax thermophysical properties are assumed to be those at liquid state, although they are used in a thermally perfect gas

model. This is a first approximation to treat in a simple way the melted paraffin wax as a dense species, a fairly good assumption below the critical temperature. By assuming $C_{32}H_{66}$ to be the reference paraffin-wax, the relevant liquid state thermophysical properties are derived with the asymptotic behavior correlations (ABC) method presented in Refs. [6, 7, 8] for a carbon number equal to 32. The same method is used to derive the curves drawn in Fig. 24, where also the values of critical pressure and temperature for $C_{32}H_{66}$ are highlighted.

The temperature behavior of thermodynamic properties obtained with the ABC method is brought back to the description in Eqs. (15,16,17) by using the coefficients reported in Table 1. In Fig. 25 the constant pressure specific heat, as a representative thermodynamic property, is shown as a function of temperature.

Table 1: Liquid-like paraffin-wax thermodynamic properties coefficients [6, 7, 8].

Coefficient	Value
a_1	0.0000000000
a_2	0.0000000000
a_3	4.9784521510
a_4	0.6354811390
a_5	-0.001018012
a_6	0.0000000615
a_7	0.0000000000
b_1	-115293.7171
b_2	-579.1619128

The temperature behavior of transport properties obtained with the ABC method is introduced by proper functions for viscosity and thermal conductivity, respectively, as follows:

$$\mu_{C_{32}H_{66}} = 0.001 \exp \left(A_\mu + \frac{B_\mu}{T} + C_\mu \ln T + D_\mu T^2 + \frac{E_\mu}{T^2} \right) \quad (82)$$

$$k_{C_{32}H_{66}} = A_k + B_k T \quad (83)$$

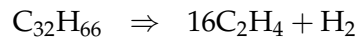
where the coefficients are those reported in Table 2. In Fig. 26 both viscosity and thermal conductivity are shown as a function of temperature. Melted paraffin-wax diffusion coefficient is derived by Eq. (23) as for all other species.

Table 2: Liquid-like paraffin-wax transport properties coefficients [6, 7, 8].

Coefficient	Value
A_μ	104.67374020
B_μ	-14186.44194
C_μ	-13.54367495
D_μ	-0.000003161
E_μ	2129422.1620
A_k	0.2083972160
B_k	-0.000142555

5.3 PARAFFIN-WAX THERMAL CRACKING

In the present model the melted paraffin-wax is directly injected into the port. On one side, because of the lower heat per unit mass required by the melting rather than the pyrolysis process, this makes the model intrinsically able to take into account the higher tendency of paraffin-based fuels to regress. On the other side, this requires an additional effort to model the way the melted paraffin-wax is decomposed before producing gaseous species actually working as fuels in the combustion process. The following thermal cracking reaction is introduced for the purpose:



Notice that ethylene is one of the most relevant products of paraffin-wax thermal cracking [110] and for the sake of simplicity is accordingly assumed to be

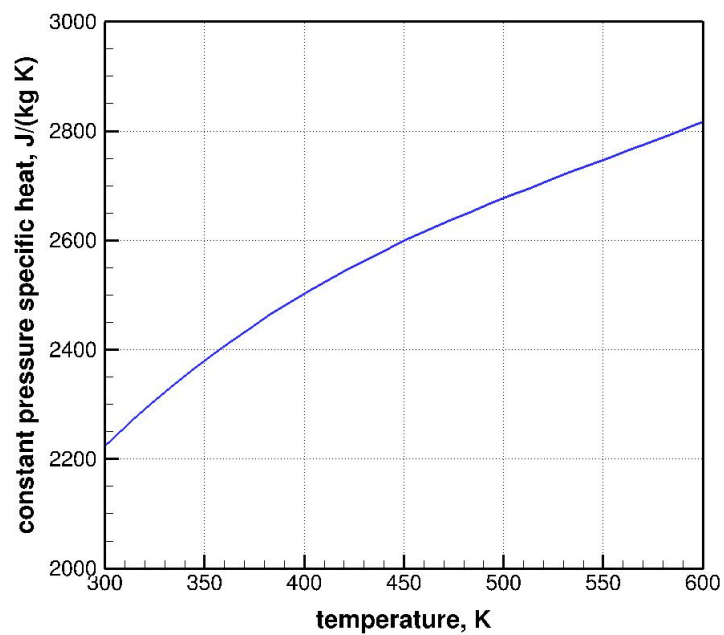


Figure 25: Liquid-like paraffin-wax constant pressure specific heat behavior with temperature.

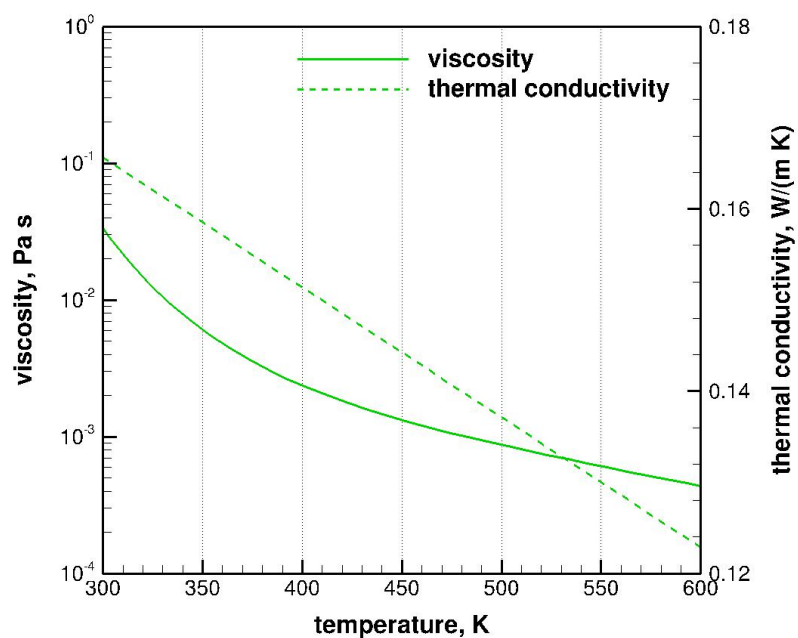


Figure 26: Liquid-like paraffin-wax transport properties behavior with temperature.

the representative cracking product. Molecular hydrogen is also introduced in the reaction step to allow the balance of number of atoms. Since thermal cracking of paraffins follows approximately a first-order kinetics [110], its reaction rate can be computed as:

$$v_{tc} = k_{tc}[C_{32}H_{66}] \quad (84)$$

with the reaction rate constant modeled as usual through an Arrhenius-type equation (see Fig. 27):

$$k_{tc} = A T^n \exp\left(-\frac{E_a}{RT}\right) \quad (85)$$

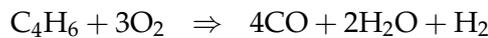
where the pre-exponential factor, temperature exponent and activation energy are those reported in Table 3 according to Ref. [9]. Notice that the reaction rate parameters presented in Ref. [9] are relevant to the thermal cracking of liquid $C_{16}H_{34}$ but they are assumed here to be valid also for $C_{32}H_{66}$ because of the lack of literature data for paraffins with a higher carbon number than 16.

Table 3: Supercritical paraffin-wax parameters for thermal cracking rate constant [9].

Reaction rate	A	n	$E_a/R, K$
k_{tc} [9]	3.0900×10^{13}	0.0	29790.6

5.4 GLOBAL REACTION MECHANISM WITHOUT DISSOCIATIONS

A global reaction mechanism not accounting for dissociation reactions is firstly presented. A case limited to HTPB fuels is described, since a comparison of results with or without dissociation reactions will be presented for this class of fuels for model validation purposes. The mechanism involves six species and two reaction steps. The first step is irreversible and accounts for 1,3-butadiene (the main HTPB pyrolysis product [11]) combustion. The second step, reversible, describes the carbon dioxide formation process.



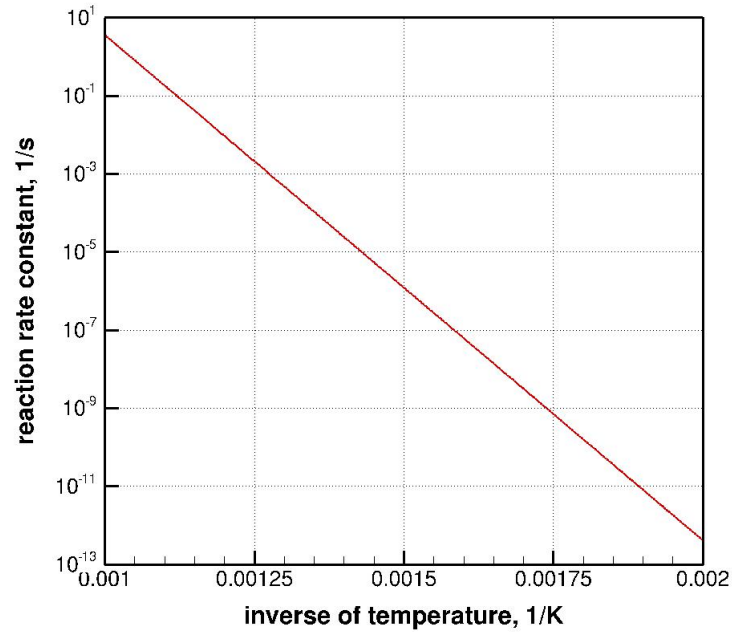


Figure 27: Supercritical paraffin–wax thermal cracking rate constant.

According to Ref. [36, 111] the reaction rates are given by:

$$v_1 = k_{f_1} [C_4H_6][O_2]$$

$$v_2 = k_{f_2} [CO][H_2O]^{0.5} [O_2]^{0.25} - k_{b_2} [CO_2][H_2O]^{0.5} [O_2]^{-0.25}$$

with reaction rate constants expressed as in Table 4.

Using Eq. (29) the chemical source terms for the species under scrutiny are obtained:

$$\dot{\omega}_{C_4H_6} = -M_{C_4H_6} v_1$$

$$\dot{\omega}_{O_2} = M_{O_2} (-3v_1 - 0.5v_2)$$

$$\dot{\omega}_{CO} = M_{CO} (4v_1 - v_2)$$

$$\dot{\omega}_{H_2O} = 2M_{H_2O} v_1$$

$$\dot{\omega}_{H_2} = M_{H_2} v_1$$

$$\dot{\omega}_{CO_2} = M_{CO_2} v_2$$

Table 4: Parameters of reaction rate constants for HTPB combustion without dissociations.

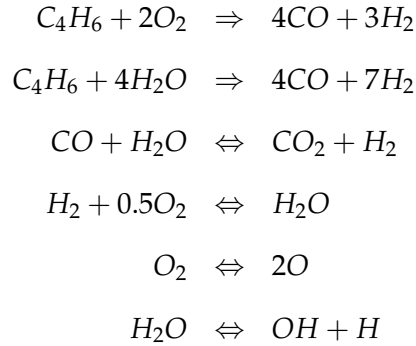
Reaction rate	A	n	$E_a/R, \text{K}$
k_{f_1} [36]	4.9486×10^9	0.0	15200.0
k_{f_2} [111]	2.2400×10^6	0.0	5032.7
k_{b_2} [111]	1.1000×10^{13}	-0.97	39456.5

5.5 GLOBAL REACTION MECHANISMS INCLUDING DISSOCIATIONS

Global reaction mechanisms for both HTPB and paraffin-based fuels are presented here including dissociation reactions. The purpose of such additional reaction steps is to improve combustion modeling, as well as internal ballistics predictions, by taking into account endothermic processes influencing both temperature and composition fields.

5.5.1 HTPB fuel

The mechanism involves nine species and six reaction steps. The first and second steps are irreversible and describe 1,3-butadiene reaction with oxygen and water vapor, respectively. All other steps are reversible and accounts for water-gas shift, water vapor formation, dissociation of molecular oxygen and dissociation of water vapor, respectively.



The mechanism, described in Ref. [112], shows the following reaction rates:

$$\begin{aligned}
 v_1 &= k_{f_1} [C_4H_6]^{0.5} [O_2]^{1.25} \\
 v_2 &= k_{f_2} [C_4H_6] [H_2O] \\
 v_3 &= k_{f_3} [CO] [H_2O] - k_{b_3} [CO_2] [H_2] \\
 v_4 &= k_{f_4} [H_2] [O_2]^{0.5} - k_{b_4} [H_2O] \\
 v_5 &= k_{f_5} [O_2] - k_{b_5} [O]^2 \\
 v_6 &= k_{f_6} [H_2O] - k_{b_6} [OH] [H]
 \end{aligned}$$

with reaction rate constants expressed as in Table 5.

From Eq. (29) the chemical source term of each species is evaluated as follows:

$$\begin{aligned}
 \dot{\omega}_{C_4H_6} &= M_{C_4H_6} (-v_1 - v_2) \\
 \dot{\omega}_{O_2} &= M_{O_2} (-2v_1 - 0.5v_4 - v_5) \\
 \dot{\omega}_{H_2O} &= M_{H_2O} (-4v_2 - v_3 + v_4 - v_6) \\
 \dot{\omega}_{CO} &= M_{CO} (4v_1 + 4v_2 - v_3) \\
 \dot{\omega}_{CO_2} &= M_{CO_2} v_3 \\
 \dot{\omega}_{H_2} &= M_{H_2} (3v_1 + 7v_2 + v_3 - v_4) \\
 \dot{\omega}_O &= 2M_O v_5 \\
 \dot{\omega}_H &= M_H v_6 \\
 \dot{\omega}_{OH} &= M_{OH} v_6
 \end{aligned}$$

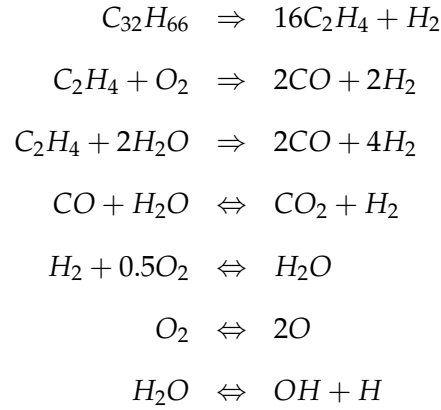
5.5.2 Paraffin-wax fuel

The mechanism for paraffin-wax is enriched with respect to the HTPB case of an additional species and reaction step. This is needed to account for thermal cracking of melted paraffin-wax as previously described. Such step is coupled to the global

Table 5: Parameters of reaction rate constants for HTPB combustion including dissociations.

Reaction rate	A	n	$E_a/R, \text{K}$
k_{f_1} [112]	9.1100×10^{13}	0.0	15702.1
k_{f_2} [112]	3.4800×10^{11}	0.0	15400.1
k_{f_3} [112]	2.9000×10^{12}	0.0	9612.50
k_{f_4} [112]	2.8000×10^{18}	-1.0	21691.0
k_{f_5} [112]	1.5000×10^{09}	0.0	56869.6
k_{f_6} [112]	2.3000×10^{22}	-3.0	60392.5

mechanism for 1,3-butadiene, adapted here to the case of ethylene in terms of stoichiometric coefficients.



The mechanism, obtained by coupling thermal cracking from Ref. [9] and the other steps from Ref. [112], shows the following reaction rates:

$$\begin{aligned}
 v_1 &= k_{f_1} [C_{32}H_{66}] \\
 v_2 &= k_{f_2} [C_2H_4]^{0.5} [O_2]^{1.25} \\
 v_3 &= k_{f_3} [C_2H_4] [H_2O] \\
 v_4 &= k_{f_4} [CO] [H_2O] - k_{b_4} [CO_2] [H_2] \\
 v_5 &= k_{f_5} [H_2] [O_2]^{0.5} - k_{b_5} [H_2O] \\
 v_6 &= k_{f_6} [O_2] - k_{b_6} [O]^2 \\
 v_7 &= k_{f_7} [H_2O] - k_{b_7} [OH] [H]
 \end{aligned}$$

with reaction rate constants expressed as in Table 6. Notice that the reaction rate constants for ethylene combustion have been assumed to be the same of 1,3-butadiene. Such analogy is made for the sake of simplicity and the lack of global mechanisms available for ethylene combustion in HRE-like conditions. This admittedly leaves some uncertainty, which is however deemed of a weight comparable to those implied in others aspects of the model.

From Eq. (29) the chemical source term of each species is evaluated as follows:

$$\begin{aligned}
 \dot{\omega}_{C_{32}H_{66}} &= -M_{C_{32}H_{66}} v_1 \\
 \dot{\omega}_{C_2H_4} &= M_{C_2H_4} (16v_1 - v_2 - v_3) \\
 \dot{\omega}_{O_2} &= M_{O_2} (-v_2 - 0.5v_5 - v_6) \\
 \dot{\omega}_{H_2O} &= M_{H_2O} (-2v_3 - v_4 + v_5 - v_7) \\
 \dot{\omega}_{CO} &= M_{CO} (2v_2 + 2v_3 - v_4) \\
 \dot{\omega}_{CO_2} &= M_{CO_2} v_4 \\
 \dot{\omega}_{H_2} &= M_{H_2} (v_1 + 2v_2 + 4v_3 + v_4 - v_5) \\
 \dot{\omega}_O &= 2M_O v_6 \\
 \dot{\omega}_H &= M_H v_7 \\
 \dot{\omega}_{OH} &= M_{OH} v_7
 \end{aligned}$$

Table 6: Parameters of reaction rate constants for paraffin–wax combustion including dissociations.

Reaction rate	A	n	$E_a/R, \text{K}$
k_{f_1} [9]	3.0900×10^{13}	0.0	29790.6
k_{f_2} [112]	9.1100×10^{13}	0.0	15702.1
k_{f_3} [112]	3.4800×10^{11}	0.0	15400.1
k_{f_4} [112]	2.9000×10^{12}	0.0	9612.50
k_{f_5} [112]	2.8000×10^{18}	−1.0	21691.0
k_{f_6} [112]	1.5000×10^{09}	0.0	56869.6
k_{f_7} [112]	2.3000×10^{22}	−3.0	60392.5

VALIDATION: HTPB CASE STUDY

6.1 OVERVIEW

In this chapter, preliminary results obtained with the HTPB fuel model are presented. The purpose is to analyze the coupling of gas–surface interaction, thermal radiation and thermochemistry models in the internal ballistics of HREs, by leaving out additional specific assumptions made for paraffin–wax. The role of thermal radiation and dissociation reactions on the internal ballistics prediction are examined, as well as the effects associated with their coupling. For validation, a test campaign, presented in the following section, has been fully simulated.

6.2 EXPERIMENTAL TEST CASES

The operational research project on hybrid rocket engine in Europe (ORPHEE) test campaign, performed on a gaseous–oxygen/HTPB lab–scale HRE, designed and built at the University of Naples *Federico II*, is taken as experimental benchmark [39, 40]. The test campaign includes nine different static firing tests performed with pure HTPB grains, whose average results are summarized in Table 7.

The space– and time–averaged regression rate in Table 7 is calculated with the fuel mass loss method [39, 40], based on the measured burned fuel mass ΔM_f . This method has been demonstrated to be the most accurate in describing the classical regression rate power law with mass flux [113]. After the burning time t_b is evaluated from the pressure trace by the well assessed procedure in Ref. [39], the time–averaged fuel mass flux is determined:

$$\bar{m}_f = \frac{\Delta M_f}{t_b} \quad (86)$$

Table 7: ORPHEE test campaign average data [10].

Firing test	\bar{G}_o , kg/m ² s	\bar{p}_c , bar	\bar{D} , mm	\bar{r} , mm/s	O/F
1	39.7	3.9	28.7	0.56	0.95
2	55.0	10.3	40.8	0.66	1.58
3	59.8	18.8	53.9	0.77	1.90
4	128.9	11.4	29.3	0.92	1.89
5	145.4	17.9	35.5	1.13	2.09
6	180.3	31.4	43.3	1.26	2.81
7	210.6	14.6	26.4	1.19	2.13
8	219.1	22.9	32.8	1.39	2.35
9	225.4	33.5	40.4	1.60	2.59

at the same time, the space-average over the grain axis of the final port diameter is obtained:

$$\hat{D}_2 = \sqrt{D_1^2 + \frac{4\Delta M_f}{\pi\rho_s L}} \quad (87)$$

in such a way the space- and time-averaged port diameter can be simply derived:

$$\bar{D} = \frac{D_1 + \hat{D}_2}{2} \quad (88)$$

the space- and time-averaged oxidizer mass flux is then calculated:

$$\bar{G}_o = \frac{4\bar{\dot{m}}_o}{\pi\bar{D}^2} \quad (89)$$

as well as the space- and time-averaged regression rate:

$$\bar{r} = \frac{\bar{\dot{m}}_f}{\rho_s\pi\bar{D}L} \quad (90)$$

The HRE under consideration is presented in Fig. 28. The oxidizer is supplied to the motor by a rack of eight cylinders connected to a feed line, equipped with a pressure regulator and a choking venturi to control and measure the mass flow rate.

An axial injector employing a converging nozzle, with 8 mm exit diameter, allows to provide the oxidizer into the axisymmetric combustion chamber of 720 mm in length and 133 mm of inner diameter. The fuel grain has a cylindrical shape with a single port geometry. It is 574 mm long with a 20 mm initial port diameter. A stainless steel pre-chamber and a thermally insulated post-chamber are set up ahead and aft of the fuel grain, respectively. The pre-chamber is 65 mm long with 80 mm inner diameter. The post-chamber, with the same length, has 70 mm inner diameter. A water-cooled conical converging-diverging nozzle in copper-alloy, with 16 mm throat diameter, 82 mm of length and a 2.4 area ratio, ensures long-duration firings without throat erosion. Motor ignition is accomplished using an electrically driven pyrotechnic cartridge. Chamber pressure is measured by two capacitive transducers set up in the pre- and post-chamber. The analog signals are sampled at 10 kHz, digitally converted with 16-bit resolution, processed and recorded. An ultrasonic transducer is set up nearby the middle of the chamber to measure the time-resolved local grain thickness and the fuel regression rate by means of the ultrasound pulse-echo technique presented in Ref. [114]. No data acquired with this technique are, however, presented in this work.

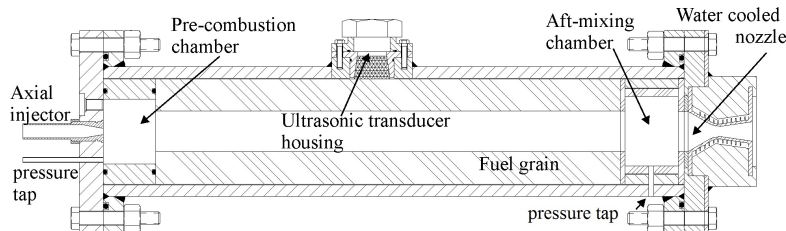


Figure 28: Gaseous-oxygen/HTPB lab-scale HRE schematic, from [5].

6.3 CFD GRID AND BOUNDARY CONDITIONS

In both CFD and DTM computations, the details of the pre- and post-chamber cavities are not modeled in the radial direction to allow relatively modest grid sizes. The adopted geometrical simplification of constant cross section has been found to be a fair assumption in Ref. [5]. In fact, even if the simplification has an effect on the chamber pressure, the regression rate has been found quite insensitive to such approximate geometrical configuration. In addition, the port area is based

on the time-averaged port diameter. According to Ref. [41], in fact, regression rates computed by simulations using the time-averaged port diameter represent a very good approximation of computed time-averaged regression rates.

In CFD axisymmetric simulations a grid of 170×60 elements, respectively in the axial and radial directions, has been selected after a grid convergence procedure. A proper grid refinement in the injection, near-wall and throat regions has also been introduced in order to capture the strong recirculation zone induced by the axial injection, the phenomena occurring into the boundary layer, as well as the transition through the sonic conditions. The experimental value of oxidizer temperature and mass flux are enforced as boundary condition at the inlet surface. At the outlet, a supersonic outflow boundary condition is set up. All chamber walls are modeled as isothermal with the exception of the grain interface. Here, the wall mass addition and mixture composition are computed through the GSI boundary condition for non-liquefying fuels. For the latter, the main product of HTPB pyrolysis is assumed to be 1,3-butadiene, i.e. C_4H_6 [11], while pre-exponential factor and activation energy for the pyrolysis model are reported in Table 8. Moreover, the HTPB grain properties needed for the calculation procedure are summarized in Table 9. The grid adopted together with the enforced boundary conditions are shown in Fig. 29.

Table 8: HTPB chemical kinetics [11].

Surface reaction	A , kg/m ² s	E_a , kJ/mol
HTPB _s → C ₄ H ₆	2.208×10^3	56.5

Table 9: HTPB grain properties [12, 13].

ρ_s , kg/m ³	c_s , J/kg K	Δh_{pyr} , MJ/kg
960	1632	1.10

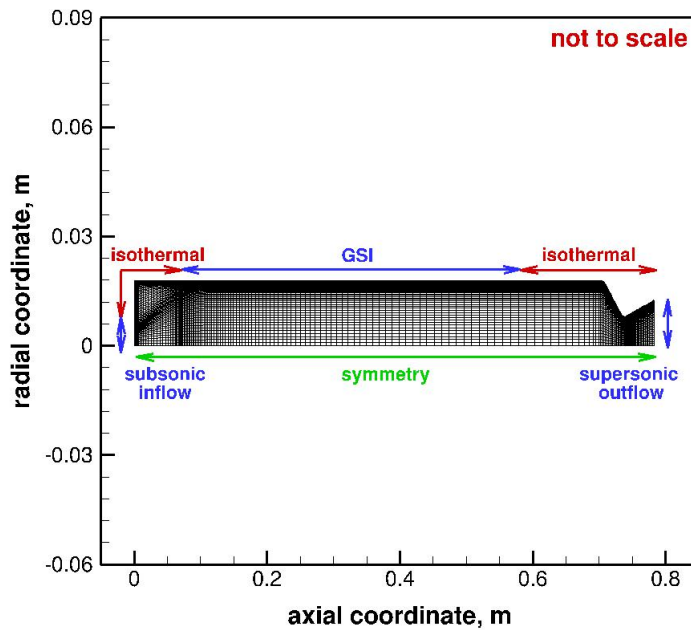


Figure 29: Adopted grid and boundary conditions, HTPB case study.

For DTM simulations, a discretization consisting in 256 rays for each calculation point and a step of 1 mm along each ray, has been used after performing convergence analyses for both parameters. Moreover, a wall emissivity equal to 0.85 has been assumed as reference for HTPB according to Eq. (70) with a refractive index of 1.73 according to Ref. [115].

An iterative procedure which couples CFD and DTM simulations has been implemented in order to take into account the effect that the radiative wall heat flux has on the fuel regression rate and, in turn, the effects that the modified flow field has on the radiative heat exchange.

6.4 ROLE OF OPERATING CONDITIONS ON THERMAL RADIATION

Before showing full CFD model results, an analysis of the role played by different operating conditions on the magnitude attained by the radiative wall heat flux is carried out by simplified and decoupled DTM simulations. A cylindrical geometry filled by a homogeneous medium is employed for the purpose, allowing fast calculations. Both the adopted cylinder dimensions, in terms of length and diame-

ter, and the medium conditions, obtained from CEA at the stoichiometric mixture ratio, are sized to mimic realistic conditions in Table 7. In particular, a parametric analysis with chamber pressure and port diameter is carried out. The pressure, used as independent variable, is varied assuming the values of 10, 30, 50, 75 and 100 bar. The diameter, on the other hand, is varied as a parameter assuming the values of 0.01, 0.1 and 1 m. The results of the parametric analysis are presented in Fig. 30 in terms of radiative wall heat flux normalized with respect to the black body emissive power, i.e. in terms of the medium global emissivity.

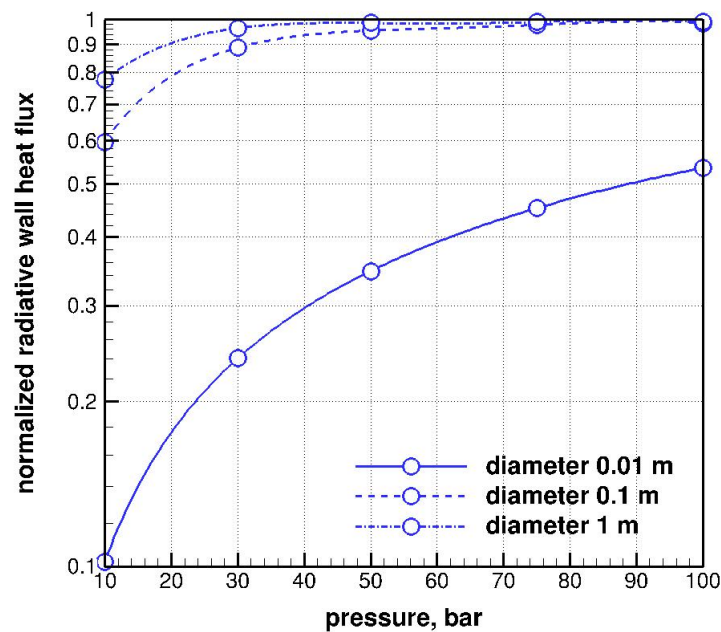


Figure 30: Role of pressure and diameter on the medium global emissivity.

The radiative wall heat flux is observed to increase with both pressure and diameter, exhibiting saturation when sufficiently high values are attained. The growth of thermal radiation with pressure and diameter agrees with the fact that they influence in a similar way the number of the absorbing/emitting particles encountered by the radiation along its path length, i.e. the medium optical thickness, and hence the way the gas participates to the radiative heat exchange. It can be also stated that, if pressure or diameter assume high values, the gaseous medium tends to behave like a black body, since the global emissivity tends to unity; while if small values are considered, the gaseous medium tends to become non-participating, since the

global emissivity tends to zero. When the black body condition is reached, the radiative wall heat flux saturates and it does not change with a further increase in pressure or diameter, while it is no more affected by the presence of the gas, when the non-participating condition is attained. Notice that similar considerations can be done by using an even more simplified model, like that represented by Eq. (72), valid for a homogeneous medium in between plane parallel surfaces.

For typical HRE conditions, i.e. chamber pressures in the range of 10–50 bar and port diameters of the order of 0.1 m, an intermediate condition is found. In fact, the gaseous mixture behaves like a participating/non-black medium, with global emissivities ranging between about 0.6 and 0.9. Such a rough estimate can undergo non-negligible deviations, estimated to be 30% on average, when actual thrust chamber geometries, as well as typical hybrid rocket temperature and composition stratification, are accounted for in the computations.

The product between pressure and diameter, pD , plays a role also in determining to what an extent the value assumed for the wall emissivity is important to attain sufficiently accurate predictions. For high pD products, when the medium is optically thick, the radiation reflected by the wall is completely re-absorbed by the medium, thus not participating anymore to the wall heating. For low pD products, on the other hand, the radiation reflected by the wall, because of an optically thin medium condition, goes back again to the wall by multiple reflections, contributing to the wall heat transfer. If one remembers that the reflected part of the irradiation is the complement to unity of the wall emissivity, according to Eq. (69), it is clear that the wall emissivity sets what is the net fraction of the irradiation not contributing to the wall heating for high pD products, while assuming a minor role when low pD products are envisaged. Such an aspect is highlighted in Fig. 31 where the ratio between radiative wall heat fluxes, computed with a gray and black wall boundary condition, respectively, is shown as a function of pD . The previous cylindrical geometry and homogeneous medium are used with the same values of pressure and diameter. The 10 bar pressure is discarded to avoid multiple points for the same pD . A value of 0.85 is set up for the wall emissivity.

As expected, the ratio approaches the wall emissivity value for high pD , while it is less affected by the chosen wall emissivity when pD is low.

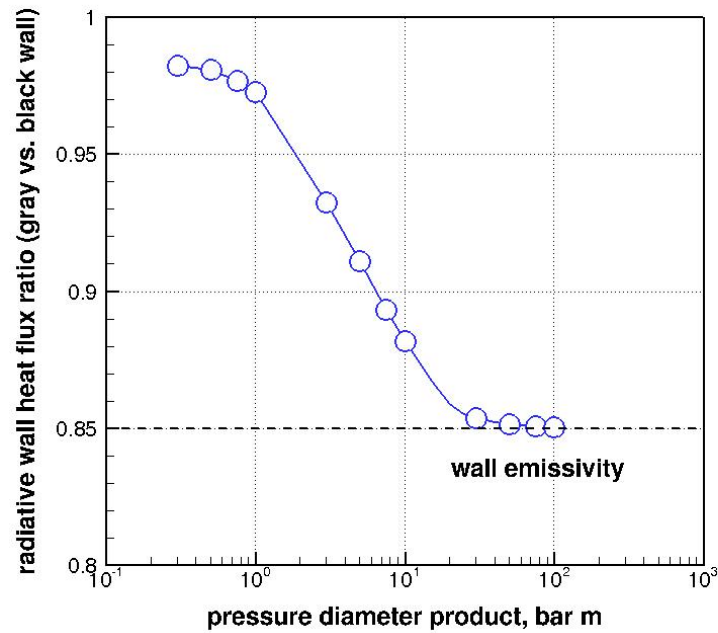


Figure 31: Ratio of radiative wall heat fluxes obtained with gray and black wall treatment.

Before concluding, it should be noted that in the present analysis the gaseous mixture mass flux has not played any role. Therefore, although more detailed analyses based on CFD simulations are needed to investigate the role of the mass flux on the radiative heat exchange, it is expected that the mass flux does not directly affect the achieved level of radiative heat flux. In any case, since the convective contribution decreases with decreasing mass fluxes, the radiative one is expected to represent a higher percentage of the whole heat transferred to the walls when low mass fluxes are envisaged. This behavior justifies the deviation from the standard Marxman's law observed at low mass fluxes, when the pD product becomes important to predict regression rate through simple boundary layer theory [17].

6.5 EFFECTS OF RADIATION AND DISSOCIATION ON THE FLOW FIELD

In order to discuss the effect of including thermal radiation and dissociation reactions on the flow field prediction, a specific firing test is taken as reference. Looking for intermediate conditions of chamber pressure, port diameter and achieved regression rate, firing test 5 is selected among those reported in Table 7. Three iter-

ations between CFD and DTM simulations are needed for such firing test in order to obtain a final converged solution.

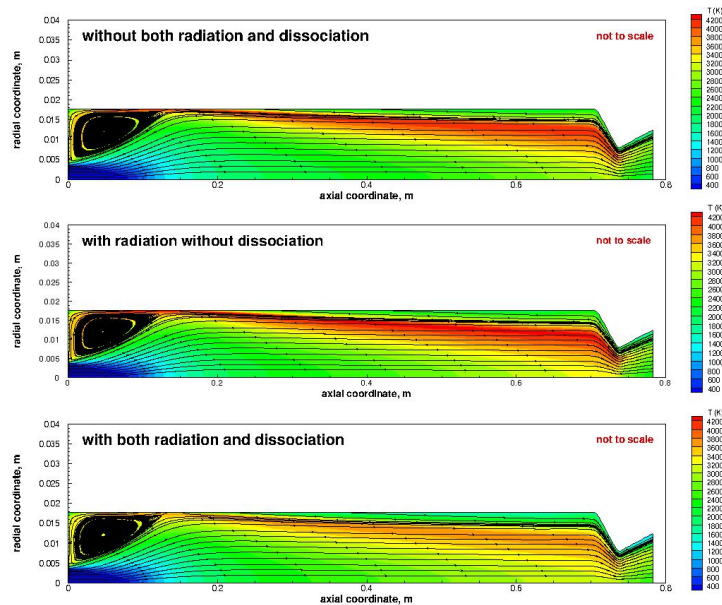


Figure 32: Effects of radiation and dissociation on the computed temperature field.

Calculated temperature fields with streamlines are presented in Fig. 32. Three different levels of detail for the model are examined, first adding the radiation, then also adding dissociations to a baseline solution without the modeling of both phenomena. This allows to stress the effects on the flow field associated to the modeling of both radiation and dissociations, singularly. In all cases the broad recirculation region due to axial injection and the diffusion flame typical of hybrid rockets are well captured. The inclusion of radiation leads the flame to wide and move away from the wall because of the enhanced blowing effect. Adding dissociations, on the other hand, leads the temperature field to be significantly reduced because of the included endothermic process, with the flame temperature decaying of about 14%, moving roughly from 4300 to 3700 K.

In Fig. 33 the radiative wall heat flux profiles computed either without or with dissociations are presented. In both cases, just after chamber entrance, a maximum due to the hot flow coming from the flame and trapped by the vortex near the wall surface is found. Then the radiative wall heat flux exhibits first an increase then a decrease, due to a compensating effect between flame thickening and increasing wall-to-flame distance. Into the nozzle region the thermal radiation at wall is af-

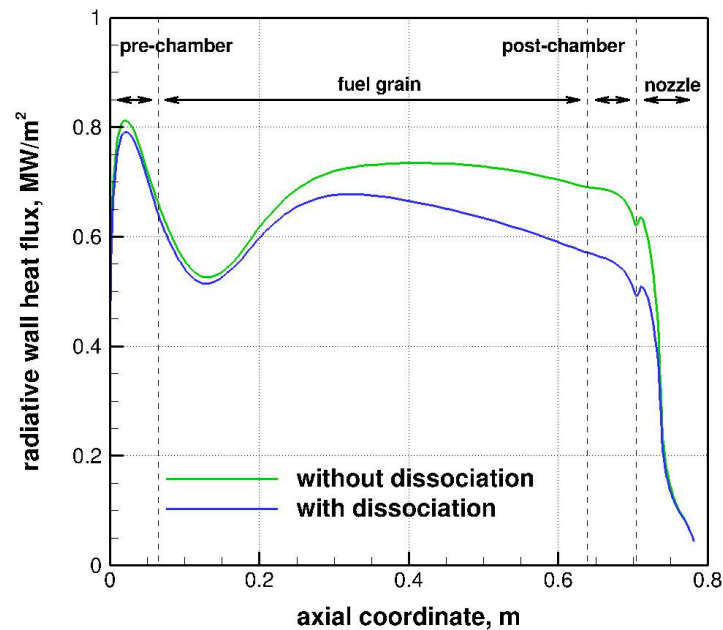


Figure 33: Radiative wall heat flux profiles with and without considering dissociation.

ected by geometry changes, while undergoing a strong reduction associated to the flow expansion. When dissociations are accounted for, the average radiative wall heat flux is reduced by about 9%, moving from 0.64 to 0.58 MW/m² average values, because of reduced temperatures. Despite such average reduction, the radiative flux qualitative behavior appears almost unchanged. The major difference is found in the second half of the fuel grain length, as soon as the flame starts to be detached from the wall surface. Here the decay of the radiative wall heat flux appears to a certain extent enhanced when including dissociations. The reason is that, while in the flame zone the temperature is significantly reduced, in the colder region, in between the flame zone and the wall surface, the temperature is almost unchanged with respect to the case without dissociations. Accordingly, while the emission from the flame is reduced, the absorption occurring near the wall surface is almost unchanged, generating the observed effect.

In Fig. 34 the different contributions to the total wall heat flux are pointed out. The radiative contribution clearly appears to play a non-negligible role in the wall heating. In particular, it is important all along the combustion chamber, thus significantly affecting the regression rate, while it appears to be negligible in the nozzle,

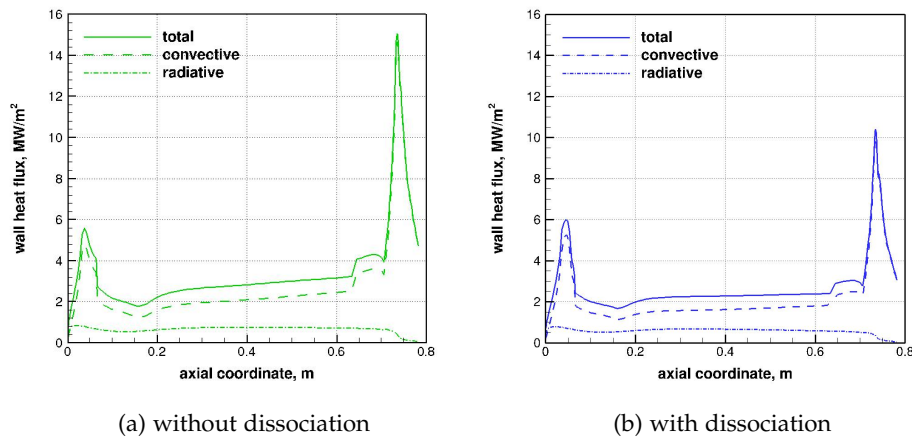


Figure 34: Contributions to the wall heat flux, HTPB case study.

where the peak of convection at throat is superimposed to the decrease of radiation. Despite the radiative wall heat flux is reduced in the case with dissociation, its relative contribution to the total value appears slightly increased because of a higher decay of the convective contribution. In fact, the radiative contribution stands around the 21% and the 19% of the total wall heat flux in the case with and without dissociations modeling, respectively.

Obviously, including the radiative wall heat flux into the wall energy balance determines an increase in the predicted regression rate. This is highlighted in Fig. 35 which also shows the convergence of the iterative procedure that couples CFD and DTM simulations. As expected, the regression rate is reduced to a non-negligible extent, that is about 16%, moving from 1.32 to 1.11 mm/s, when dissociation reactions are included.

6.6 REBUILDING RESULTS AND COMPARISON WITH TEST DATA

All of the ORPHEE firing tests are considered in this section in order to extend the previous considerations to the whole test campaign and evaluate the ability of the numerical setup to reproduce the experimental results. The number of iterations required to attain convergence between CFD and DTM varied between two and four depending on the magnitude of the radiative wall heat flux for each firing test, hence by the operating conditions.

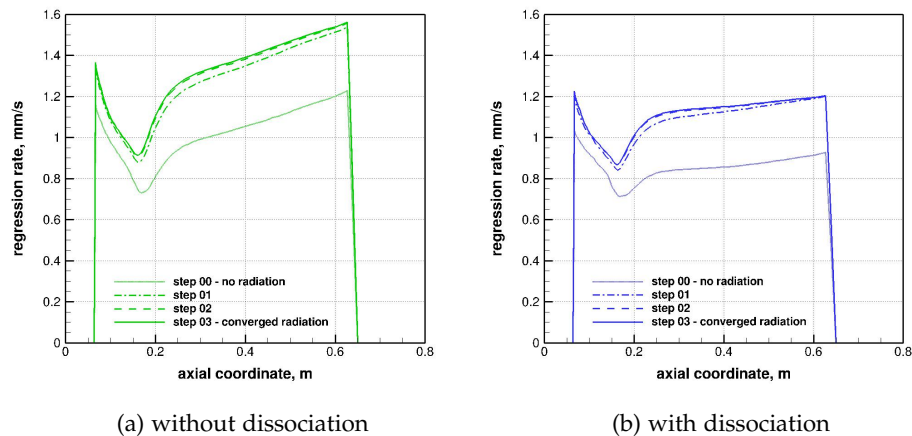


Figure 35: Regression rate evolution with iterations, HTPB case study.

The radiative contribution with respect to the total wall heat flux ranges between 10%, in the firing test 7, and 41%, in the firing test 3. Such percentages, averaged along the motor length, include contributions into the nozzle region, which are in favor of the convective heat flux. Higher percentages can be found along the port, with the radiative heat flux being potentially higher than the convective heat flux at certain grain locations. Notice that test cases 7 and 3 are those with the lowest and the highest port diameter, respectively. This highlights that quite small changes in the port diameter can significantly influence the extent to which the thermal radiation affects the total wall heating. Not only the dependence of radiation, but also that of convection, is responsible for such strong effect. On one side the radiative wall heat flux increases with port diameter because of the volumetric radiative source scaling up with the volume to surface ratio, as explained in Sec. 6.4 and well described in Ref. [31]. On the other side, the convective heat flux decreases with port diameter because of the shallow temperature gradient at wall, that is when the flame is farthest from the wall, attained for high motor sizes [31]. When axial injection is envisaged, more attention needs to be paid because of additional superimposed effects to both heat transfer contributions. Notice in fact that, with increasing the diameter of the port, with respect to that of the injector, the vortex widens, enters the port and impinges further downstream along the fuel grain, with non-negligible effects on both convective and radiative contributions. As described in detail in Ref. [5], convection is enhanced by the improved mixing

associated with a wider vortex. Also radiation is enhanced in the upstream part of the fuel grain length. In fact, when for high diameters the vortex enters the port, part of the hot flow coming from the flame gets trapped into the vortex, in such a way a thick hot region attached to the wall is formed, which gives a significant contribution to the local radiative wall heat flux. Figure 36 compares test cases 7 and 3, showing how different port diameters can affect the flow field, as well as the vortex and flame structures. Figure 37, in particular, shows the effect of a higher port diameter on the radiative wall heat flux magnitude and profile. While a cold and small vortex, confined in the pre-chamber, is found for firing test 7, a hot and wide vortex, extended into the port, is found for firing test 3. The result is that, superimposed to the different magnitude, as expected from previous considerations in Sec. 6.4, a completely different radiative heat flux profile is found in the upstream part of the port length.

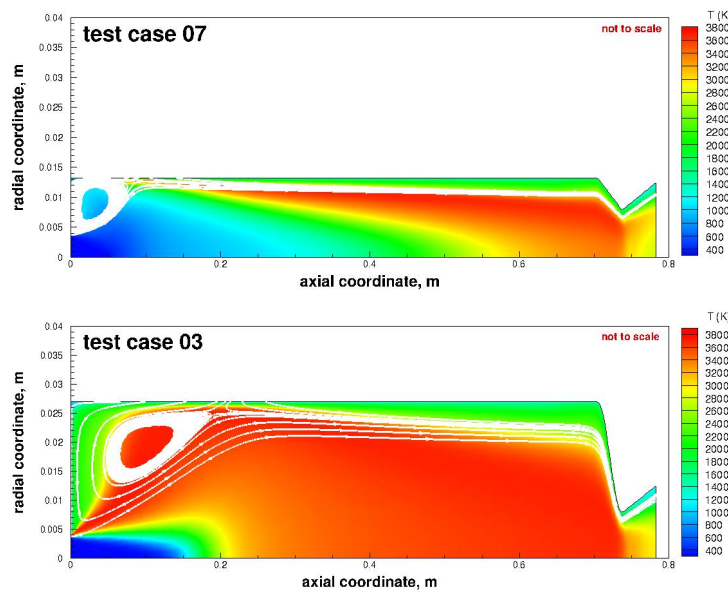


Figure 36: Port diameter effect on the flow field.

The comparison between numerical results and experimental data in terms of space- and time-averaged regression rate and chamber pressure are presented in Figs. 38 and 39, respectively. For all test cases, the regression rate is increased by including the radiative flux into the wall energy balance. Because of the overestimated temperature field in the case without including dissociations, the tendency in underestimating the measured value is turned into a slight overestimation of the

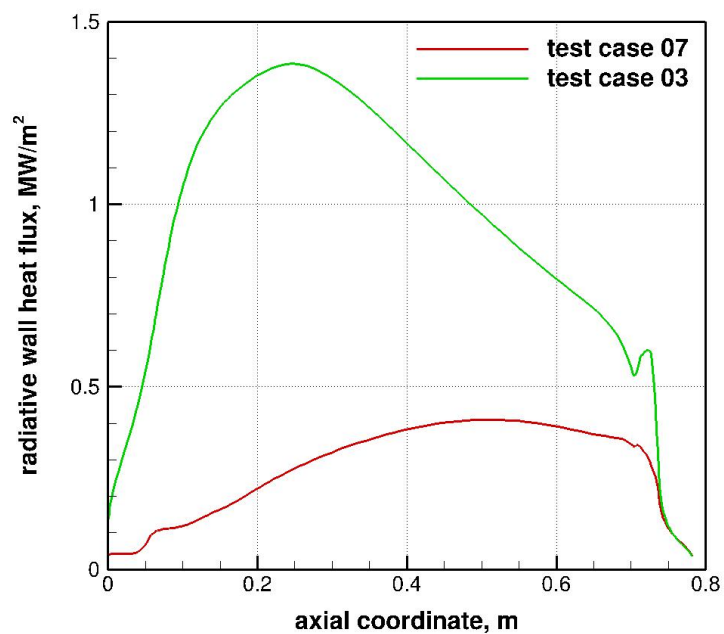


Figure 37: Port diameter effect on the radiative wall heat flux magnitude and profile.

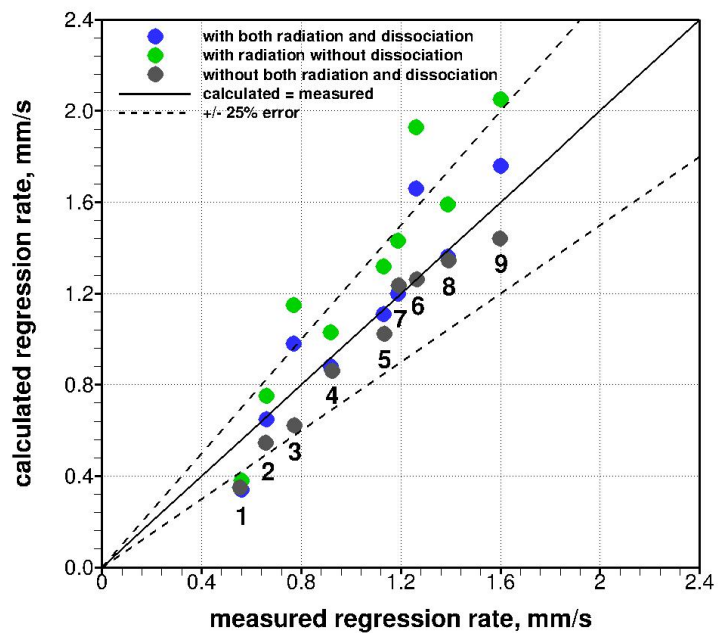


Figure 38: Comparison between computed and measured regression rates, HTPB case study.

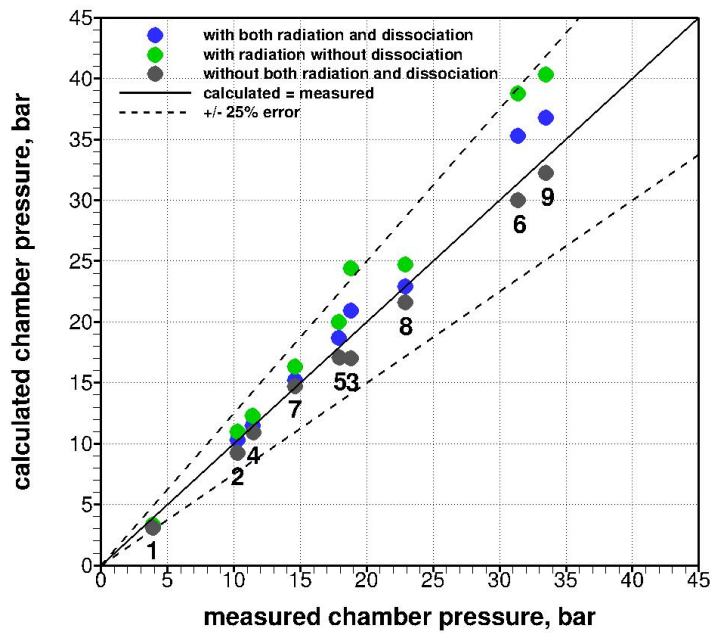


Figure 39: Comparison between computed and measured chamber pressures, HTPB case study.

regression rate. When also dissociations are included, this tendency is significantly mitigated with numerical results approaching quite well the experimental data. A similar behavior is found for chamber pressure. It is important to underline that the predicted chamber pressure is not only the result of the fuel regression rate but also of the combustion and mixing process within the combustion chamber, that can strongly affect the characteristic velocity. Hence, a correct prediction of the fuel regression rate does not necessarily guarantees that the chamber pressure is correctly predicted. If the mixing and combustion processes are not correctly modeled, in fact, a mismatch between predicted and measured chamber pressure will result.

From Fig. 38 the space- and time-averaged regression rate prediction of most firing tests appears very good when radiation and dissociations are included. In fact, for firing tests 2, 4, 5, 7 and 8, the average error on the computed regression rate is only about 2%. For the same test cases, also the space- and time-averaged chamber pressure is very well predicted, with an average discrepancy from experimental data of 3%, as shown in Fig. 39. Looking at test case 5, assumed as

reference in Sec. 6.5, the error on regression rate and chamber pressure are 1.8% and 0.9%, respectively, confirming a good ability of the numerical setup to rebuild the experimental data.

An exception is represented by test cases 3, 6 and 9 where a certain residual overestimation is found for both chamber pressure and regression rate, especially the latter. Not by chance, such test cases are those characterized by the highest values of pD , hence the highest computed radiative wall heat fluxes and, accordingly, the highest sensitivity to even slight over-predictions of the radiative contribution. According to the discussion in Sec. 6.4, a too high value selected for the wall emissivity can have a role in this effect.

A different behavior with respect to that observed for the majority of test conditions is found for test cases 1 and 7. In fact, when the complete model is adopted, the computed regression rates attain values even lower than those obtained without modeling both radiation and dissociations. This means that for such test cases the role played by dissociations in decreasing the convective wall heat flux is more important than the one directly played by including the radiative contribution. Notice that thermal radiation is very small for such test cases because of the low pD product.

Test case 1 features an anomalous underestimation of regression rate that should be attributed to aspects lacking in the model and playing a non-negligible role in such conditions. From one side test case 1 has the lowest pD product and a very low radiative contribution by gaseous phase. On the other, it is the most strongly fuel rich, with a mixture ratio of 0.948, and can probably experience a non-negligible radiative contribution by condensed phase, such as soot. Accordingly, soot radiation, not modeled here, can be dominant on gas phase radiation, justifying the anomalous prediction.

RESULTS: PARAFFIN–WAX CASE STUDY

7.1 OVERVIEW

In this chapter the results obtained with the full paraffin–wax model are presented. The capability of the numerical setup to capture the main features of paraffin–based HRE flow fields is highlighted. Attention is given to the study of diffusion flame characteristics and melted paraffin–wax concentration fields, as well as the different contributions to the wall heat transfer. After the ability of the combustion and mixing model to predict the motor characteristic velocity is evaluated, selected test cases are rebuilt to evaluate the internal ballistics prediction capability for different mass flux and chamber pressure conditions.

7.2 COMPARISON BETWEEN HTPB AND PARAFFIN–WAX MODELS

Before showing the results obtained for selected test cases using paraffin–wax as fuel, a comparison between paraffin–wax and HTPB models is carried out by considering again the lab–scale HRE of the University of Naples *Federico II*. For the purpose, the firing test 5, widely discussed in Chapter 6 as the reference test case, is simulated by assuming a paraffin–wax fuel grain in place of the standard HTPB one. The GSI boundary condition and thermochemistry description for paraffin–wax are used, while the same discretization presented in Chapter 6 is adopted for both CFD and DTM simulations. Also in this case three iterations are found sufficient to attain the convergence of the numerical solution.

The temperature fields with streamlines obtained with the paraffin–wax and HTPB models are compared in Fig. 40. Very similar recirculation regions are found. However, in spite of a similar maximum achieved temperature, very different flame structures are obtained. In the paraffin–wax case, in fact, the flame appears much

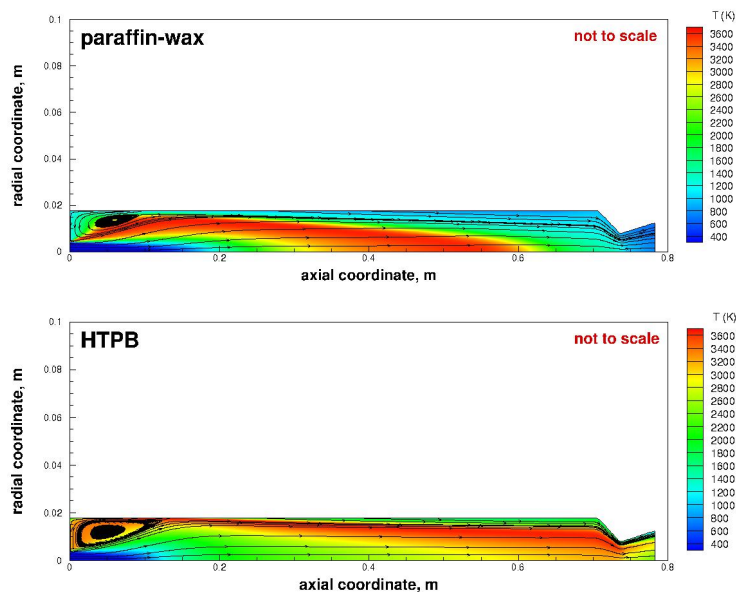


Figure 40: Comparison of temperature fields with streamlines for paraffin-wax and HTPB.

more blown away toward the symmetry axis, leading to unburned fuel and low temperatures at nozzle entry. Such temperature field configuration is indicative of a higher regression rate, as peculiar of paraffin-wax fuel grains. It denotes, at the same time, a lower achieved characteristic velocity than in the HTPB case, that is however only an effect of the motor design, that has not been optimized for actually employing paraffin-wax as fuel, which results in a significant fuel-rich condition.

The comparison of regression rate for paraffin-wax and HTPB fuels is shown in Figure 41. Besides a quite different behavior along the axis, in the paraffin-wax case the regression rate is increased of a value ranging in between 2.06 and 3.81 depending on the axial location. In particular, the average regression rate moves from 1.11 mm/s with HTPB to 3.70 mm/s with paraffin-wax, highlighting an average increase of 3.34 times that is in very good agreement with what is expected from literature data [26].

The increase of regression rate, associated to the different model, together with unchanged operative conditions, i.e. oxidizer mass flux, brings down the mixture ratio from 2.11 to 0.66 and, in turn, leads the characteristic velocity to be drastically reduced from 1678 m/s to 1094 m/s. As a consequence of the increased regression

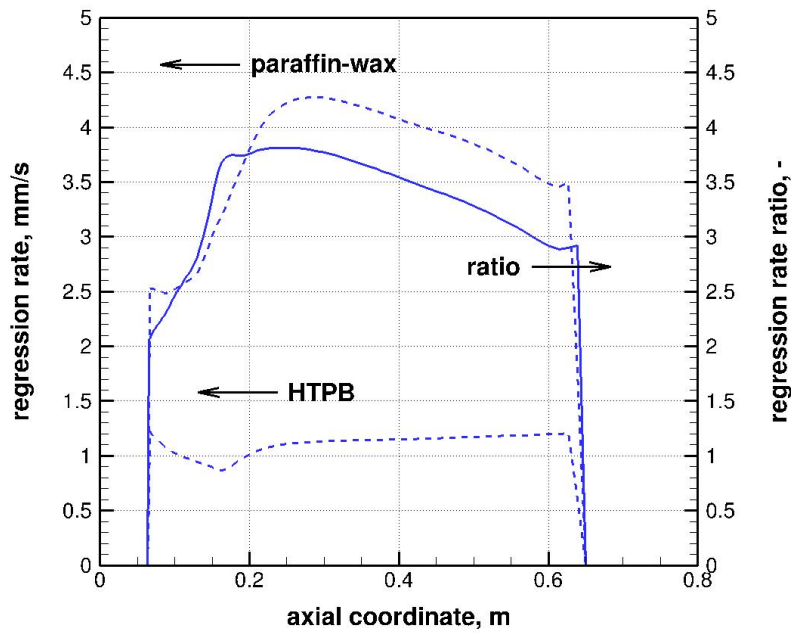


Figure 41: Comparison of regression rate profiles for paraffin-wax and HTPB.

rate and reduced characteristic velocity, the chamber pressure is found to only slightly increase, from 17.7 to 19.7 bar.

Looking at the different contributions to the wall heating, both the radiative and convective fluxes appear reduced by using paraffin-wax in place of HTPB, assuming average values of 0.31 and 0.48 MW/m², respectively. The radiative wall heat flux is reduced, in spite of a slightly higher pressure with the same diameter, because of the averagely colder temperature field. The low temperatures in the near-wall region leads also the convective contribution to be reduced in spite of an increased mass flux along the port. The radiative to total wall heat flux ratio is finally found to be increased from 21% to 39% because of the stronger reduction of the convective than the radiative contribution.

7.3 EXPERIMENTAL TEST CASES

Selected test cases of an experimental campaign performed at the HCF of NASA Ames Research Center [50], and aimed to verify the high regression rate behavior of paraffin-based fuels for conditions representative of flight applications, have

been simulated with the present comprehensive model for paraffin-wax regression and combustion. Four different operating conditions of the medium-scale gaseous-oxygen/paraffin-wax HRE under examination are considered, as summarized in Table 10. The test case L01 is assumed as reference. Test cases L04 and P01 are aimed at evaluating the numerical setup by singularly changing the mass flux and the chamber pressure, with respect to the reference operating conditions, respectively. The test case P04, finally, is simulated to look at completely different values of both parameters [14].

Table 10: Selected test case average data [14].

Firing test	\bar{G}_o , kg/m ² s	\bar{p}_c , bar	\bar{D} , mm	\bar{r} , mm/s	O/F
L01	270.5	45.7	143.9	3.66	2.57
L04	368.0	44.7	123.9	4.21	2.66
P01	274.1	21.6	143.4	3.51	2.69
P04	146.9	10.8	135.2	2.73	1.78

The space- and time-averaged regression rate in Table 10 is, similarly to the HTPB case, calculated with the fuel mass loss method, once the burned fuel mass ΔM_f and the burning time t_b are measured. The space-average over the grain axis of the final port diameter is first determined:

$$\hat{D}_2 = \sqrt{D_1^2 + \frac{4\Delta M_f}{\pi\rho_s L}} \quad (91)$$

before being corrected to exclude the non-negligible fuel mass consumed during the long termination transients [14]:

$$\tilde{D}_2 = f(\hat{D}_2) \quad (92)$$

the space- and time-averaged port diameter is then simply obtained:

$$\bar{D} = \frac{D_1 + \tilde{D}_2}{2} \quad (93)$$

in particular, the space- and time-averaged oxidizer mass flux is evaluated as:

$$\bar{G}_o = \frac{4\bar{m}_o}{\pi\bar{D}^2} \quad (94)$$

while the space- and time-averaged regression rate is simply obtained by the following formula:

$$\bar{r} = \frac{\tilde{D}_2 - D_1}{2t_b} \quad (95)$$

The HRE under consideration is presented in Fig. 42. The facility supporting the test article is equipped with an oxygen feed system capable of delivering up to 16 kg/s of ambient temperature gaseous-oxygen at chamber pressures ranging from about 10 to 68 bar. An axial injector with a constant cross section diameter of 50.8 mm provides the oxidizer into the axisymmetric combustion chamber of 1347.4 mm in length and 194.9 mm in inner diameter. The cylindrical single port fuel grain is spin casted into a paper phenolic tube before being inserted into the combustion chamber. Different initial port diameters, in between 75 and 130 mm, are used in the test campaign, as well as two different lengths, of 775 and 1148 mm, thanks to a modular combustion chamber. Only test cases with the higher length are considered in the present rebuilding. Both pre- and post-chamber cavities, of 120.6 and 78.7 mm in length, respectively, are thermally insulated with graphite materials. Graphite insulation is also used for the nozzle, employing different throat diameters, ranging from 36.8 to 71.6 mm, to allow significantly different pressure to be achieved in the combustion chamber. The motor is ignited by a fuel-rich methane-oxygen gas-gas system, initiated by two spark plugs located in the igniter chamber. Standard measurements during a run of the facility include time history of oxygen mass flow rate and chamber pressure [14].

7.4 CFD GRID AND BOUNDARY CONDITIONS

As in the HTPB case, in both CFD and DTM computations, the details of the pre- and post-chamber cavities are not modeled in the radial direction to allow relatively modest grid sizes [5], while the port area is based on the average port diameter to compute the time-averaged regression rate [41].

In CFD axisymmetric simulations the grid consists of 340 axial and 120 radial elements selected after a grid convergence procedure. A proper grid refinement in the injection, near-wall and throat regions has been introduced, similarly to the HTPB case, to capture the recirculation zone, the boundary layer and the transition

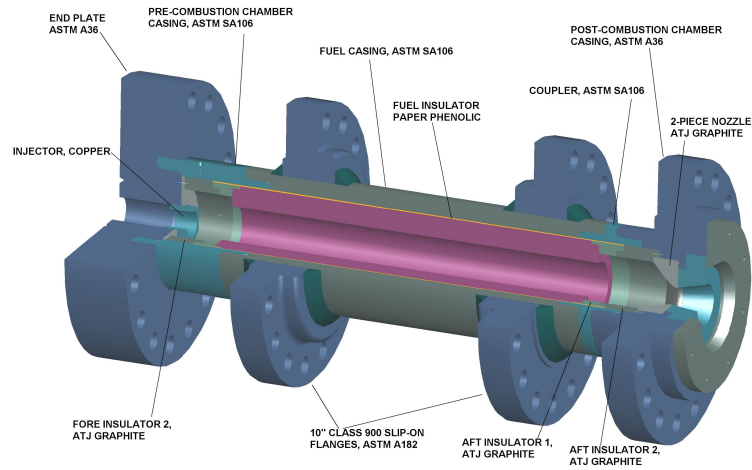


Figure 42: Gaseous-oxygen/paraffin-wax medium-scale HRE schematic (Credits Stanford).

through sonic conditions, respectively. A subsonic inflow boundary condition is set up at the inlet surface by specifying the experimental value of oxidizer temperature and mass flux. At the outlet surface, a supersonic outflow boundary condition is set up as usual. The chamber walls are modeled as adiabatic because of the unknown temperature achieved by the graphite insulations. Along the fuel grain surface, however, the GSI boundary condition for liquefying fuels is enforced to compute regression rate and wall mixture composition. As melting temperature for the paraffin-wax, a value of 342.15 K is used. Moreover, the paraffin-wax grain properties needed for the calculation procedure are summarized in Table 11. The adopted grid and boundary conditions are described in Fig. 43.

Table 11: Paraffin-wax grain properties [15, 16].

ρ_s , kg/m ³	c_s , J/kg K	Δh_{melt} , MJ/kg
920	2900	0.17

For DTM simulations a discretization consisting in 256 rays and a step of 1 mm has been verified to be adequate by a convergence analysis. Moreover, a wall

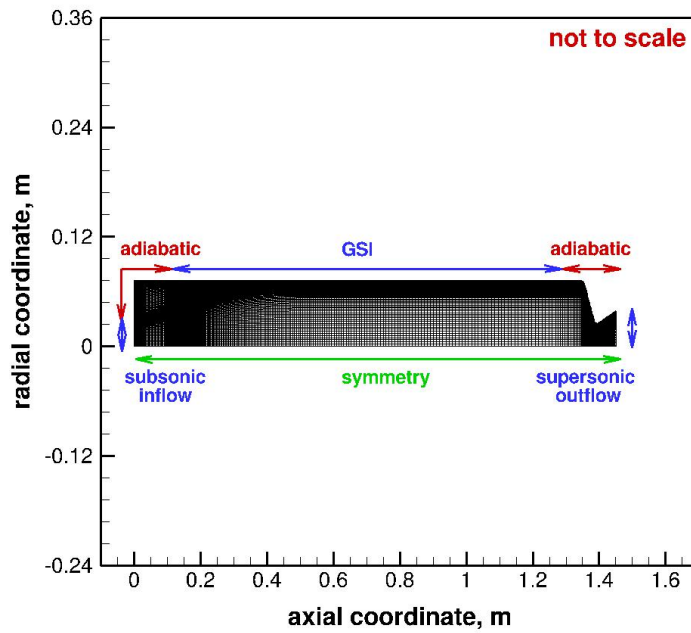


Figure 43: Adopted grid and boundary conditions, paraffin-wax case study.

emissivity equal to 0.91 has been assumed as reference for paraffin-wax by using Eq. (70) with a refractive index of 1.43 according to Ref. [116].

The coupling between flow field and radiative flux has been taken into account by the usual iterative procedure between CFD and DTM simulations.

7.5 GENERAL RESULTS FOR THE REFERENCE TEST CASE

In this section, the reference test case, i.e. L01, is examined. The purpose is to show general results achievable with the proposed comprehensive model for paraffin-wax regression and combustion. Since the need of a coupled radiation and dissociations model has been highlighted to be crucial to obtain reasonably good internal ballistics predictions, both phenomena are included in the present simulation. In particular, three iterations between CFD and DTM simulations are needed for firing test L01 in order to obtain a final converged solution.

The temperature field, including a detail with streamlines in the near-injector region, is shown in Fig. 44. A wide diffusion flame with temperatures up to about 3780 K is captured. The axial injection mode leads the formation of a strong re-

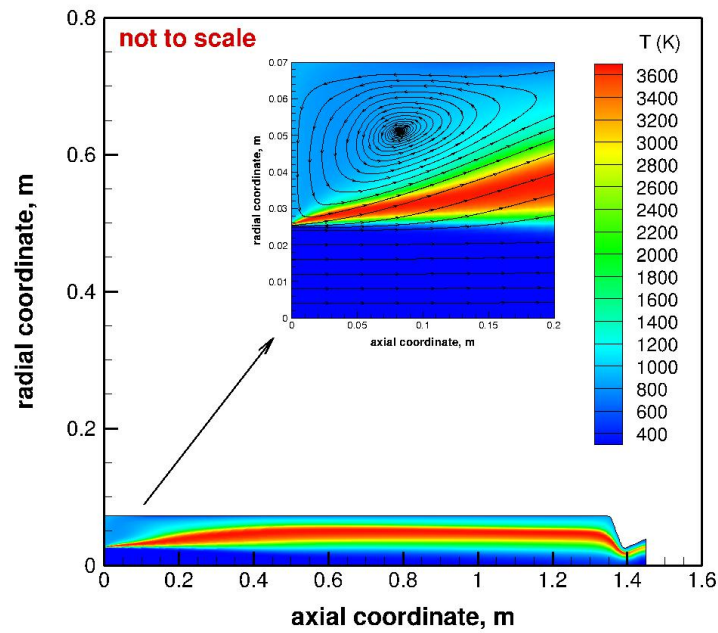


Figure 44: Temperature field with streamlines.

circulation region in the upstream part of the combustion chamber, which anchor the flame to the inlet surface. The flame structure appears quite flat and rather close to the wall surface. As a consequence, temperature not higher than 500 K are found at the centerline, with a portion of the core oxidizer remaining practically unburned. Such inefficient behavior has been proven to be grid independent. In Fig. 45 radial profiles of temperature and oxygen mass fraction at the exit of the grain length obtained by considering two grid levels are presented. In particular, the present mesh (fine grid) and a discretization obtained from the reference mesh by halving the number of elements in both axial and radial direction (coarse grid) are used. The results, show a fairly good agreement, although a smoother solution is found for the finer discretization.

The inefficient use of the oxidizer stream in the core flow is thought to be attributable to the quite large size of the motor under consideration. In fact, as evidenced in Ref. [31], with increasing the size of the combustion chamber, although the flame is further away from the wall in absolute dimensions, it appears nearer to grain surface in non-dimensional terms. Such an effect of the motor size is able to significantly affect the combustion efficiency. Very similar temperature fields

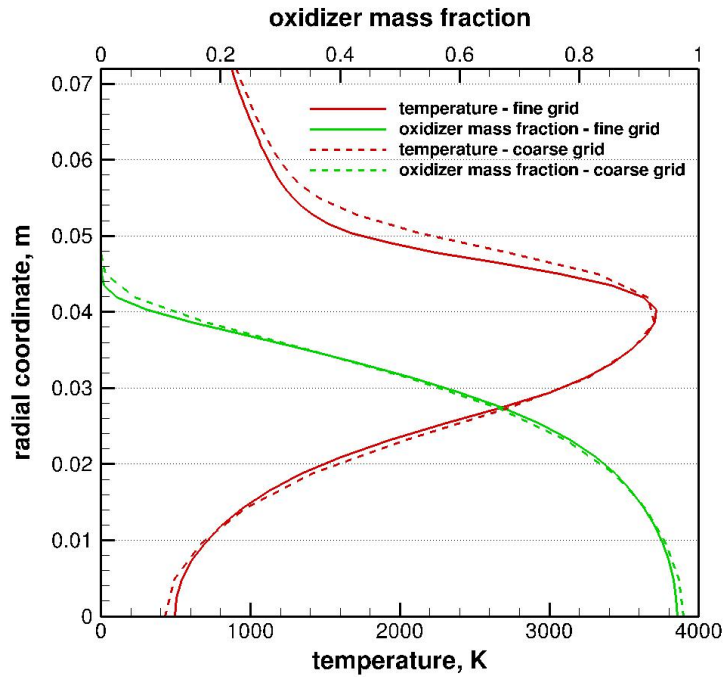


Figure 45: Comparison of radial profiles at the end of the grain length obtained with two different grid levels.

to those presented in this section have been found in Ref. [65] for large nitrous-oxide/paraffin-wax HRE.

The mass fraction of the melted paraffin-wax, together with a detail of the near-wall region close to the fuel grain leading edge, is shown in Fig. 46. As expected the melted paraffin-wax is concentrated in a very narrow layer close to the wall surface. The picture gives an idea of how the present RANS approach is able to capture diffusion and convection, as well as decomposition per thermal cracking, of the melted paraffin-wax.

In Fig. 47 the molar fraction fields of the species participating to the radiative heat transfer are presented. Both water vapor and carbon dioxide, that recalling Fig. 11 are those most relevant in the radiation exchange process, are strongly concentrated in the hottest region of the flow field, where their mass fractions attain values up to 0.3 and 0.2, respectively. Carbon monoxide, on the other hand, attains the highest concentration in the region between the wall surface and the flame zone, with values up to 0.45. A role of carbon monoxide preliminary to the formation of the other radiating species is highlighted. For water vapor and

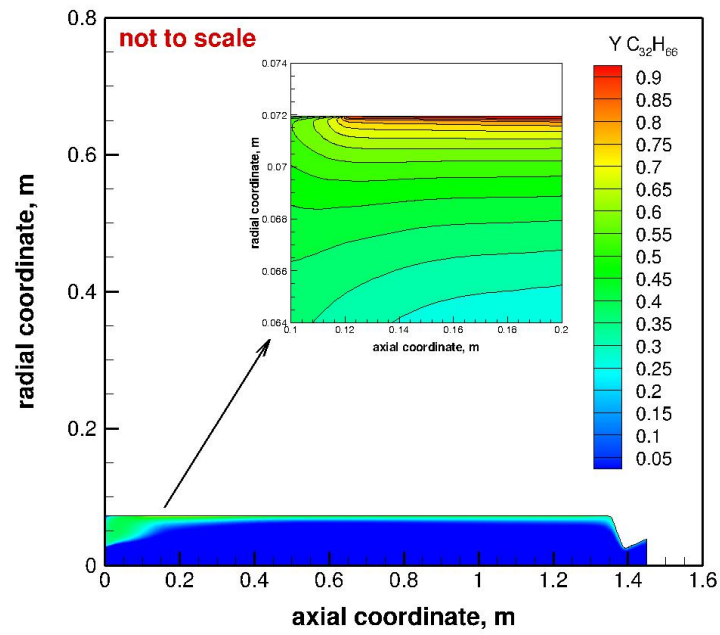


Figure 46: Mass fraction field of melted paraffin-wax.

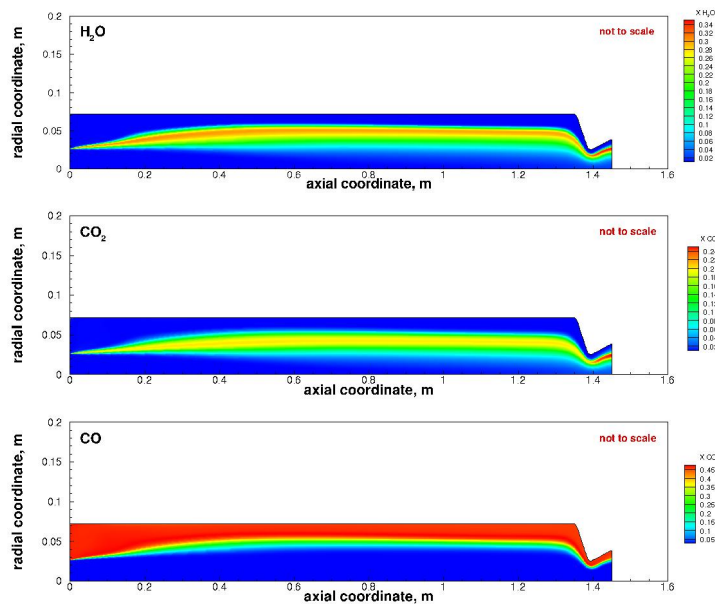


Figure 47: Molar fraction fields of radiative species.

carbon dioxide, it should be noted that the higher concentrations are reached into the nozzle region because of recombination reactions. This is confirmed in Fig. 48, where the mass fraction fields of the radical species are presented. Both atomic oxygen and hydrogen, as well as the hydroxyl radical, formed by dissociation into

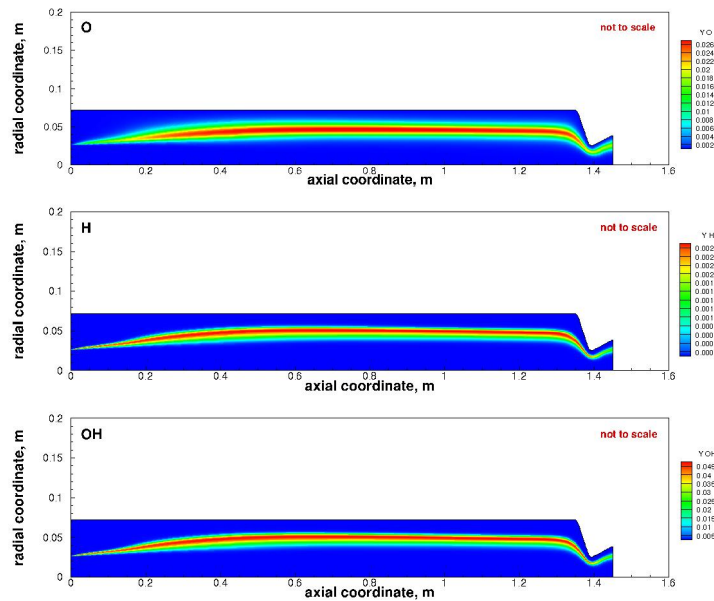


Figure 48: Mass fraction fields of radical species.

the flame zone, are significantly reduced across the flow expansion into the nozzle. Notice that the hydroxyl radical is the most present, while atomic hydrogen is concentrated in a very small amount.

7.6 RADIAL PROFILES OF TEMPERATURE AND SPECIES CONCENTRATION

Figure 49 shows into more details the radial profiles of temperature and some relevant species. The mid-grain section of the port is chosen as the reference location.

The mass fraction at wall of the melted paraffin-wax is about 0.8, highlighting the ability of the GSI boundary condition to solve the mixture composition at wall by accounting for the diffusion of other species toward the grain surface. From the 0.8 wall value, the mass fraction of melted paraffin-wax progressively decreases with the wall distance by undergoing the thermal cracking process. Notice that the rate of decay of the paraffin-wax mass fraction is directly related to the temperature gradient. While the thermal cracking is responsible for melted paraffin-wax consumption, the process gives rise to the production of ethylene. Such effect is however quite rapidly compensated by the combustion process, leading a complete consumption of the ethylene, as that of the oxygen convected from the core

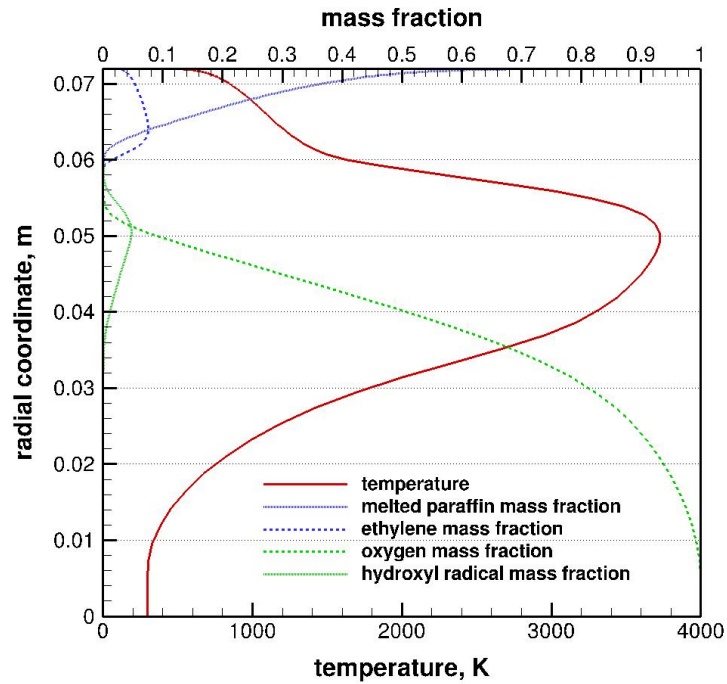


Figure 49: Radial profiles of temperature and species concentration at mid-grain location.

flow. As expected, ethylene and oxygen are fully consumed at the same radial location. Near such location, the peak of the hydroxyl radical is found, also almost identifying the point of maximum temperature.

The radial profiles of melted paraffin-wax and ethylene mass fractions, as well as that of temperature, are also shown at different axial locations along the grain in Fig. 50. In particular, the profiles at the start and at the end of the grain length are presented in order to understand the quantities evolution along the port axis. At the start of the grain length the profiles are dominated by the recirculation effect. The melted paraffin-wax is convected toward the centerline, as well as the ethylene and, in turn, the flame region, anchored to the inlet section as previously observed. The profiles at the end of the grain length, compared to those observed at mid-grain location, allow to better understand how the different quantities evolve along the port axis without any effect associated to recirculation phenomena. The value of the peak of temperature appears almost unchanged while its location is moved toward the centerline. Although a quite low temperature persist here, the core flow appears to a certain extent warmed up going downstream along the port, so that the relevant temperature joins the flame zone more smoothly. In the region

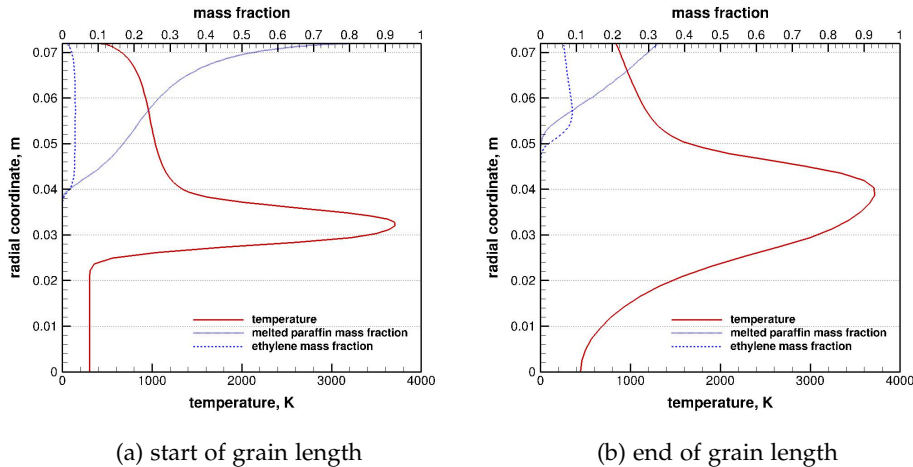


Figure 50: Radial profiles evolution along the grain length.

between the flame and the wall surface, the temperature gradient decreases along the port. Such a variation of the temperature gradient induce a lower thermal cracking process and, in turn, favor the growth of the layer which contains the melted paraffin-wax. Something similar to this happens, as a consequence, to the region with a high concentration of ethylene and, in turn, to the wall-to-flame distance, which, as previously observed, is slightly moved toward the core flow.

7.7 WALL HEAT FLUX CONTRIBUTIONS AND REGRESSION RATE EVOLUTION

The different contributions to the total wall heat flux are pointed out in Fig. 51.

The radiative wall heat flux first increases than, after a maximum is attained, starts to decrease downstream along the port. Such variations are strictly associated with the flame structure and the radiative species concentrations evidenced in Figs. 44 and 47. The average value of the radiative flux is about 0.78 MW/m^2 , that is comparable to the magnitude observed for the lab-scale HTPB case. The effect of increased port diameter and chamber pressure, with respect to the lab-scale HTPB simulations, appears then almost compensated by the higher wall-to-flame distance and the lower temperature in between the wall surface and the flame zone.

The convective wall heat flux essentially increases along the port because of the mass addition from the fuel grain, with the decay associated to the boundary layer

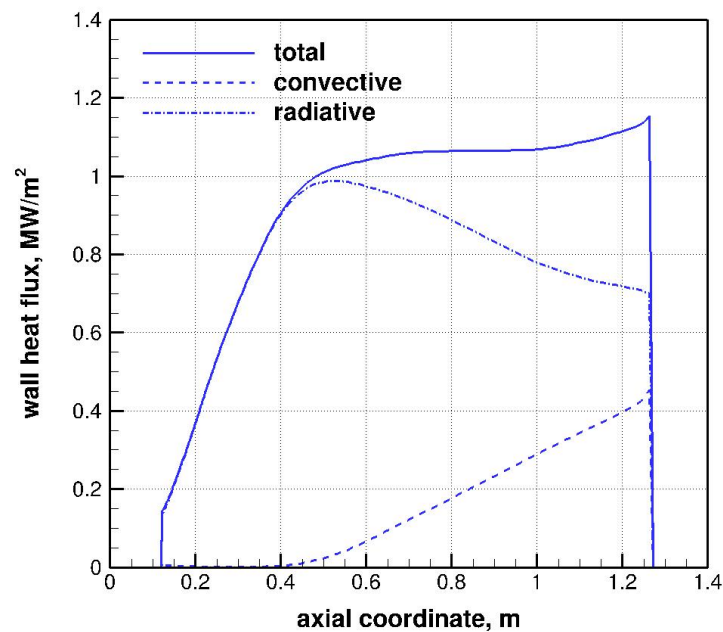


Figure 51: Contributions to the wall heat flux, paraffin-wax case study.

growth confined in the very first part of the grain length. A negligible role played by the recirculation region in the upstream part of the port in convective heat flux enhancement is observed. An average value of 0.15 MW/m^2 is found, hence almost an order of magnitude lower than for the lab-scale HTPB case. Again the effect of a high distance of the flame from the wall surface and a cold flow in the near-wall region are responsible of a low flux.

Looking at the total wall heat flux, it appears strongly dominated by the radiative contribution in the first part of the motor length, while it is increasingly influenced also by the convective contribution downstream along the port. The latter contributes on average to 84% of the total wall heat flux, appearing as a crucial contribution.

CFD results presented for HTPB fuels in Ref. [31], obtained by using a very simplified and experimentally calibrated radiative transfer model, show the radiative flux to increase and the convective flux to decrease with motor scale, respectively, until comparable values are attained. This agrees with the lower temperature gradient at wall, affecting convection, and the higher volumetric radiative source, enhancing radiation, typical of larger scale motors. The results in Fig. 51, obtained

with a more detailed radiative model and without any calibration, seem to confirm such behavior, underlying also an augmentation effect associated with the use of paraffin-based fuels. The injection of a relatively cold fluid at wall interface, in fact, creates a quite low temperature region at the wall surface that significantly flattens the wall temperature gradient, and hence decreases the convection. Such results have been in a certain way anticipated in Sec. 7.2, where the role of low temperatures in the wall-to-flame zone on the different wall heat flux contributions has been highlighted.

The evolution with coupling iterations of the regression rate profiles is shown in Fig. 52. To save computational time the convergence criterion has been based on the average regression rate, that had not to change of an amount higher than 5% between two successive iterations. Notice that the regression rate profile is significantly over-predicted at the first iteration, before reaching expected lower values at the next steps. This highlights a strong change of the temperature field, and in particular a significantly enhanced blowing, when the radiative flux is introduced. At the same time it denotes a strong reduction of the radiative wall heat flux associated with the modified structure of the flow field. The changes of temperature field and radiative wall heat flux profile are accordingly linked to a change of the regression rate. The regression rate increase obtained by including thermal radiation is 46% of the average final converged value. A significant blocking effect is highlighted if such percentage is compared to the share of the radiative flux. In conclusion, a radiative heat transfer model seems to be necessary to aim at reproducing the internal ballistics of paraffin-based HREs, at least for medium-scales.

7.8 COMBUSTION AND MIXING MODELING EVALUATION

Before comparing numerical results and experimental data for the whole set of selected test cases, it is important to test the combustion and mixing model to know to what an extent possible discrepancies should be attributed to such modeling part. To this purpose, an additional specific simulation of test case *L01* has been performed by enforcing the experimental regression rate, instead of solving the

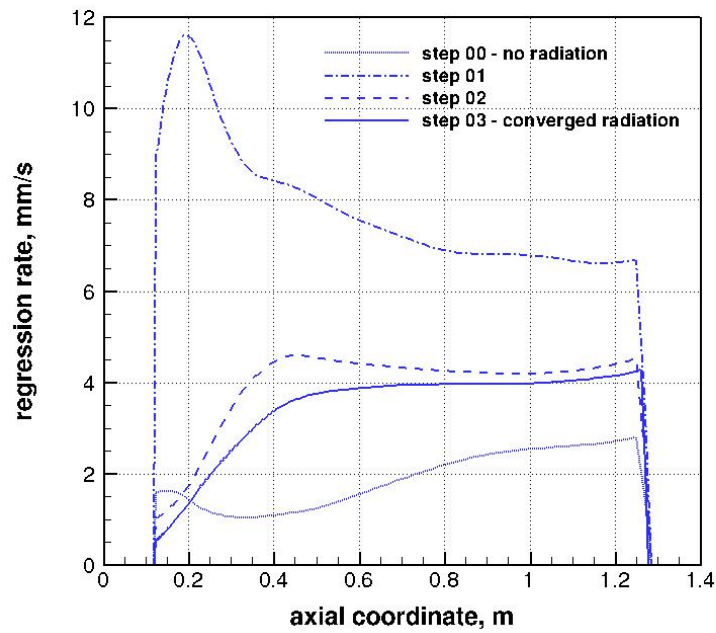


Figure 52: Regression rate evolution with iterations, paraffin-wax case study.

GSI balance equations at the wall surface. Such a simulation allows to evaluate the ability of the combustion and mixing model in reproducing the motor characteristic velocity by directly comparing the numerically predicted chamber pressure with the one measured through the experiment. The results obtained are summarized in Fig. 53. An under-estimation by 18% with respect to the experimental value is found. Such an error can be reasonably accepted in order to use global reaction mechanisms and, accordingly, save a lot of computational time. A possible improvement to be evaluated before moving to detailed reaction mechanisms, could be obtained by performing parametric analyses for the thermal cracking reaction rate constant, as well as by implementing reaction rate constants for ethylene combustion measured in hybrid rocket-like conditions, if available. Notice that a role could also be played by the post-chamber geometry, here not accurately reproduced in the radial direction. Finally, the pressure profile obtained by solving the surface energy balances appears very similar to that obtained by enforcing the experimental regression rate. This let us to expect a fairly well predicted regression rate.

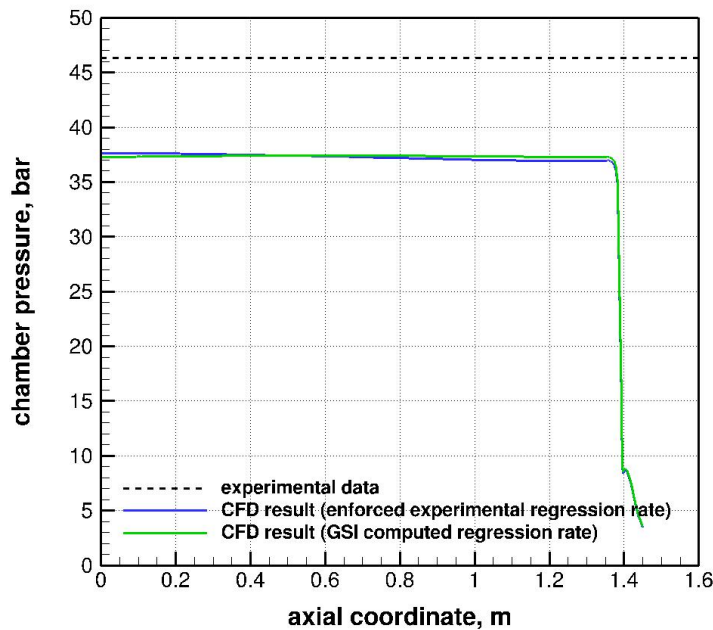


Figure 53: Evaluation of the combustion and mixing model.

7.9 REBUILDING RESULTS AND COMPARISON WITH TEST DATA

The whole set of selected test cases is here investigated to make more general considerations and test the internal ballistics prediction capability of the numerical setup for different mass flux and chamber pressure conditions. The same number of iterations has been required for all test cases, as a result of similar radiative-to-total wall heat flux contributions. Such contributions, together with computed space-averaged values of radiative and convective wall heat fluxes, are shown in Table 12. In addition, in Table 13, the computed space- and time-averaged chamber pressure, regression rate and mixture ratio, with a recall to port diameter and mass flux values, are presented.

The relative magnitude of the computed radiative wall heat flux is confirmed to be dominant in the total wall heating, giving a contribution of averagely 77% of the total value on the whole set of firing tests. As already observed for the reference test case, this happens in spite of not particularly high radiative wall heat fluxes, essentially because of very low convective contributions associated to shallow wall temperature gradients. In particular, such low gradients are caused by a

Table 12: Computed wall heat flux contributions.

Firing test	$\bar{q}_{w,\text{rad}}, \text{ MW/m}^2$	$\bar{q}_{w,\text{conv}}, \text{ MW/m}^2$	$\bar{q}_{w,\text{rad}}/\bar{q}_{w,\text{tot}}, \%$
L01	0.78	0.15	83.8
L04	0.67	0.34	66.3
P01	0.83	0.20	80.6
P04	0.45	0.13	77.6

Table 13: Computed chamber pressure, regression rate and mixture ratio.

Firing test	$\bar{G}_o, \text{ kg/m}^2\text{s}$	$\bar{p}_c, \text{ bar}$	$\bar{D}, \text{ mm}$	$\bar{r}, \text{ mm/s}$	O/F
L01	270.5	37.6	143.9	3.95	2.33
L04	368.0	39.3	123.9	3.77	2.86
P01	274.1	19.3	143.4	3.55	2.62
P04	146.9	9.3	135.2	2.17	2.16

high wall-to-flame distance, due to a relatively large port size, and a cold injection at wall, as paraffin-wax melting temperature is much lower than HTPB pyrolysis temperature. As expected, looking at Tables 12 and 13, the convective flux appears attenuated with increasingly lower mass fluxes. A non-trivial behavior with operative conditions is however found for the radiative flux.

For all firing tests, roughly the 50% of the final converged value of the space- and time-averaged regression rate is obtained by introducing the radiative heat transfer contribution. Such percentage increase, although very important, appears lower than that of the thermal radiation relative weight, as a consequence of a significant blowing computed when radiative heat flux is included, and associated blocking effect. In Fig. 54 the test cases L04 and P04 are considered to compare regression rate profiles for two very different conditions in terms of chamber pressure and oxidizer mass flux. After a sudden increase in the upstream part of the grain length, the regression rate shows different behaviors along the port. In fact,

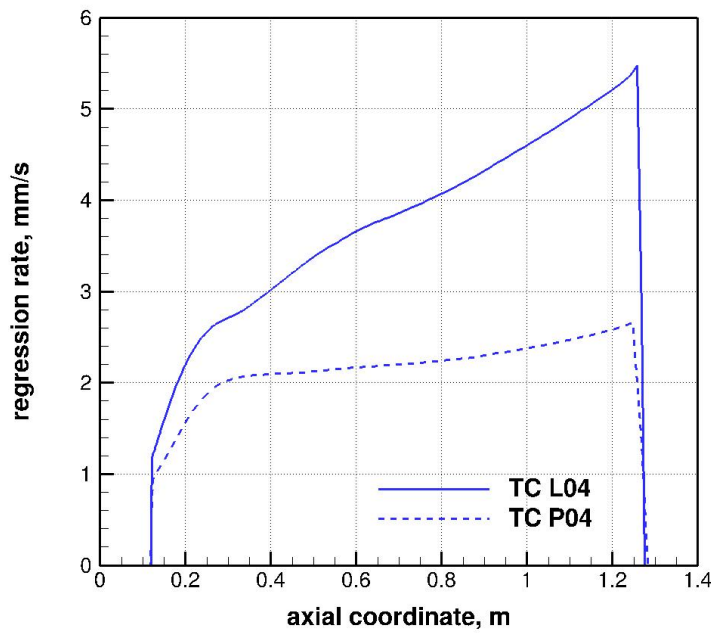


Figure 54: Comparison of regression rate profiles between different test conditions.

the regression rate is observed to increase in a more or less pronounced way depending on the relevant test case. This effect is essentially related to the mass flux condition and associated convective heat flux. In fact, when the mass flux is high and the convective flux has a steeper increase along the port, the same behavior is observed for the regression rate, and *vice versa* for low mass fluxes. This agrees with post-firing inspections of the final grain shape showing a coning effect for high mass fluxes and an almost axially uniform burning when low mass fluxes were envisaged [14]. Such behavior is also an indication that, as observed in the numerical rebuilding, the effects of the radiative heat flux are potentially able to overshadow those of the convective contribution. If thermal radiation had a minor role, the conical behavior, a peculiar trace of the convective heat flux, would have been observed for all different test conditions.

The comparison between numerical results and experimental data in terms of space- and time-averaged regression rate and chamber pressure are presented in Figs. 55 and 56, respectively. In Table 14 the errors on both quantities are highlighted. Both the space- and time-averaged regression rate and chamber pressure

appear fairly well rebuilt. Maximum errors falls within 20% for both regression rate and chamber pressure. Test case P01, in particular, is the best predicted.

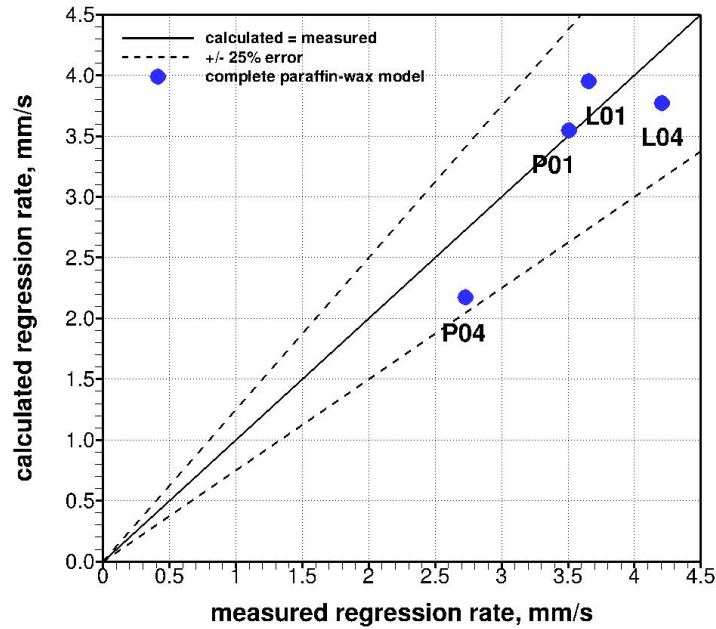


Figure 55: Comparison between computed and measured regression rates, paraffin-wax case study.

A comparison between experimental and numerical space- and time-averaged regression rates as a function of oxidizer mass flux is shown in Fig. 57. Power fitting laws are included together with experimental uncertainties gathered from Ref. [14]. The best predicted firing test, i.e. case P01, falls within the experimental uncertainty. Looking at the power fitting laws, experimental and numerical data are approximated by an exponent of 0.46 and 0.66, respectively. Calculated data appear slightly worse approximated by a power law than measured ones. Despite a different exponent is found, that for calculated data appears fairly in agreement with the value of 0.62 estimated from a wider set of experimental measurements according to Ref. [14].

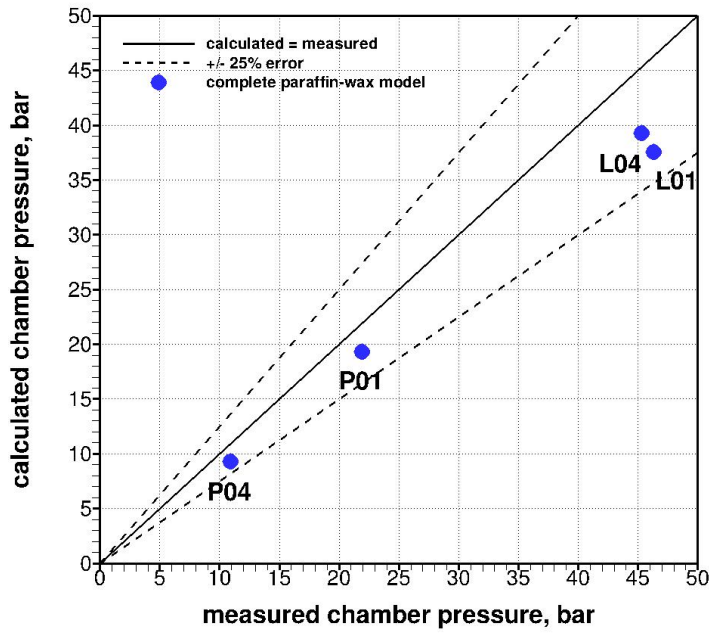


Figure 56: Comparison between computed and measured chamber pressures, paraffin-wax case study.

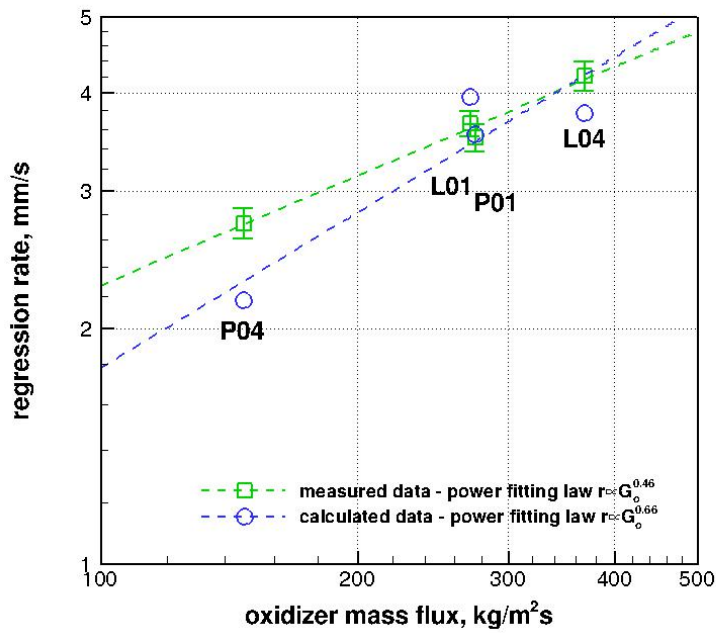


Figure 57: Comparison between computed and measured regression rates including error bars and power fitting laws as a function of the oxidizer mass flux.

Table 14: Errors between computed and measured regression rates and chamber pressures.

Firing test	$\epsilon_{\dot{r}}$, %	ϵ_{p_c} , %
<i>L01</i>	+8.0	-18.9
<i>L04</i>	-10.4	-13.3
<i>P01</i>	+1.1	-11.6
<i>P04</i>	-20.4	-14.8

CONCLUSIONS

The use of paraffin-based fuels has given rise to a renewed interest in hybrid rocket engine research and development. The high regression rate behavior observed for paraffin-wax fuel grains, in fact, has made hybrid rocket engines very promising for future efficient and low-cost space applications. Models for computational fluid dynamics simulations of paraffin-based hybrid rocket engines are however still in their infancy. Few works can be counted worldwide, anyway lacking of full internal ballistics prediction capabilities and thermal radiation modeling, as well as relying on very simplified combustion schemes. Such panorama has significantly limited the investigation of the way the different physical phenomena occurring in paraffin-based thrust chambers are coupled together. This investigation appears as a milestone on the way that leads to paraffin-based hybrid rocket engine design optimization.

In the present work a novel and comprehensive computational fluid dynamics model for paraffin-based hybrid rocket engine regression and combustion has been presented. By exploiting typical supercritical pressure conditions of the melted paraffin-wax, when it is injected into the ports of hybrid rocket engines, the entrainment has been assumed part of the turbulent mixing process. Accordingly, a classical single-phase Reynolds-averaged Navier-Stokes approach has been found viable to build up the numerical model. Such approach allowed to introduce an innovative gas-surface interaction boundary condition for liquefying fuels, which provided internal ballistics prediction capabilities to the numerical setup. The predictive capability appears as a crucial innovative feature with respect to the state of the art since it makes the numerical setup suitable for design purposes. The gas-surface interaction model has been made capable to account for the radiative heat flux contribution, by coupling the solutions obtained from the computational fluid dynamics solver and a radiative heat transfer code, developed for the purpose. Such a code, suitably verified and validated, has been found very effective to investigate the role of thermal radiation in hybrid rocket engines by relying on a fast and

exact method that is the discrete transfer. The code, in particular, has been made capable to integrate the radiative transfer equation within axisymmetric, gray and diffuse wall boundaries containing inhomogeneous, gray and non-scattering media. To complete the comprehensive model, the thermophysical properties of the melted paraffin-wax at supercritical pressures have been described in a simplified way by reasonably assuming a liquid-like behavior. In addition, a thermal cracking reaction step for the melted paraffin-wax into simpler gaseous species, actually working as fuel, has been introduced into the global reaction mechanism used to account for both combustion and dissociations.

The model has shown to be capable to describe the main flow field characteristics, like diffusion flame structure and concentration distributions of different species, as that of the melted paraffin-wax. Including a suitable minimum number of species into the model has been found necessary in order to adequately reproduce the temperature and composition fields, and, in turn, to correctly predict the radiative heat flux. The radiative contribution has been observed to be non-negligible in general, and potentially dominant in the total wall heat flux. A role of chamber pressure and port diameter in the enhancement of the radiative heating has been observed. At the same time, flow field conditions of paraffin-based hybrid rocket engines appeared to favor high shares of the radiative heat flux because of the relatively cold injection of melted paraffin-wax at grain interface, leading to rather small convective contributions. The radiative heat flux has been observed as indispensable for proper internal ballistics predictions. Under certain operative conditions, in fact, without accounting for the radiative heat transfer, the regression rate has been found underestimated by half. The model finally showed up a good ability to reproduce the motor internal ballistics since deviations of computed regression rates and chamber pressures with respect to experimental data, from selected firing tests of a medium-scale gaseous-oxygen/paraffin-wax hybrid rocket engine, have been found reasonably small.

The proposed predictive model and numerical approach gave, besides a first insight of the relevant physical phenomena and coupling, rather encouraging results. This stimulates further improvements, especially for what concern paraffin-wax thermochemistry modeling. Thermophysical properties should be extended on a wider range of temperatures, including the gas-like regime for temperatures

higher than the critical value. At the same time, the effect of different thermal cracking reaction rate constants from the literature should be tested in a proper sensitivity analysis. In the future, equations of state accounting for the real-gas behavior, as well as conveniently reduced detailed chemical mechanisms dedicated to paraffin-wax combustion, could be employed. The latter will also allow to predict the local volume fraction of soot, to account for its absorbing/emitting contribution into the radiative heat transfer model.

BIBLIOGRAPHY

- [1] T. Astarita and G. M. Carlomagno, *Infrared thermography for thermo–fluid–dynamics*. Heidelberg: Springer, 2013.
- [2] P. Rivière and A. Soufiani, “Updated band model parameters for H₂O, CO₂, CH₄ and CO radiation at high temperature,” *International Journal of Heat and Mass Transfer*, vol. 55, no. 13, pp. 3349–3358, 2012.
- [3] D. Suslov, B. Betti, T. Aichner, S. Soller, F. Nasuti, and O. Haidn, “Experimental investigation and CFD–simulation of the film cooling in an O₂/CH₄ subscale combustion chamber,” in *4th Space Propulsion Conference*, (Bordeaux, France), May 2012.
- [4] M. Pizzarelli, A. Urbano, and F. Nasuti, “Numerical analysis of deterioration in heat transfer to near–critical rocket propellants,” *Numerical Heat Transfer*, no. 57, pp. 297–314, 2010.
- [5] D. Bianchi, F. Nasuti, and C. Carmicino, “Hybrid rockets with axial injector: port diameter effect on fuel regression rate,” *Journal of Propulsion and Power*, vol. 32, no. 4, pp. 984–996, 2016.
- [6] J. J. Marano and G. D. Holder, “General equation for correlating the thermo–physical properties of n–paraffins, n–olefins, and other homologous series. 1. formalism for developing asymptotic behavior correlations,” *Industrial & Engineering Chemistry Research*, vol. 36, no. 5, pp. 1887–1894, 1997.
- [7] J. J. Marano and G. D. Holder, “General equation for correlating the thermo–physical properties of n–paraffins, n–olefins, and other homologous series. 2. asymptotic behavior correlations for PVT properties,” *Industrial & Engineering Chemistry Research*, vol. 36, no. 5, pp. 1895–1907, 1997.
- [8] J. J. Marano and G. D. Holder, “General equation for correlating the thermo–physical properties of n–paraffins, n–olefins, and other homologous series. 3.

- asymptotic behavior correlations for thermal and transport properties," *Industrial & Engineering Chemistry Research*, vol. 36, no. 6, pp. 2399–2408, 1997.
- [9] B. Blouri, F. Hamdan, and D. Herault, "Mild cracking of high-molecular-weight hydrocarbons," *Industrial & Engineering Chemistry Process Design and Development*, vol. 1, no. 24, pp. 30–37, 1985.
- [10] C. Carmicino and A. Russo Sorge, "Experimental investigation into the effect of solid-fuel additives on hybrid rocket performance," *Journal of Propulsion and Power*, vol. 31, no. 2, pp. 699–713, 2015.
- [11] H. Arisawa and T. B. Brill, "Flash pyrolysis of hydroxyl terminated polybutadiene (HTPB) ii: Implications of the kinetics to combustion of organic polymers," *Combustion and Flame*, vol. 106, pp. 131–143, 1996.
- [12] E. Farbar, J. Louwers, and T. Kaya, "Investigation of metallized and non-metallized hydroxyl terminated polybutadiene/hydrogen peroxide hybrid rockets," *Journal of Propulsion and Power*, vol. 23, no. 2, pp. 476–486, 2007.
- [13] K. Ramohalli and J. Yi, "Hybrids revisited," in *26th AIAA/ASME/SAE/ASEE Joint Propulsion Conference*, (Orlando, FL), 1990.
- [14] A. M. Karabeyoglu, G. Zilliac, B. J. Cantwell, S. DeZilwa, and P. Castellucci, "Scale-up tests of high regression rate paraffin-based hybrid rocket fuels," *Journal of Propulsion and Power*, vol. 20, no. 6, pp. 1037–1045, 2004.
- [15] M. A. Karabeyoglu, B. J. Cantwell, and J. Stevens, "Evaluation of homologous series of normal-alkanes as hybrid rocket fuels," in *41st AIAA/ASME/SAE/ASEE Joint Propulsion Conference*, (Tucson, AR), 2005.
- [16] D. Bianchi, F. Nasuti, and D. Delfini, "Modeling of gas-surface interface for paraffin-based hybrid rocket fuels in CFD simulations," in *6th European Conference for Aeronautics and Space Sciences (EUCASS)*, (Krakow, Poland), 2015.
- [17] M. Chiaverini, "Review of solid-fuel regression rate behavior in classical and nonclassical hybrid rocket motors," in *Fundamentals of Hybrid Rocket Combustion and Propulsion* (K. Kuo and M. Chiaverini, eds.), vol. 218 of *Progress in Astronautics and Aeronautics*, pp. 37–125, AIAA, 2007.

- [18] D. Altman and A. Holzman, "Overview and history of hybrid rocket propulsion," in *Fundamentals of Hybrid Rocket Combustion and Propulsion* (K. Kuo and M. Chiaverini, eds.), vol. 218 of *Progress in Astronautics and Aeronautics*, pp. 1–36, AIAA, 2007.
- [19] J. Majdalani, "Vortex injection hybrid rockets," in *Fundamentals of Hybrid Rocket Combustion and Propulsion* (K. Kuo and M. Chiaverini, eds.), vol. 218 of *Progress in Astronautics and Aeronautics*, pp. 247–276, AIAA, 2007.
- [20] B. J. Cantwell, A. M. Karabeyoglu, and D. Altman, "Recent advances in hybrid propulsion," *International Journal of Energetic Materials and Chemical Propulsion*, vol. 9, no. 4, pp. 305–326, 2010.
- [21] M. V. F. Ribeiro and P. C. G. Junior, "Hybrid rocket motors propellants: A historical approach," in *21st International Congress of Mechanical Engineering*, (Natal, Brazil), 2011.
- [22] P. G. Carrick and C. W. Larson, "Lab scale test and evaluation of cryogenic solid hybrid rocket fuels," in *31st AIAA/ASME/SAE/ASEE Joint Propulsion Conference*, (San Diego, CA), 1995.
- [23] M. E. DeRose, K. Pfeil, P. G. Carrick, and C. W. Larson, "Tube burner studies of cryogenic solid combustion," in *33rd AIAA/ASME/SAE/ASEE Joint Propulsion Conference*, (Seattle, WA), 1997.
- [24] C. P. S. Clair, E. E. Rice, W. H. Knuth, and D. J. Gramer, "Advanced cryogenic solid hybrid rocket engine developments – concept and test results," in *34th AIAA/ASME/SAE/ASEE Joint Propulsion Conference*, (Cleveland, OH), 1998.
- [25] D. J. Gramer, W. H. Knuth, E. E. Rice, and C. P. S. Clair, "Experimental investigation of a metallized cryogenic hybrid rocket engine," in *34th AIAA/ASME/SAE/ASEE Joint Propulsion Conference*, (Cleveland, OH), 1998.
- [26] M. A. Karabeyoglu, D. Altman, and B. J. Cantwell, "Combustion of liquefying hybrid propellants: Part 1, general theory," *Journal of Propulsion and Power*, vol. 18, no. 3, pp. 610–620, 2002.

- [27] M. A. Karabeyoglu and B. J. Cantwell, "Combustion of liquefying hybrid propellants: Part 2, stability of liquid films," *Journal of Propulsion and Power*, vol. 18, no. 3, pp. 621–630, 2002.
- [28] G. A. Marxman, C. E. Wooldridge, and R. J. Muzzy, "Fundamentals of hybrid boundary layer combustion," in *Heterogeneous Combustion* (I. Glassman, J. L. Green, and H. G. Wolfhard, eds.), vol. 15 of *Progress in Astronautics and Aeronautics*, pp. 485–521, AIAA, 1964.
- [29] G. A. Marxman, "Combustion in the turbulent boundary layer on a vaporizing surface," in *10th Symposium on Combustion*, (Pittsburgh, PA), 1965.
- [30] K. Kuo, Y. C. Lu, M. J. Chiaverini, D. K. Johnson, N. Serin, G. A. Risha, C. L. Merkle, and V. Sankaran, "Fundamental phenomena on fuel decomposition and boundary-layer combustion processes with applications to hybrid rocket motors," Tech. Rep. NAS8–39945, 1996. NASA.
- [31] V. Sankaran, "Computational fluid dynamics modeling of hybrid rocket flow-fields," in *Fundamentals of Hybrid Rocket Combustion and Propulsion* (K. Kuo and M. Chiaverini, eds.), vol. 218 of *Progress in Astronautics and Aeronautics*, pp. 323–349, AIAA, 2007.
- [32] M. J. Chiaverini, N. Serin, D. K. Johnson, Y. Lu, K. Kuo, and G. A. Risha, "Regression rate behavior of hybrid rocket solid fuels," *Journal of Propulsion and Power*, vol. 16, no. 1, pp. 125–132, 2000.
- [33] M. J. Chiaverini, K. Kuo, A. Peretz, and G. C. Harting, "Regression rate behavior of hybrid rocket solid fuels," *Journal of Propulsion and Power*, vol. 17, no. 1, pp. 99–110, 2001.
- [34] N. Serin and Y. Gogus, "Navier–Stokes investigation on reacting flow field of HTPB/O₂ hybrid motor and regression rate evaluation," in *39th AIAA/ASME/SAE/ASEE Joint Propulsion Conference*, (Huntsville, AL), 2003.
- [35] G. Gariani, F. Maggi, and L. Galfetti, "Simulation code for hybrid rocket combustion," in *46th AIAA/ASME/SAE/ASEE Joint Propulsion Conference*, (Nashville, TN), 2010.

- [36] G. C. Cheng, R. C. Farmer, H. S. Jones, and J. S. McFarlane, "Numerical simulation of the internal ballistics of a hybrid rocket motor," in *32nd Aerospace Science Meeting*, (Reno, NV), 1994.
- [37] P. Liang, R. J. Ungewitter, and S. E. Claflin, "CFD analysis of the 24-inch JIRAD hybrid rocket motor," in *31st AIAA/ASME/SAE/ASEE Joint Propulsion Conference*, (San Diego, CA), 1995.
- [38] C. L. Lin and H. H. Chiu, "Numerical analysis of spray combustion in hybrid rockets," in *31st AIAA/ASME/SAE/ASEE Joint Propulsion Conference*, (San Diego, CA), 1995.
- [39] C. Carmicino and A. Russo Sorge, "Role of injection in hybrid rockets regression rate behavior," *Journal of Propulsion and Power*, vol. 21, no. 4, pp. 606–612, 2005.
- [40] C. Carmicino and A. Russo Sorge, "Influence of a conical axial injector on hybrid rocket performance," *Journal of Propulsion and Power*, vol. 22, no. 5, pp. 984–995, 2006.
- [41] D. Bianchi, B. Betti, F. Nasuti, and C. Carmicino, "Simulation of gaseous oxygen/hydroxyl-terminated polybutadiene hybrid rocket flowfields and comparison with experiments," *Journal of Propulsion and Power*, vol. 31, no. 3, pp. 919–929, 2015.
- [42] G. D. Di Martino, C. Carmicino, and R. Savino, "Transient computational thermofluid–dynamic simulation of hybrid rocket internal ballistics," *Journal of Propulsion and Power*, 2017. In press.
- [43] G. D. Di Martino, S. Mungiguerra, C. Carmicino, and R. Savino, "Computational fluid–dynamic simulations of hybrid rocket internal flow including discharge nozzle," in *53rd AIAA/SAE/ASEE Joint Propulsion Conference*, (Atlanta, GA), 2017.
- [44] M. Lazzarin, F. Barato, A. Bettella, and D. Pavarin, "Computational fluid dynamics simulation of regression rate in hybrid rockets," *Journal of Propulsion and Power*, vol. 29, no. 6, pp. 1445–1452, 2013.

- [45] M. Faenza, F. Barato, M. Lazzarin, and D. Pavarin, "Hybrid rocket motors regression rate prediction through CFD simulations," in *6th European Conference for Aeronautics and Space Sciences (EUCASS)*, (Krakow, Poland), 2015.
- [46] S. May and O. Bozic, "CFD simulations of chemical non-equilibrium reacting flow within the AHRES hybrid rocket engine," in *6th European Conference for Aeronautics and Space Sciences (EUCASS)*, (Krakow, Poland), 2015.
- [47] Y. Chen, A. Lai, J. Lin, T. Chou, and J. Wu, "Investigation on tri-propellant hybrid rocket performance," in *52nd AIAA/SAE/ASEE Joint Propulsion Conference*, (Salt Lake City, UT), 2016.
- [48] Y. Chen, "Comprehensive modeling of hybrid rocket internal ballistics," in *53rd AIAA/SAE/ASEE Joint Propulsion Conference*, (Atlanta, GA), 2017.
- [49] M. A. Karabeyoglu, B. J. Cantwell, and D. Altman, "Development and testing of paraffin-based hybrid rocket fuels," in *37th AIAA/ASME/SAE/ASEE Joint Propulsion Conference*, (Salt Lake City, UT), 2001.
- [50] G. Zilliac, M. A. Karabeyoglu, B. J. Cantwell, R. Hunt, S. DeZilwa, M. Shoffstall, and P. T. Soderman, "Ames hybrid combustion facility," Tech. Rep. TM-2003-211864, 2003. NASA.
- [51] I. Nakagawa and S. Nikone, "Study on the regression rate of paraffin-based hybrid rocket fuels," *Journal of Propulsion and Power*, vol. 27, no. 6, pp. 1276–1279, 2011.
- [52] A. Chandler, E. T. Jens, B. J. Cantwell, and G. S. Hubbard, "Visualization of the liquid layer combustion of paraffin fuel for hybrid rocket applications," in *48th AIAA/ASME/SAE/ASEE Joint Propulsion Conference*, (Atlanta, GE), 2012.
- [53] E. T. Jens, F. S. Mechentel, B. J. Cantwell, G. S. Hubbard, and A. Chandler, "Combustion visualization of paraffin-based hybrid rocket fuel at elevated pressures," in *50th AIAA/ASME/SAE/ASEE Joint Propulsion Conference*, (Cleveland, OH), 2014.

- [54] M. Kobald, H. Ciezki, and S. Schleichtriem, "Optical investigation of the combustion process in paraffin-based hybrid rocket fuels," in *49th AIAA/ASME/SAE/ASEE Joint Propulsion Conference*, (San Jose, CA), 2013.
- [55] A. Petrarolo, M. Kobald, and S. Schleichtriem, "Optical analysis of the liquid layer combustion of paraffin-based hybrid rocket fuels," in *7th European Conference for Aeronautics and Space Sciences (EUCASS)*, (Milan, Italy), 2017.
- [56] A. Petrarolo, M. Kobald, and S. Schleichtriem, "Liquid layer combustion visualization of paraffin-based hybrid rocket fuels," in *53rd AIAA/SAE/ASEE Joint Propulsion Conference*, (Atlanta, GA), 2017.
- [57] M. Adachi and T. Shimada, "Liquid films instability of liquefying hybrid rocket fuels under supercritical conditions," *AIAA Journal*, vol. 53, no. 6, pp. 1578–1589, 2015.
- [58] P. Narsai, K. Venkataraman, K. J. Stober, and B. J. Cantwell, "Measuring time-varying fuel regression rates with image processing in a hybrid rocket motor," in *52nd AIAA/SAE/ASEE Joint Propulsion Conference*, (Salt Lake City, UT), 2016.
- [59] M. Santi, E. Paccagnella, A. Ruffin, F. Barato, D. Pavarin, G. Mistè, G. Venturelli, and N. Bellomo, "Development and testing of a long burning time lab-scale paraffin-based hybrid rocket motor," in *53rd AIAA/SAE/ASEE Joint Propulsion Conference*, (Atlanta, GA), 2017.
- [60] Y. Funami, V. Novozhilov, I. Nakagawa, and T. Shimada, "Regression modeling of paraffin-based hybrid rocket fuels for internal ballistics simulation," in *46th AIAA/ASME/SAE/ASEE Joint Propulsion Conference*, (Nashville, TN), 2010.
- [61] J. Y. Lestrade, J. Anthoine, and G. Lavergne, "Liquefying fuel regression rate modeling in hybrid propulsion," *Aerospace Science and Technology*, no. 42, pp. 80–87, 2015.
- [62] A. Chandler Karp, B. Nakazono, R. Shotwell, J. Benito, D. Vaughan, and G. Story, "Technology plan and preliminary results for a low temperature

- hybrid Mars ascent vehicle concept," in *53rd AIAA/SAE/ASEE Joint Propulsion Conference*, (Atlanta, GA), 2017.
- [63] B. Evans and A. Karabeyoglu, "Development and testing of SP7 fuel for Mars ascent vehicle application," in *53rd AIAA/SAE/ASEE Joint Propulsion Conference*, (Atlanta, GA), 2017.
- [64] N. Bellomo, F. Barato, M. Faenza, M. Lazzarin, A. Bettella, and D. Pavarin, "Numerical and experimental investigation of unidirectional vortex injection in hybrid rocket engines," *Journal of Propulsion and Power*, vol. 29, no. 5, pp. 1097–1113, 2013.
- [65] M. Lazzarin, M. Faenza, F. Barato, N. Bellomo, A. Bettella, and D. Pavarin, "Computational fluid dynamics simulation of hybrid rockets of different scales," *Journal of Propulsion and Power*, vol. 31, no. 5, pp. 1458–1469, 2015.
- [66] G. Ranuzzi, D. Cardillo, and M. Invigorito, "Numerical investigation of a N₂O–paraffin hybrid rocket engine combusting flowfield," in *6th European Conference for Aeronautics and Space Sciences (EUCASS)*, (Krakow, Poland), 2015.
- [67] B. J. McBride and S. Gordon, "Computer program for calculation of complex chemical equilibrium compositions and applications," Tech. Rep. RP–1311, 1994. NASA.
- [68] J. D. Anderson, *Hypersonic and high-temperature gas dynamics*. Reston: AIAA Education series, 2 ed., 2006.
- [69] P. R. Spalart and S. R. Allmaras, "A one-equation turbulence model for aerodynamic flow," *La Recherche Aérospatiale*, vol. 1, pp. 5–21, 1994.
- [70] S. K. Godunov, A. V. Zabrodin, M. I. Ivanov, A. N. Kraiko, and G. P. Prokopov, *Numerical solution of multidimensional problems of gas dynamics*. Moscow: Izdatel'stvo Nauka, 1976.
- [71] P. L. Roe, "Approximate Riemann solvers, parameter vectors and difference schemes," *Journal of Computational Physics*, vol. 43, pp. 357–372, 1981.

- [72] G. Strang, "On the construction and comparison of difference schemes," *SIAM Journal on Numerical Analysis*, vol. 5, no. 3, pp. 506–517, 1968.
- [73] P. N. Brown, G. D. Byrne, and A. C. Hindmarsh, "VODE: a variable-coefficient ODE solver," *SIAM Journal on Scientific and Statistical Computing*, vol. 10, no. 5, pp. 1038–1051, 1989.
- [74] B. Betti, M. Pizzarelli, and F. Nasuti, "Coupled heat transfer analysis in regeneratively cooled thrust chambers," *Journal of Propulsion and Power*, vol. 30, no. 2, pp. 360–367, 2014.
- [75] B. Betti, D. Bianchi, F. Nasuti, and E. Martelli, "Chemical reaction effects on heat loads of CH₄/O₂ and H₂/O₂ rockets," *AIAA Journal*, vol. 54, no. 5, pp. 1693–1703, 2016.
- [76] G. Leccese, D. Bianchi, B. Betti, D. Lentini, and F. Nasuti, "Convective and radiative wall heat transfer in liquid rocket thrust chambers," *Journal of Propulsion and Power*, 2017. In press.
- [77] R. A. Gater and M. R. L'Ecuyer, "A fundamental investigation of the phenomena that characterize liquid–film cooling," *International Journal of Heat and Mass Transfer*, vol. 13, pp. 1925–1939, 1970.
- [78] P. Milova, "Entrainment effects on combustion process in paraffin–based hybrid rocket motors," in *Ph.D Thesis in Aerospace Engineering*, (Politecnico di Milano), 2015.
- [79] D. Bianchi, "Modeling of ablation phenomena in space applications," in *Ph.D Thesis in Theoretical and Applied Mechanics*, (Sapienza Università di Roma), 2007.
- [80] D. Bianchi, F. Nasuti, R. Paciorri, and M. Onofri, "Computational analysis of hypersonic flows including finite rate ablation thermochemistry," 7th European Workshop on Thermal Protection Systems and Hot Structures, ESA–ESTEC, Noordwijk, The Netherlands, April 8–10, 2013.
- [81] A. Turchi, D. Bianchi, F. Nasuti, and M. Onofri, "A numerical approach for the study of the gas–surface interaction in carbon–phenolic solid rocket nozzles," *Aerospace Science and Technology*, vol. 27, no. 1, pp. 25–31, 2013.

- [82] D. Bianchi and F. Nasuti, "Numerical analysis of nozzle material thermochemical erosion in hybrid rocket engines," *Journal of Propulsion and Power*, vol. 29, no. 3, pp. 547–558, 2013.
- [83] V. Quan, "Quasi-steady solution for ablation-erosion heat transfer," *Journal of Spacecraft and Rockets*, vol. 7, no. 3, pp. 355–357, 1970.
- [84] M. Oschwald and A. Schik, "Supercritical nitrogen free jet investigated by spontaneous Raman scattering," *Experiments in Fluids*, no. 27, pp. 497–506, 1999.
- [85] M. Oschwald and M. Micci, "Spreading angle and centerline variation of density of supercritical nitrogen jets," *Atomization and Sprays*, no. 11, pp. 91–106, 2002.
- [86] M. F. Modest, *Radiative heat transfer*. San Diego: Academic Press, 2003.
- [87] H. Ziebland and R. C. Parkinson, "Heat transfer in rocket engines," Tech. Rep. AG-148-71, 1971. AGARD.
- [88] C. L. Tien, "Thermal radiation properties of gases," *Advances in Heat Transfer*, vol. 5, pp. 253–324, 1968.
- [89] "International workshop on measurement and computation of turbulent nonpremixed flames – radiation models," 2003. Sandia National Laboratories – <http://www.sandia.gov/TNF/radiation.html>.
- [90] P. Giordano and D. Lentini, "Combustion-radiation-turbulence interaction modelling in absorbing/emitting nonpremixed flames," *Combustion Science and Technology*, vol. 172, no. 1, pp. 1–22, 2001.
- [91] C. M. Mazzoni, "Modelling of thermal radiation and soot emissions in aerospace applications," in *Ph.D Thesis in Aeronautics and Space Technology*, (Sapienza Università di Roma), 2011.
- [92] H. Hottel and E. Cohen, "Radiant heat exchange in a gas filled enclosure: Allowance for non-uniformity in temperature," *AIChE Journal*, vol. 4, no. 1, pp. 3–14, 1958.

- [93] H. Hottel and A. Sarofim, *Radiative transfer*. New York: McGraw–Hill, 1967.
- [94] A. Schuster, “Radiation through a foggy atmosphere,” *Astrophysical Journal*, vol. 21, no. 1, pp. 1–22, 1905.
- [95] K. Schwarzschild, “über das gleichgewicht der sonnenatmosphären,” *Nachrichten von der Gesellschaft der Wissenschaften zu Göttingen, Mathematische–Physikalische Klasse*, vol. 1906, no. 1, pp. 41–53, 1906.
- [96] S. Chandrasekar, *Radiative Transfer*. New York: Dover, 1960.
- [97] T. S. Wang, “Multidimensional unstructured–grid liquid rocket–engine nozzle performance and heat transfer analysis,” *Journal of Propulsion and Power*, vol. 22, no. 1, pp. 78–84, 2006.
- [98] F. Göbel and C. Mundt, “Implementation of the P_1 radiation model in the CFD solver NSMB and investigation of radiative heat transfer in the SSME main combustion chamber,” in *17th AIAA International Space Planes and Hypersonic Systems and Technologies Conference*, (San Francisco, CA), Apr. 2011.
- [99] J. Jeans, “The equations of radiative transfer of energy,” *Monthly Notices of the Royal Astronomical Society*, vol. 78, no. 1, pp. 28–36, 1917.
- [100] F. Göbel, B. Kniesner, M. Frey, O. Knab, and C. Mundt, “Radiative heat transfer analysis in modern rocket combustion chambers,” *CEAS Space Journal*, vol. 6, no. 2, pp. 79–98, 2014.
- [101] J. Fleck, “The calculation of nonlinear radiation transport by a Monte Carlo method: Statistical physics,” *Methods in Computational Physics*, vol. 1, pp. 43–65, 1961.
- [102] F. C. Lockwood and N. G. Shah, “A new radiation solution method for incorporation in general combustion prediction procedures,” *Symposium (International) on Combustion*, vol. 18, no. 1, pp. 1405–1414, 1981.
- [103] S. T. Hsu, *Engineering heat transfer*. Princeton: Van Nostrand Company, 1963.
- [104] F. Bonifazi and D. Lentini, “Effect of gas–phase carbon depletion by sooting on the structure of methane/air flamelets,” in *7th International Symposium On*

Turbulence, Heat and Mass Transfer (K. Hanjalić, Y. Nagano, D. Borello, and S. Jakirlić, eds.), pp. 757–760, Begell House Inc., 2012.

- [105] J. Liu and S. N. Tiwari, “Radiative heat transfer effects in chemically reacting nozzle flows,” *Journal of Thermophysics and Heat Transfer*, vol. 10, no. 3, pp. 436–444, 1996.
- [106] G. Ordonneau, O. Haidn, S. Soller, and M. Onofri, “Oxygen–methane combustion studies in the in space propulsion programme,” in *4th European Conference for Aerospace Sciences (EUCASS)*, (Saint Petersburg, Russia), July 2011.
- [107] B. Betti, D. Bianchi, G. Leccese, D. Lentini, and F. Nasuti, “Convective and radiative contributions to wall heat transfer in liquid rocket engine thrust chambers,” in *51st AIAA/ASME/SAE/ASEE Joint Propulsion Conference*, (Orlando, FL), 2015.
- [108] M. Pizzarelli, F. Nasuti, and M. Onofri, “CFD analysis of transcritical methane in rocket engine cooling channels,” *Journal of Supercritical Fluids*, no. 62, pp. 79–87, 2012.
- [109] M. Pizzarelli, “Modeling of cooling channel flow in liquid–propellant rocket engines,” in *Ph.D Thesis in Theoretical and Applied Mechanics*, (Sapienza Università di Roma), 2007.
- [110] B. M. Fabuss, J. O. Smith, R. I. Lait, A. S. Bornsanyi, and C. N. Satterfield, “Rapid thermal cracking of n–hexadecane at elevated pressures,” *Industrial & Engineering Chemistry Process Design and Development*, vol. 1, no. 4, pp. 293–299, 1962.
- [111] J. Andersen, C. L. Rasmussen, T. Giselsson, and P. Glarborg, “Global combustion mechanisms for use in CFD modeling under oxy–fuel conditions,” *Energy & Fuels*, vol. 23, pp. 1379–1389, 2009.
- [112] A. Coronetti and W. A. Sirignano, “Numerical analysis of hybrid rocket combustion,” *Journal of Propulsion and Power*, vol. 29, no. 2, pp. 371–384, 2013.
- [113] M. A. Karabeyoglu, B. J. Cantwell, and G. Zilliac, “Development of scalable space–time averaged regression rate expressions for hybrid rockets,” *Journal of Propulsion and Power*, vol. 23, no. 4, pp. 737–747, 2007.

- [114] C. Carmicino, "Acoustics, vortex shedding, and low-frequency dynamics interaction in an unstable hybrid rocket," *Journal of Propulsion and Power*, vol. 25, no. 6, pp. 1322–1335, 2009.
- [115] R. A. Isbell and M. Q. Brewster, "Optical properties of energetic materials: RDX, HMX, AP, NC/NG, and HTPB," *Propellants, Explosives, Pyrotechnics*, vol. 23, pp. 218–224, 1998.
- [116] F. H. Mark and J. I. Kroschwitz, *Encyclopedia of polymer science and engineering*, vol. 17. New York: Wiley, 1989.